Model-based Study of Mixing

-using Computational Fluid Dynamics

and Experiments

by

Ameer Shareef and Victor Åberg

Department of Chemical Engineering
Lund University

June 2018

Supervisor: **Post Doc Niklas Andersson**
Examiner: **Professor Bernt Nilsson**

Postal address	**Visiting address**	**Telephone**
P.O. Box 124	Getingevägen 60	+46 46-222 82 85
SE-221 00 Lund, Sweden		+46 46-222 00 00
Web address		**Telefax**
www.chemeng.lth.se		+46 46-222 45 26

Preface

Our deepest thanks and gratitude to our supervisor, Post-Doc Niklas Andersson and examiner, Professor Bernt Nilsson, for providing us with an interesting thesis project and for your continuous interest, help, patience and enthusiasm for the project. We also would like to thank the Department of Chemical Engineering and Professor Bernt Nilsson for providing us with the experimental equipment needed for the experimental study and Niklas Andersson for the seemingly endless stream of computers that were sent to our little work space. Further acknowledgments go to the PHD students that were checking in on how we were doing and made us feel like one in the gang during lunch and coffee-breaks. Thanks to rest of the staff for providing a loving and including atmosphere at the department. We would also like to give a special thanks to our fellow co-workers Dennis Bogren, Linus Gustafsson and Daniel Nilsson, which we have shared office with for the duration of our thesis. You have endured occasional outbursts with patience and humor and we would not have managed this without your positive attitude and goal oriented mindset. Thank you, guys. Finally, we would like to thank our families and beloved ones at home for patiently putting up with us. You are the best.

Abstract

Mixing in millimeter scale applications faces completely different challenges compared with the macro scale. A thorough understanding of the physics and mass conservation principles that are affecting the fluid dynamics, are therefore key for development and successful implementation of mixers, in an existing process. Only relying on molecular diffusion for molecules with very low diffusivities can result in unfeasibly long mixing channels, thus making purely diffusive mixing impractical for continuous processes. In contrast, by introducing perturbations to the flow field which breaks up, distorts, stretches and folds the fluid elements continuously, can be used to increase the level of mixing. Mixers can broadly be dealt with in two separate categories, passive and active. Active mixers rely on an external source of power to enhance mixing, while passive mixers work without moving actuators.

The result in this thesis show both from Computational Fluid Dynamics and experimental measurements, that the flow regimes and mixing quality, using the ÄKTA T-mixer, in small scale continuous chromatography processes, potentially is limited by set flowrates and running parameters of the process and therefore seems to benefit from additional mixing action from passive and active mixing methods. When it comes to choosing which method to implement it should be based on both what level of mixing that is required as well on what components that are being mixed. To have control over the mixing process and a well-defined dispersion in the mixer is also important. Due to the increased shear rate and sharper gradients in the flow velocity field in active mixers, softer mixing methods, provided by passive mixers, potentially pose a more smooth and controlled mixing process compared to active mixers, when it comes to shear sensitive and fragile compounds.

Sammanfattning

Mixning i millimeterskalan, ställs inför helt andra utmaningar och förutsättningar jämfört med mixning i stor skala. God förståelse för fysiken och kontinuitetsprinciperna som påverkar fluidmekaniken är därför viktig när man utvecklar och implementerar mixers i sin process. Molekylär diffusion är en långsam process vilket innebär att längden på mixningskanalerna för att nå homogenitet, blir ohållbart långa. Detta gör diffusion opraktiskt som mixningsmetod i många kontinuerliga processer. I jämförelse, genom att introducera kontinuerliga perturbationer som bryter upp, sträcker, viker och förvrider flödeslinjerna i fluiden som skall mixas kan man se en märkbar ökning i mixningsgrad. Mixrar kan i stort delas in i två separata klasser, aktiva och passiva. Aktiva mixrar förlitar sig på en extern kraftkälla medan passiva mixrar fungerar utan rörliga delar.

Resultatet i exjobbet visar från beräkningsbaserad fluidmekanik och experiment, att mixningsgraden i ÄKTA T-mixern är potentiellt styrd av driftsförhållandena och flödena som processen körs i och därför verkar gynnas av passiva och aktiva mixrar. När det kommer till att välja metod, verkar det inte bara vara viktigt med den önskade mixningsgraden utan även vilka komponenter i fråga som skall mixas. En tydligt definierad dispersion i mixern är också viktig för att ha ett kontrollerat mixningsförlopp. Den högre skjuvningsgraden i aktiva mixrar kan potentiellt sett skada ömtåliga molekyler, vilket gör att mer kontrollerade och mjuka mixningsförlopp i passiva mixrar, i direkt jämförelse kan vara bättre.

Table Of Contents

1 Introduction 1
2 Theory 2
2.1 Mixers 2
2.2 Quantification of mixing processes 3
2.3 Governing equations – Computational Fluid Dynamics(CFD) 4
2.4 Macroscopic Non-ideal mixing models 9
2.5 Experimental theory and Conductivity Measurements 9
3 Material and Method 10
3.1 CFD analysis 10
3.2 Experimental based modelling 19
3.3 Experimental Set-Up 19
3.4 Visual experiments - Ethanol and Water 25
4 Results 27
4.1 CFD Analysis 27
4.2 Experimental studies 39
5 Conclusion 46
6 Further work 47
7 References 48
8 Appendix A-Populärvetenskaplig sammanfattning 51
9 Appendix B-Simulation of Dynamic Mixer in COMSOL MULTIPHYSICS 53
10 Appendix C-Analytical model 56
11 Appendix D-Experiments-ÄKTA Explorer 100 system 59
11.1 Conductivity experiments 59

1 Introduction

Proper understanding of mixing processes and transport phenomena in flow systems are of key importance in many chemical engineering applications. Inline mixing processes during continuous chromatography, a separation process in Bio-Tech, involves the mixing of a fluid carrying a dilute or concentrated species with solvent, aqueous or organic at different mixing and junction points in the process. This could be to adjust pH or reach the desired concentration of buffer or organic solvent content, prior going to a new unit operation in the process. Good mixing is also of key importance when discussing chemical reaction engineering, to facilitate desired conditions for chemical reactions. (Cortes-Quiroz, et al., 2017)

Models describing ideal mixing, perfectly mixed stirred tanks (CSTR) and plug-flow tubes (PFR), are used in chemical engineering for their simplicity and ease of modelling. In many technical and natural systems, spatial distributions, where the mixing can be considered "non-ideal", occur and has practical implications on for example, the rate of chemical reactions and effective heat removal from the system. For technical applications, it is therefore important to understand what are the governing dynamics and how it can best be described and perhaps be approximated by a mathematical model. Going further, non-ideal mixing can be described by either macro- or microscopic models. While the macroscopic models inherently become much simpler to work with, they also lack in resolution and description of the system. Microscopic models have the potential of giving a more accurate description and higher resolution of the processes within the system, while the complexity and number of parameters that needs to be calibrated to give exact estimations, increases drastically. As the modelling world only describes a simplified version of the natural world, experimental validation is important for comparison and critical validation of the theoretical models. In this thesis, both microscopic and macroscopic modelling coupled with experiments were used and compared.

The purpose of the thesis was to investigate and discuss optimization of fluid mixing in different mixing configurations, using Computational Fluid Dynamics (CFD) and experimental analysis. The numerical simulations of the Mixing Configurations were conducted using the commercial CFD-software, COMSOL MULTIPHYSICS. The goal of the analysis was to propose configurations and implement analytical tools for analysing mixing processes, which would be feasible to use in continuous chromatography processes. The CFD-analysis became quite general when it came to mix ratios, concentrations of solute used and different flowrates and as such more detailed studies is required for understanding and examining more specific cases, given the exact running conditions when conducting continuous chromatography. One of the sub-goals of the CFD-analysis was to simulate and quantify mixing of fluids with different density and rheological properties. Another sub-goal, was to conduct simulations of rotating machinery parts using dynamic moving mesh algorithms to model stirred tank reactors. The work done in this thesis was partly linked to other projects and processes run at the department, regarding relevant flow rates, mixer configurations and chemical solvents used. The CFD-analysis was coupled with experiments using the ÄKTA EXPLORER 100-chromatography system at the Department of Chemical Engineering at LTH, Lund University of Scania, Sweden.

2 Theory

In the following section some basic theory regarding mixer design are explained where some of the challenges of fluid mixing in the small scale are discussed. Also, quantification of mixing and different views and perspectives on fluid dynamics are briefly explained and finally, a short section is given to experimental theory.

2.1 Mixers

There are many types of designs and principles when it comes to fluid mixers, but they can, in general, be divided into two categories, passive or active. While active mixers rely on an external source of power or disturbance to enhance mixing efficiency, passive mixers functions without moving actuators. (Hardt & Schönfeld, 2007) Passive mixers can further be categorised as diffusion based or relying on a concept termed, chaotic advection, referring to the stretching and folding of fluid elements, induced by transverse flows in the mixing channel.

Some of the simplest designs involved in microfluidic mixing devices are T and Y shaped mixers, which also are commonly featured junction elements in many processes. (Galetti, et al., 2012) Mixing quality in T-mixers is highly dependent on the flow regime in the mixer, governed by the dimensionless Reynolds number, Re and the geometry of the mixer, or more precisely, its height to width ratio of the inlets and mixing channel. Re describes the ratio between the inertial, advective forces and the viscous forces in the fluid, where L_c is the characteristic length, v_c, characteristic velocity and υ is the kinematic viscosity. (Hauke, 2008) Re indicate the state of the flow and can be used to estimate flow stability and the transitioning in phase from laminar to turbulent flow. (Andersson, et al., 2012)

$$Re = \frac{L_c v_c}{\upsilon} \tag{1}$$

Previous studies on T-mixers for water-water (W/W)-systems with quadratic inlets and mixing channels have identified four different flow regimes. In the stratified flow regime at low Re, when the concentration field is a passive scalar quantity, the fluid streams meet at the mixing point and flow side by side through the mixing channels, resulting in two completely segregated fluid streams. (Andreusssi, et al., 2015) When mixing fluid streams in laminar stratified flow, the mixing in the cross-section of the mixing channel occurs by diffusion only, which is a comparatively slow process compared with advective transport, given the low diffusivities of molecules in liquids compared with gases. The ratio between the advective and the diffusive transport is given by the dimensionless Peclét number, Pe, where D_{AB} is the molecular diffusivity. For non-thermal fluids, Pe is given by the product between Re and the dimensionless Schmidt number, Sc, describing the ratio between momentum and diffusion.

$$Pe = ReSc = \frac{L_c v_c}{\upsilon}\frac{\upsilon}{D_{AB}} = \frac{L_c v_c}{D_{AB}} \tag{2}$$

In practice, for most liquid flow systems, the mass transfer is dominated by advective transport, resulting in large Peclét numbers which leads to impractically long mixing channels when the flow is stratified. For a solute-particle to traverse a mixing channel of width d by diffusion, requires the length of the channel to be, $L_{channel} \cong \frac{d^2 v_c}{D_{AB}}$. (Schikarski, et al., 2017) Diffusive mixing is facilitated by the shorter mixing distance, but can be made impractical for large size

molecules with low molecular diffusivities, thus requiring additional passive or active mixing methods. (Hardt & Schönfeld, 2007)

In the vortex regime at higher Re, a double vortex pair, called Dean vortices, appears at the confluence of the mixing point. As the vortex pair is left-right symmetric in the flow plane, there typically persists a well-defined region between the two fluids, thus the mixing predominantly is diffusive. At a critical Re for some geometries, the system goes through a bifurcation and the flow will go from being a steady-symmetric configuration to a steady-asymmetric, resulting in an engulfment region where transverse flows reach the other side of the mixing channel. The increased stretching and folding of the fluid elements in the engulfment region, significantly increases the efficiency of the mixing process when compared with stratified and flow in the vortex region. Above the engulfment regime, the flow behaviour starts to show unsteady behaviour, before transitioning in phase to full turbulence. (Andreusssi, et al., 2015)

Since the benefit of mixing in the engulfment region is obvious, there has previously been extensive research trying to establish the exact conditions under which this occurs, through experimental studies and numerical simulations using Computational Fluid Dynamics (CFD). Some mixer configurations have shown flow in the vortex regime at Re up to 1200 without engulfment, while other studies done by Dreher et.al, (2009), showed periodic unsteady flow behaviour for certain configurations for $240 < Re$. (Andreusssi, et al., 2015) Studies for water-ethanol (W/E)-systems have shown similar behaviour in flow configurations, the difference being the viscous boundary layer between the two fluids. (Schikarski, et al., 2017)

The increased efficiency in the engulfment region, it seems that stretching, folding and break-up processes of the fluid elements from the advective part of fluid motion, is the largest contributing factor for determining efficient mixing. Topological stirring by chaotic advection for low Reynolds flows, has been studied within the framework of dynamic systems theory, as far down as to creeping flow, Stokes flow. The term chaotic advection refers to the stretching and folding of fluid elements, induced by transverse flows in the mixing channel. (Hardt & Schönfeld, 2007) Chaotic advection and topological fluid mechanics of stirring was studied by (Aref & Stremler, 2000), where they used stirring protocols, periodic motions of mechanical stirrers, to produce chaotic patterns in 2-D flows at low Re. This concept has laid ground for development of mixing channels, where periodic changes in the geometry, is used as a passive method for enhancement of fluid mixing. The periodic perturbation of the flow field, referred to as an advection cycle, works by continuously mapping each flow configuration into the next cycle, which increases the stretching and folding of fluid elements without any external application of force. (Aref, 2002)

2.2 Quantification of mixing processes

To make exact estimations when analysing mixing processes and when considering implementation of different methods, analytical tools used to quantify and measure the rate and degree of mixing, becomes of significant importance. Common methods of quantifying mixing, traditionally used, are measurements of spatial variance using L^2- and L^∞-norm. For a mass concentration of a dissolved component, dependent on both space and time, $u(\boldsymbol{x}, t)$, in a domain, $\Omega \subset \mathbb{R}^n$, the L^2-norm is expressed as, $\|u\|_{L^2(\Omega)} = (\int |u(\boldsymbol{x}, t)|^2 d\boldsymbol{x})^{1/2}, \boldsymbol{x} \in \Omega$ and L^∞-norm, $\|u\|_\infty = sup_{x\in\Omega}|u(\boldsymbol{x}, t)|$, for each $t > 0$. Both measures are used to estimate how far a system is from being homogenous and at what rate it is becoming mixed, but as it turns out, there exist no exact consensus on how to best evaluate mixing. The issue with L^2- and L^∞-norm is that in the absence of diffusion, the metric does not decay in time, meaning that the stirring action from advection

and small-scale variations in concentration in chaotic flow patterns, is not captured. (Mathew, et al., 2005)

Mixing and stochastic processes are also explained within the framework of ergodic theory and the study of the Lagrangian formulation of fluid kinematics through dynamical systems theory. The Lagrangian form of the motion equations describing flow, is given by the advection equations where the flow is described by a system of Ordinary Differential Equations (ODEs), describing the trajectory of each fluid particle. (Aref, 2002) Thus, in the Lagrangian setting, each point $\boldsymbol{r}(t) = (x(t), y(t), z(t))$, in space refers to an individual fluid particle and the velocity can be determined by simply differentiating its position with respect to time. In Cartesian coordinates, the advection equations read as follows

$$\begin{cases} \frac{dx}{dt} = u(x, y, z, t) \\ \frac{dy}{dt} = v(x, y, z, t) \\ \frac{dz}{dt} = w(x, y, z, t) \end{cases} \tag{1}$$

where u, v and w are referred to as the stream functions of the flow. The stream functions are given by solving a set of dynamic equations describing the flow field, i.e. the Navier-Stokes or Euler equations. The phase-portrait describing the distribution of fluid particles in a static mixer with helical shaped impellers, simulated in COMSOL MULTIPHYSICS, is depicted in figure 1, where increased mixing of an initial distribution of fluid particles can be seen, as the fluid flows through the mixer.

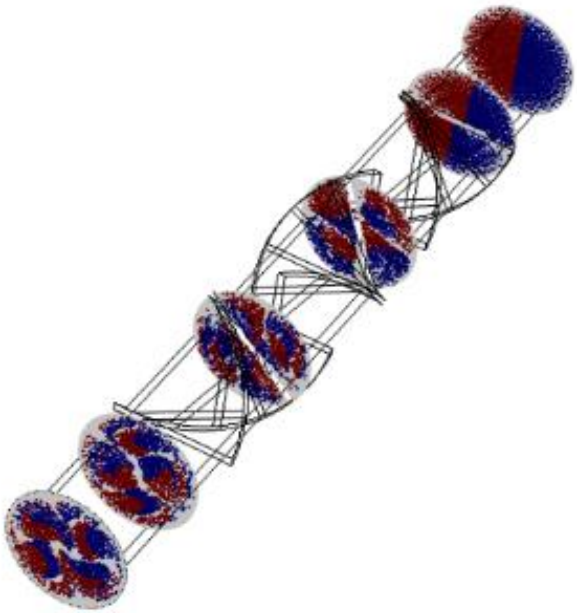

Figure 1: Phase Portrait of Particle Distribution in Passive Mixer.

2.3 Governing equations – Computational Fluid Dynamics(CFD)

In comparison to the Lagrangian description, in the Eulerian frame, each point in space is fixed and the flow is described as a field, rather than tracking the trajectory of every fluid particle. Thus, information of the flow in the Eulerian setting, only describes the velocity at fixed points

and gives no information about the motion or position of individual fluid particles. The visualisation of the flow field is given by stream-lines, the lines tangential to the velocity vector at each fixed point in space, generated from solving the set of equations, describing the flow field. For applications in general, the Eulerian formulation is most commonly used, as it yields the simplest formulations. (Hauke, 2008)

The governing equations in CFD, describing the conservation of heat, mass and momentum within a flow system, are described by Partial Differential Equations (PDEs). Partial Differential Equations are a fundamental field within mathematics and can broadly be categorized as being hyperbolic, parabolic or elliptic depending on type and the characteristics of the equation or system of equations. The simplest examples are respectively, the three fundamental equations, wave-, heat/diffusion- and Laplace´s or Poisson´s equation. (Sparr & Sparr, 1999/2000) The benefit of classifying equations using characteristics, helps the analyst to describe and predict the nature of singularities and approximating methods, used for finding a solution. The typical problem involved in PDEs, is finding or approximating a solution under a set of certain boundary conditions and/or initial conditions, leading to well-posed problems. (Renardy & Rogers, 2004)

The Eulerian formulation of fluid dynamics as it is derived from continuum theory, is described by the Navier Stokes-(NS) and Euler equations and is as such valid if the continuum hypotheses holds. Isothermal flow described by the NS-equations in its conserved form, is a system of non-linear equations depicted below in tensor form, using index notation for the spatial variables given in Cartesian coordinates, in three-dimensional space, $\{x_i\}_{i\in\mathbb{N}^+} = \{x, y, z\},\ i \neq j = 1,2,3$, $\partial_i = \frac{\partial}{\partial x_i}$. The first equation is the motion equation and the second is the continuity equation, where τ_{ji} is the viscous stress tensor and K_i denotes an arbitrary force load, applied to the fluid. (Andersson, et al., 2012)

$$\frac{\partial(\rho v_i)}{\partial t} = -\partial_j\left(\rho v_j v_i\right) - \partial_j \tau_{ji} - \partial_i p + K_i \tag{2}$$

$$\frac{\partial \rho}{\partial t} = \partial_i(\rho v_i) \tag{3}$$

If the flow is considered incompressible, $\partial_i v_i = 0$, with summation over indices 1-3, the divergence of the velocity field is zero and is an approximation made for liquid flow, when there is no spatial or temporal distribution or change in the density of the fluid and corresponds to the dilation of the fluid volume. (Hauke, 2008) For a Newtonian fluid, the viscous stress in the fluid depends only linearly on the gradient of the velocity field and the constitutive relationship between viscous stress and the velocity gradient or shear rate, is given by Newton's law of viscosity, seen below using index notation where μ is the dynamic- or shear-viscosity. (Alveteg, 2015)

$$\tau_{ji} = \mu \frac{\partial v_i}{\partial x_j} \tag{3}$$

Flow close to a solid boundary, the viscous stress causes the fluid to have infinitely slow velocity in the tangential direction, referred to as the no-slip boundary condition. This phenomenon creates something which in fluid dynamics is referred to as a boundary layer. The main theory related to this kind of phenomenon, explaining the development of laminar viscous, thermal and mass-transfer boundary layers close to solid surfaces, is explained by Prandtl's boundary

layer theory. (Hauke, 2008) The thickness of a viscous boundary layer developed over a flat surface can be estimated from the following expression, where δ_L is the viscous boundary layer thickness, defined as the thickness of the layer containing 99% of the shear-volume profile, L is a point given along the plate surface and Re_L is the dimensionless Reynolds number at the point of interest.

$$\delta_L = \frac{L}{\sqrt{Re_L}} \tag{4}$$

In analogous fashion, estimation of mass and thermal boundary layers can be estimated using the dimensionless mass and thermal Peclét numbers, by substituting between the Schmidt and the Prandtl numbers, respectively. (Hauke, 2008)

The NS-equations are by their nature, complicated and to this day there still exist no analytic solution for the general case. (Alveteg, 2015) A simpler model describing fluid flow when the viscous effects can be neglected, referred to as inviscid flow, is given by the Euler equations.

$$\frac{\partial(\rho v_i)}{\partial t} = -\partial_j\left(\rho v_j v_i\right) - \partial_i p + K_i \tag{5}$$

Usually, (5) is valid if $Re \gg 1$, i.e. the advective forces dominates over viscous. (Hauke, 2008) However, this assumption only applies to flow "far" from solid boundaries, since shear-stress effects close to the solid boundaries affects the flow stability as well as creating viscous boundary layers at low Reynolds numbers. One of the key findings of Prandtl was that as the fluid moves away from a solid surface the flow becomes more and more inviscid and the friction effects from the solid boundaries decreases. (Alveteg, 2015)

Considering the molar flux in an isotropic medium for a non-reacting, ideally diluted species subject to both advection through the flow-field and diffusion, the continuity equation in 3-D, is described by the source/sink free Diffusion-Advection equation, given below in index form.

$$\frac{\partial c}{\partial t} = D_{AB}\partial_i{}^2 c - v_i\partial_i \mathrm{c} \tag{6}$$

2.3.1 Discrete models

The governing equations are, in general, too complicated to solve analytically and often numerical methods and discrete models are used for approximate solutions. Examples of discrete and numerical models are Finite Element Methods (FEM), Finite Difference and Finite Volume Methods (FVM).

Diffusion in liquid flow is also difficult to accurately simulate, given the very low transport distance compared with advection. The average transport distance from diffusion can be estimated from $x = \sqrt{D_{AB}t}$, which can be compared to the expression $L_{channel} \cong \frac{d^2 v_c}{D_{AB}}$, used for estimating the length of a mixing channel. (Andersson, et al., 2012) Due to high diffusion Pe numbers in liquids compared to gases, this leads to almost always advection dominated problems, i.e. eqn. (6) is hyperbolic. The added numerical difficulty presented from the advective term and the added hyperbolicity, introduces difficulties which needs additional care when prescribing boundary data and introducing stiffness to the mathematical model. From physics and boundary layer theory, a simple example is illustrated by the following initial-, boundary-value problem for a quasi-1-D case of eqn. (6), with fixed Dirichlét boundary conditions and initial condition, describing a mass transfer boundary layer. (Hauke, 2008)

$$\begin{cases} \frac{\partial u}{\partial t} = D_{AB}\partial_x{}^2 u - v_c \partial_x u & 0 < x < L, t > 0 \\ u(0,t) = 1, u(L,t) = 0 & t > 0 \\ u(x,0) = 0 & 0 < x < L \end{cases} \tag{7}$$

Now, only considering the stationary case

$$\begin{cases} D_{AB}\partial_x{}^2 u = v_c \partial_x u & 0 < x < L \\ u(0,t) = 1\, u(L,t) = 0 \end{cases} \tag{8}$$

Where the exact solution is given by

$$u = \frac{e^{\frac{v_c}{D_{AB}}L} - e^{\frac{v_c}{D_{AB}}x}}{e^{\frac{v_c}{D_{AB}}L} - 1} \tag{9}$$

There exist several different discrete methods, as previously mentioned to approximate a solution to eqn. (9). As COMSOL MULTIPHYSICS is FEM based, the equivalent FEM formulation of eqn. (8) is derived. For more texts and a more thorough explanation of functional analysis and FEM, we refer you to (Renardy & Rogers, 2004) and (Iserles, 2009).

Multiplying eqn. (8) with an arbitrarily chosen weight function, $w \in V = H^1(\Omega)$ and integrating over the domain $\Omega = (0, \mathrm{L})$, then u is a weak solution to eqn. (8) in $H^1(\Omega)$ if the following holds

$$\begin{cases} D_{AB}(\Delta u, \nabla w)_{L^2(\Omega)} + v_c(\nabla u, w)_{L^2(\Omega)} = 0 & \forall w \in V \\ u(0,t) = 1\, u(L,t) = 0 \end{cases} \tag{10}$$

where $(u,v)_{L^2(\Omega)} = \int_0^L u(x)v(x)dx$, denotes the inner-product in the space of $L^2(\Omega)$-functions. (Renardy & Rogers, 2004) We now seek the approximate weak solution u_h, in the finite-dimensional subspace V_h, with N nodal-interior points and get the following expression after performing an integration by parts.

$$D_{AB}(\nabla u_H, \nabla w)_{L^2(\Omega)} + v_c(\nabla u_H, w)_{L^2(\Omega)} = [D_{AB}\nabla u_H w]_L^0, \forall w \in V_h \tag{11}$$

Since V_h is finite dimensional, we choose a set of basis-functions, $\{\phi_i\}_{i=1}^N$, and then wish to express u_H as a linear combination of these functions, where U_i are the nodal concentrations.

$$u_h = \boldsymbol{u_h} \cdot \boldsymbol{\phi} = \sum_{i=1}^N U_i\, \phi_i \tag{12}$$

Using the Galerkin's method and choosing the basis-functions as weight function, gives a system of linear equations in matrix form

$$\boldsymbol{A u_h} = \boldsymbol{f_b} \tag{13}$$

Where $\boldsymbol{A} = (a_{ij})$ and a_{ij} is given by the functionals, $D_{AB}\left(\nabla\phi_i, \nabla\phi_j\right)_{L^2(\Omega)} + v_c\left(\nabla\phi_i, \phi_j\right)_{L^2(\Omega)} = D_{AB}\int_0^L \nabla\phi_i \nabla\phi_j dx + v_c \int_0^L \nabla\phi_i \phi_j dx\,, i-1 \le j \le i+1, i \in N$

The issue with the approximate solution, is that it has been shown to contain unphysical oscillations under certain circumstances. Below, eqn. (12) can be seen in figure 2, for different Peclét

values, $N = 50, L_c = L = 1\ [m]$ and $D_{AB} = 10^{-9}\ \left[\frac{m^2}{s}\right]$, using linear elements as basis-function, which shows increasing oscillations closing in on the right boundary.

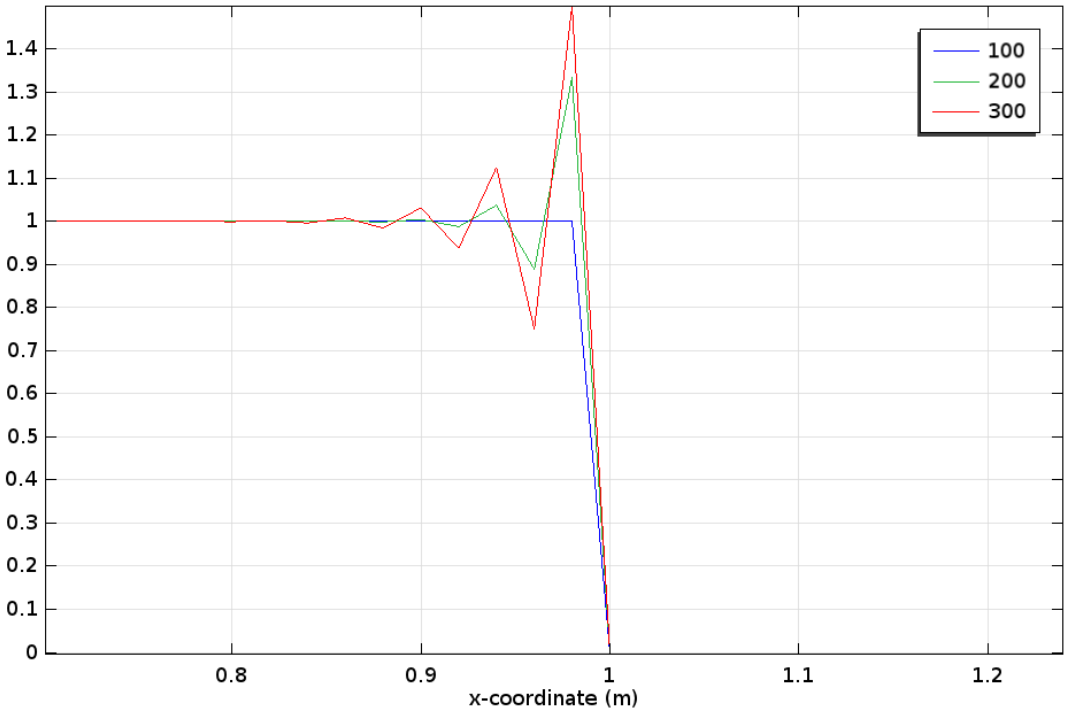

Figure 2: Increasingly oscillatory behaviour of the numerical solution, using FEM and linear element approximation.

For a 1-D case such as the one described above, it is well understood when using linear elements on a uniform grid distribution with constant mesh size, h, different values on left and right boundary and constant velocity, that oscillations occur when the mesh Peclet number, Pe_N, is greater than 1, i.e. $Pe_N = \frac{|v_c|h}{2D_{AB}} > 1$, thus requiring very fine mesh sizes to resolve. (Elman & Ramage, 2001) In two or more space dimensions, the result mentioned above does not hold and things get more complicated.

There are however, remedies to this kind of behaviour, that increases the numerical stability and consistent stabilisation methods by adding numerical streamline and crosswind-diffusion of the advective term are checked by default in COMSOL MULTIPHYSICS, when working within the physics modules. There are also options for adding so-called, inconsistent artificial diffusivity over each mesh element. (MULTIPHYSICS, 2013)

Due to the difficulties related to the continuum based models in liquid flow, accurate simulations using particle tracking and Lagrangian Particle dynamics has proven a successful alternative. In general, continuum models are not capable of handling systems with Peclét values over 1000. In the Lagrangian setting, the fluid particles motion is independent of the Peclét number and modelling advective transport of molecules can be done by adding drag forces between the background flow field and the immersed particles. Particle diffusion can also be modelled by adding Brownian forces which provides an alternative from studying diffusion using continuum models. (COMSOL, 2012)

2.4 Macroscopic Non-ideal mixing models

An alternate approach of describing non-ideal mixing is to model and describe it macroscopically using lumped parameter models. Non-ideal mixing is described on a macroscopic level by a phenomenon referred to as dispersion, which describes the stochastic process of mass transfer, analogous to molecular diffusion. As such macroscopic dispersion can be described mathematically in a similar way as molecular diffusion, by just changing the physical constant in the constitutive relationship. (Warfvinge, 2015) Axial dispersion in laminar pipe and tube flow is induced by the laminar flow profile and is referred to as Taylor dispersion. The mass conservation of a component subject to both advection and dispersion without any source or sink term is described by the same continuity equation as the advection diffusion equation given by eqn. (6). However, the ratio between advection and dispersion is usually lower compared with the ratio between advection and molecular diffusion and as such, the dispersion coefficient, D_{Ax} is several orders of magnitudes larger compared with D_{AB}, leading to less hyperbolicity.

2.5 Experimental theory and Conductivity Measurements

Experimental measurements are essential when validating theoretical hypotheses that are developed through mathematical modelling. A proper understanding of measuring theory and how experimental based studies are conducted are therefore important for making experiments that are relevant and corresponds with the theoretical models and vice versa.

Conductivity measures the capacity of a medium to conduct electricity. The method is non-specific, since it simply detects the presence of dissolved ions, regardless of type of species and is a commonly used tool for analysing drinking water quality and when estimating the ionic strength in a solution. The total amount of dissolved ions in a solution can be estimated as amount of Total Dissolved Solids (TDS) which is estimated by multiplying the conductivity by an estimated conversion factor depending on the dissolved species and is in the range of between 0.55 and 0.70. (Analytical, 2018) Estimation of concentration of a dissolved species from conductivity measurements can only be done, within certain intervals where there exists proportionality between the conductivity and the concentration of dissolved ions. Furthermore, to be able to estimate the ion concentration of a certain species of interest in the solution, it becomes important to prevent the dissolution of other charged species that can affect the measurements. The relationship between conductivity and ion concentration is dependent on the dissolved species, but a generic example can be seen in figure 3 below, where the non-linear relationship between conductivity and concentration is shown. (Sciences, 2012)

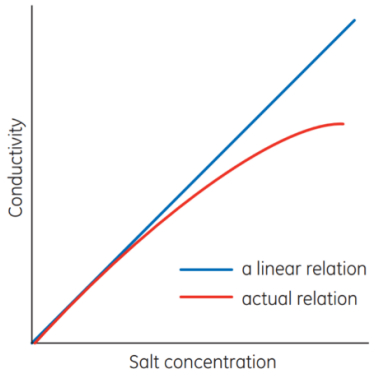

Figure 3: Relationship between conductivity and ion concentration, showing simplified linear- and actual relation at higher concentrations of dissolved ions.

3 Material and Method

The method section is divided into two parts. The first part is based on Computational Fluid Dynamics (CFD), using COMSOL MULTIPHYSICS to investigate the effectiveness of mixing configurations for different fluid systems in 3-D. To validate the models and theoretical hypotheses developed through CFD, the second part consisted of an experimental study of T-mixers and active mixers using ÄKTA EXPLORER 100-chromatography system. The experiments were analysed using analytic and discrete models and through visual observations.

3.1 CFD analysis

The outline of the CFD-analysis, was describing mixing of fluids in different mixer configurations and simulations of fluids with different density and rheological properties. Continuum based models were used to describe rheological and material properties as equations of state which was not possible when simulating advection and diffusion using particle tracking methods. When analysing mixing efficiency, spatial distributions were analysed using L^2-variance and a spatial measure based on mass fluxes. Thus, it became more convenient for the analysis, to work with continuum models rather than *Particle Tracing*, using Lagrangian particle dynamics.

Two Newtonian fluid systems were created, one water-water system (W/W), where the transport of solute, dissolved NaCl, was modelled as an ideal diluted species. The other fluid system was a water-ethanol system (W/E), where mixing of two fluids with different physical properties regarding viscosity and density was simulated.

3.1.1 W/W system

Assuming iso-thermal flow, the domain equation describing the flow field, was the in-compressible NS-equations in 3-D. The component mass balance of the solute was modelled as a passive scalar quantity, by the advection-diffusion equation, given below in divergence form, where ∇ and Δ is the Nabla- and Laplacian-operator, respectively. There is density and viscosity differences between different concentrations of NaCl, seen in figure 4 below, but the difference between 0 and 1 M NaCl solution is approximately 4.0 % for the density and 8.3 % for the dynamic viscosity, thus the solute was assumed ideally diluted for the modelling purposes. (Hai Lang & Han, 1996)

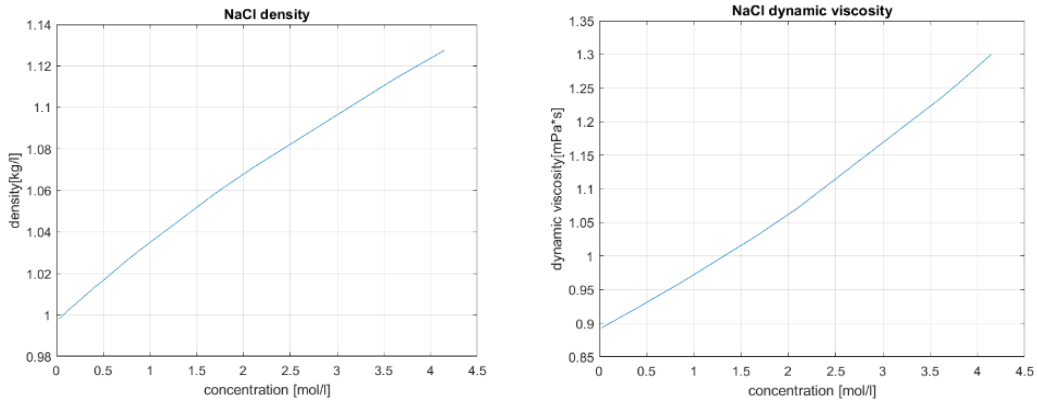

*Figure 4:Density [kg/l] vs [NaCl] [M] (left), and Dynamic viscosity [mPa*s] vs [NaCl] [M], (right).*

As such, the mixing can be considered as being between two water streams with equal rheological properties. The density and viscosity was set to the default values of water in COMSOL MULTIPHYSICS, assuming a temperature of 293.15 K. The diffusivity, $D_{AB,water}$ was set to $1.485 * 10^{-9}$, based on the diffusivity of NaCl in 1 M solution. (Vitagliano & Lyons, 1995)

$$\begin{cases} -\rho(\boldsymbol{v}\cdot\nabla)\boldsymbol{v} + \mu\nabla\cdot(\nabla\boldsymbol{v}) - \nabla p = 0 \\ \nabla\cdot\boldsymbol{v} = 0 \\ D_{AB,water}\Delta c - \boldsymbol{v}\cdot(\nabla \mathrm{c}) = 0 \end{cases} \tag{14}$$

3.1.2 W/E-system

The mathematical model describing the mixing of two miscible Newtonian fluids, ethanol and water, was created by coupling the transport equation of one of the components of the binary system with the overall continuity equation and momentum balance of the fluid by describing the effective viscosity and density of the fluid as equations of state. Since the fluid system was binary, Fick diffusion was assumed. The mixing was assumed to be isothermal and volume reduction effects from mixing ethanol and water was neglected. Denoting the mass-fraction of ethanol in water as $\phi \in (0,1)$, we thus get the following system of equations in divergence form where $D_{AB,EtOH}$ is the diffusivity of ethanol in water. The first equation is the momentum equation of the fluid, second equation is the overall material-balance and third is the component mass balance. Notice as the density is composition dependent, the fluid no longer can be treated as being incompressible.

$$\begin{cases} -(\boldsymbol{v}\cdot\nabla)(\rho(\phi)\boldsymbol{v}) - \nabla\cdot(-\mu(\phi)\nabla\boldsymbol{v}) - \nabla p = 0 \\ \nabla\cdot(\rho(\emptyset)\boldsymbol{v}) = 0 \\ \nabla\cdot\left(D_{AB,EtOH}\rho(\emptyset)\nabla\phi\right) - \rho(\phi)\boldsymbol{v}\cdot\nabla\phi = 0 \end{cases} \tag{15}$$

Since the viscosity in the domain is dependent on the composition, the diffusion coefficient should be dependent on the composition as well. For modelling purposes given the low diffusivities in fluids, it was assumed that the diffusion was negligible, and was set to $1.20 * 10^{-9}$, and no consideration of composition dependent diffusivity was made. For further work it should however be straight-forward to implement a composition dependent diffusion coefficient, using an appropriate model. The functions for the density and viscosity were fitted with experimental data using a least square fit method, **polyfit**, in **MATLAB** and can be seen in figure 5 below. (Dizechl & Marshall, 1982)

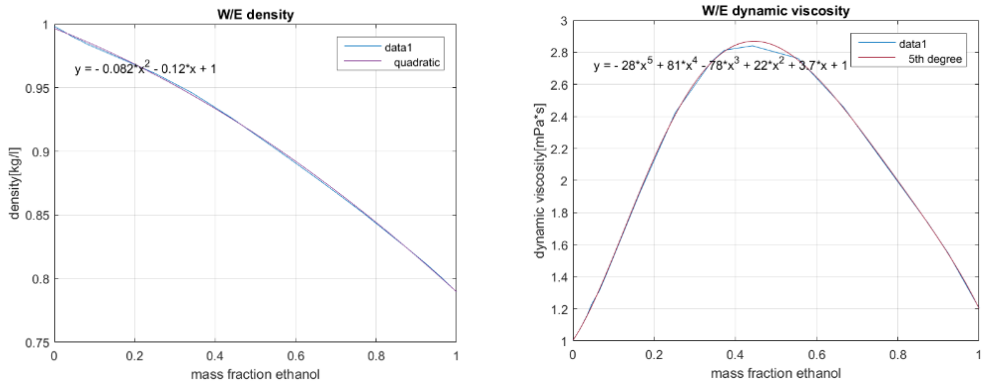

*Figure 5: Effective Density [kg/l] (left) and Effective Dynamic Viscosity [mPa*s] (right), expressed as functions of mass fraction ethanol.*

3.1.3 Simulation Method

This section describes the method of simulating flow for different Re, investigating vortex and engulfment in a T-mixer for the two fluid systems and flow simulations in the stratified flow regime, for different in-line mixer-configurations. Nearly all simulations that were conducted in the CFD analysis was stationary. The governing equations for the fluid systems were derived and compared with works done by Andreussi, et al 2015, for the W/W-system and Schikarski, et al 2016 and Orsi, et.al 2013, for the W/E-system and implemented in the physics modules, *Single Phase Fluid Flow-Laminar Flow, Transport of Diluted Species* for W/W and *Transport of Concentrated Species*, for W/E, available in COMSOL MULTIPHYSICS. The W/E-system was only simulated in the T-mixer.

The geometry of the T-mixer was based on a basic plastic T-cross design used in ÄKTA processes. A cut-open plastic T-cross used in ÄKTA and corresponding COMSOL model, can be seen below in figure 6, where the rotating grooves are used for coupling the different tubing in the process to the internal T-mixer geometry, seen in the middle of the picture. This makes the junction point quite arbitrary and varying depending on inlet and outlet tubing, but for the sake of modelling simplicity, we assumed that the most interesting parts regarding mixing are occurring inside the internal plastic structure of the T-mixer.

The cylindrical geometry has an aspect ratio, height to width ratio, of 1 and a characteristic length, estimated from the inner-diameter, D, of 1mm for both the inlets and the mixing channel. The length of the mixing channel, $L_{channel}$ was set to $10D$ in the simulations, for not imposing the outlet boundary condition too strongly to the flow at the confluence point. Similarly, the inlets were extended, to allow having a freer flow at the mixing point. For modelling the T-mixer for different Reynolds, it was found that using a coarser mesh with mesh refinement around the cylindrical walls and second order discretization for the transport equation of the solute was more robust, compared with decreasing the grid size and lowering the discretization level for both W/W and W/E. Also, due to the junction between the cylindrical geometries, singularities arose at the junction point when trying to decrease the grid size which lead to divergence in the stationary solver sequence.

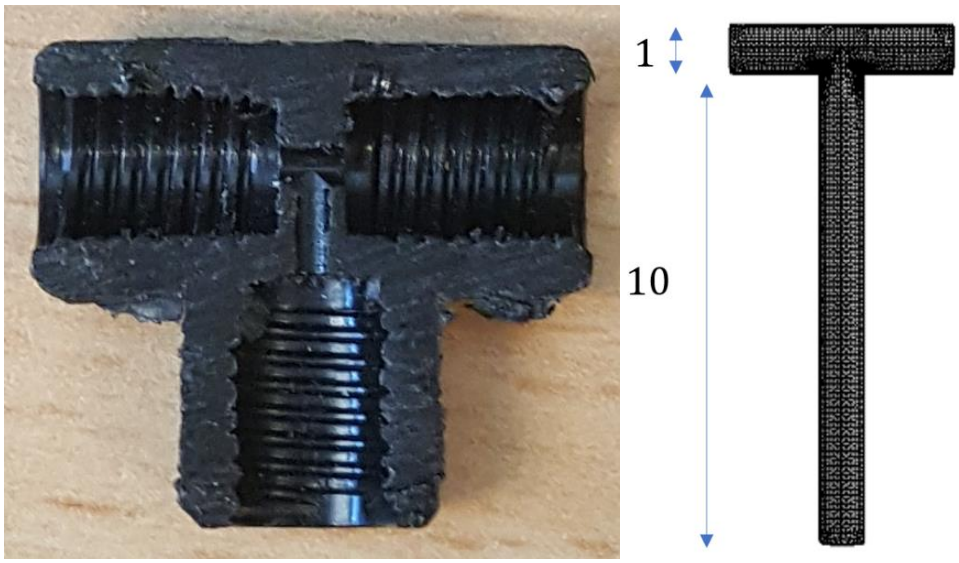

Figure 6: Cross-section cut of plastic T-cross used in ÄKTA processes and COMSOL MODEL.

Three different mixer configurations were simulated and compared based on the degree of homogeneity at the outlet, for a given flowrate of 1 ml/min at each of the inlets. One with attached curved helical-shaped rotating baffles, one with obstructing walls, referred to as an advection model and one serpentine model. The baffle mixer was modelled and implemented from design created by COMSOL MULTIPHYSICS. To compare mixing performance of the different configurations, the geometries were scaled to yield a similar hydraulic diameter, $d_h = \frac{2wh}{w+h}$, estimated from the width and height of the mixing channel. We then put, $L_c = d_h$ and $v_c = \bar{v} = \frac{Q}{A} = \frac{4Q}{\pi {d_h}^2}$, for estimation of Re and Pe, in the stationary mixer configurations.

For the static mixer, the design of the geometry comes in two parts. The first part is a cylindrical pipe, which is larger (in volume) than the tubes used to transport the fluids. The second part is the helix shaped baffles inside the pipe. These pipes are used to ensure that the fluids entering the mixer are getting mixed. The baffles consist of three twisted blades, each blade with an alternating rotation than the other blades. The usage of COMSOL's extruding tool made it possible to build the blades. First, a rectangle is built which is then extruded to transform it into a block, after that these blocks were twisted at a 30 degrees angle. The last thing to do is to copy the first blade and paste it twice with a 30 degrees rotation of set for each blade. Figure 7 below shows the static mixers in two parts, the pipe part and the blade part. (COMSOL, 2015-2017)

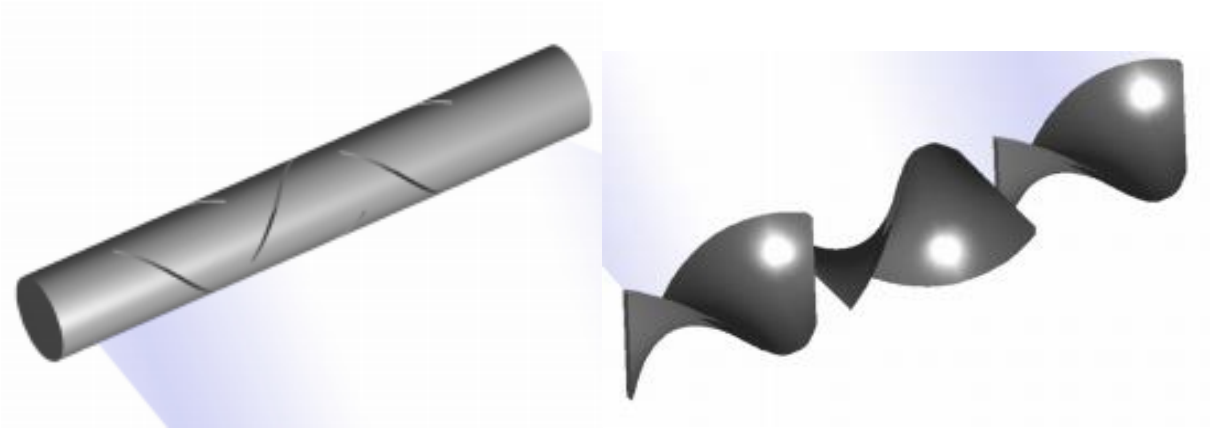

Figure 7: Stationary mixers with rotating stationary blades.

The length of the advection model and the helical bladed mixing chamber was 30 mm. The width of the advection model was 6 mm and height 3 mm. Each wall in the mixing channel was 3mm wide. The serpentine model mixing channel geometry was square in the flow direction, with a width and height of 3 mm. All geometries are depicted on the next page, in figure 8. The serpentine and helical mixer had a slightly lower hydraulic diameter, d_h, 3 mm, compared with the advection model, 4 mm. This corresponded to a Re of approximately 14 and 10 and Pe of approximately 9570 and 7145, respectively. Due to the larger diffusive Pe values compared with Re, the diffusion thus required a higher resolution, finer mesh and higher order discretization, compared with the flow field. Also, due to the decoupling between NS and the advection-diffusion equation for the W/W-system, it was possible to use a segregated solver procedure and first solve NS on a coarser mesh and then map the velocity field to the finer mesh used to simulate the diffusion of solute in the domain, to save computation time. (COMSOL, 2015-2017)

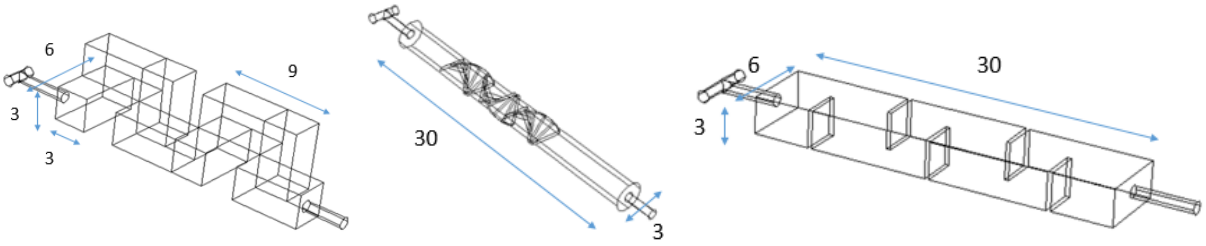

Figure 8: Three different stationary mixer geometries, serpentine-, helical baffle shaped and advection model. [mm]

For the advection and serpentine model, it was found that a finer mesh and lower level of discretization was more robust compared with using a coarser mesh and higher level of discretization. Also for resolving the diffusive flux in the domain, the mesh resolution closer to the walls were switched off in favour of a finer mesh structure in the domain. Due to the large number of sharp corners in the advection model, the number or singularities when using the default mesh setting was found to be unacceptably high. This issue was solved by defining the wall thickness of the sectioning walls to be equal to the size of the smallest mesh element of 0.305 mm. This effectively, eliminated all singularities around the sharp corners of the geometry. For the serpentine model, a similar meshing procedure was used, the largest mesh element was set to 0.12 mm and the smallest to 0.0012 mm, which gave a very fine mesh structure without singularities in the geometry. For the helical mixer a finer mesh coupled with a second order shape function was used for modelling the diffusion. Increasing the mesh refinement for the helical mixer started to create oscillations and non-physical levels of concentrations, assumed to be caused by over-interpolation, compared with the coarser mesh.

It was assumed that the laminar flow profile at the inlets, in all simulations, was fully developed for a set flowrate, with a ratio of 1:1 between the inlets. A no-slip boundary condition was enforced for the solid walls of the geometry and a back-pressure constraint of 0 Pa was set at the outlet. The inflow of concentration to the domain for both the W/W-system and the W/E-system was simulated as a flux-Dankvert's boundary condition with a prescribed solute concentration of 1 M NaCl and mass fraction of 0.55 (≈70- vol%) ethanol at one inlet and zero concentration on the opposing inlet. The outlet boundary condition for the component mass balance was modelled as homogenous van Neumann boundary conditions, which can be seen in figure 9 for the T-Mixer.

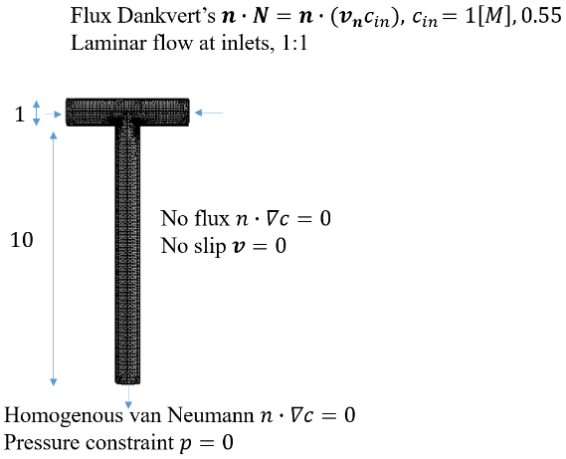

Figure 9: Boundary conditions for T-Mixer.

3.1.4 Mixing Efficiency and estimation of dimensionless Reynolds number

To quantify the degree of mixing and homogeneity at the outlet of the mixing channel, a mixing efficiency was defined as the standard deviation from the average normalised concentration at the outlet, $\bar{\phi}(\boldsymbol{r})$, $\boldsymbol{r} = (x, y, z)$. The L^2-variance of the scalar concentration field can be seen below and is defined by the following expression, where $\phi = \frac{c}{c_{in}}$ is the normalised concentration of NaCl or mass-fraction of ethanol at the outlet and where S corresponds to the outlet surface area.

$$\sigma^2{}_1 = \frac{1}{S}\iint (\phi(\boldsymbol{r}) - \bar{\phi}(\boldsymbol{r}))^2 \, dxdy \tag{16}$$

$$\bar{\phi}(\boldsymbol{r}) = \frac{1}{S}\iint \phi(\boldsymbol{r}) \, dxdy \tag{17}$$

$$S = \iint dxdy \tag{18}$$

The mixing efficiency was also estimated for the W/E-system based on material fluxes, using the following expression where δ_m is the mixing efficiency and σ_{max} is the maximum value of the variance, achieved when the fluid streams are completely segregated and not mixed. (Orsi, et al., 2013)

$$\delta_m = 1 - \frac{\sigma_2}{\sigma_{max}} \tag{19}$$

$\sigma_2{}^2$ is defined as a mass flow variance by the following expression

$$\sigma^2{}_2 = \frac{\iint \left(\left(\phi(\boldsymbol{r}) - \bar{\phi}(\boldsymbol{r})\right)^2\right) v(\boldsymbol{r})\rho(\boldsymbol{r}) dxdy}{\iint v(\boldsymbol{r})\rho(\boldsymbol{r}) dxdy} \tag{20}$$

and σ_{max} is the value when the streams are completely segregated, thus we expect (19) to increase towards 1, with better mixing. (Orsi, et al., 2013)

$$\sigma_{max} = \sqrt{\bar{\phi}(\boldsymbol{r})(1 - \bar{\phi}(\boldsymbol{r}))} \tag{21}$$

The mixing efficiencies were estimated, during simulation post-processing, as global variables using an integral, (**intop1()**) and an average-operator, (**aveop1()**), defined at the outlet boundary of the models, operating on the model variables, concentration of NaCl, (**c**), mass fraction ethanol, (**w2**), effective viscosity, (**dyn_visc_effec**), effective density, (**rho_effec**) and velocity, (**v**), which can be seen in figure 10 and 11.

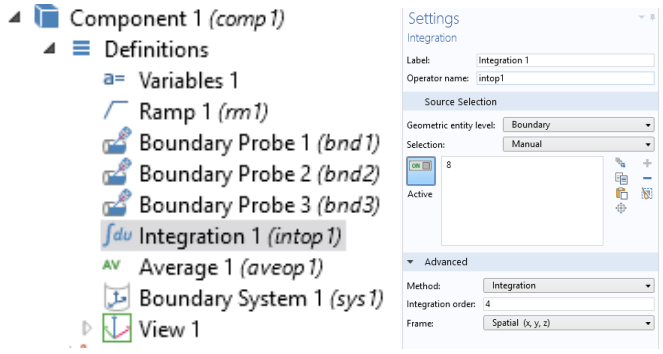

Figure 10: Definition of integration and average boundary operators.

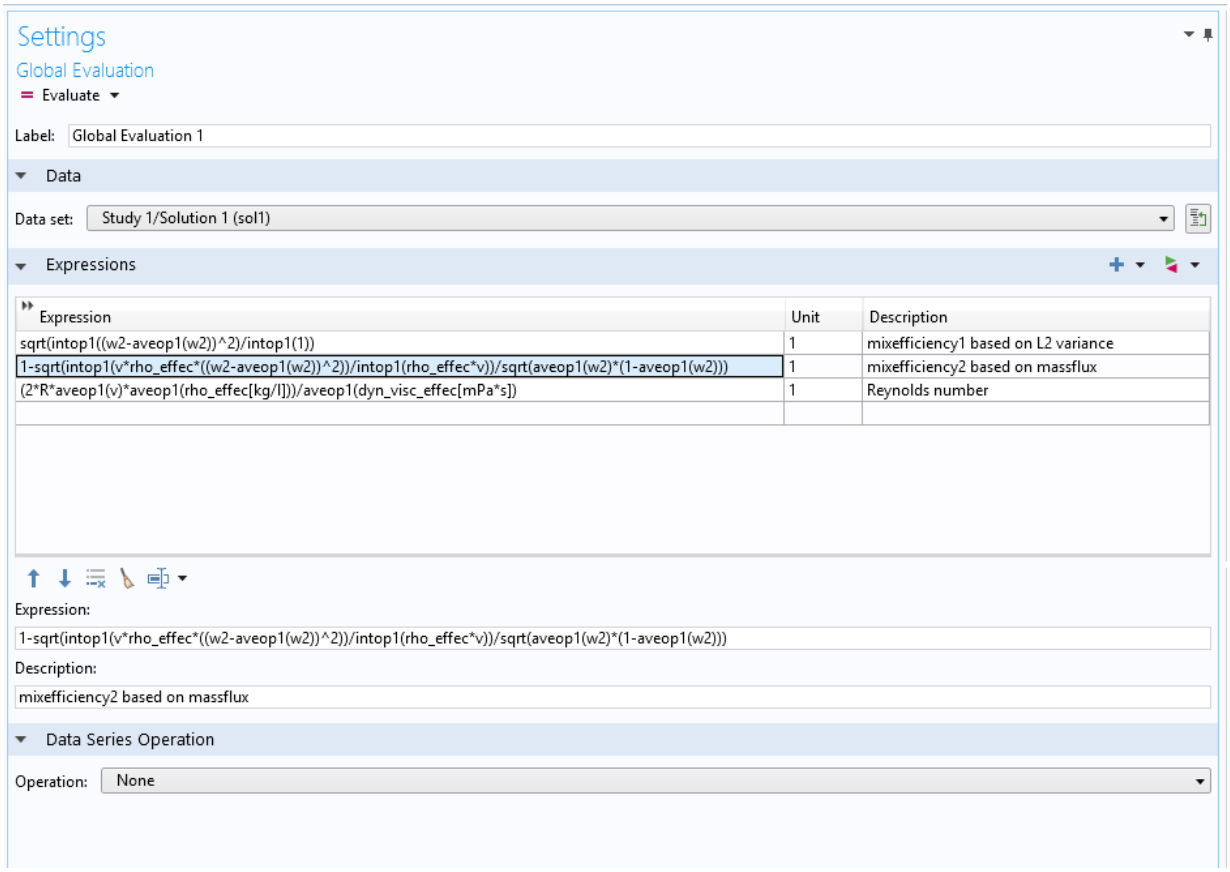

Figure 11: Post-processing of model variables using global evaluation of integral and average operators.

The mixing efficiencies were compared for different Re at the outlet of the mixing channel and for the different stationary mixer configurations. Due to the not necessarily consistent volumetric flowrate in the domain for the W/E-system, an average value of the velocity, effective density and effective viscosity was estimated using an average-integral operator, defined at the outlet boundary of the mixing channel.

$$\bar{v} = \frac{1}{S}\iint v(x,y)\,dxdy \tag{22}$$

$$\bar{\rho}_{effec} = \frac{1}{S}\iint \rho_{effec}(x,y)\,dxdy \tag{23}$$

$$\bar{\mu}_{effec} = \frac{1}{S}\iint \mu(x,y)\,dxdy \tag{24}$$

Given the numerical difficulties related to using continuum models to model mass distributions, several requirements were used to critically verify and analyse the simulations and the evaluation criteria for the numerical methods when analysing the continuum models was based on solutions that were physically relevant. As such, the requirements were, positivity, there exist no negative concentrations and stability, the solution should not oscillate meaning that the solution is expected to be smoothly varying and thus special care needs to be considered where there is expected sharp gradients in the concentration field and finally boundedness and robustness, there exist no infinite concentrations. The methods should also fulfil the accuracy requirements and having a proportionally low computational load.

3.1.5 Stirred mixer

Geometry of the dynamic mixers was based on standard dynamic mixers used in ÄKTA EXPLORER 100-chromatography system, where two different sized magnetic agitators can be seen below in figure 12. Two mixers with different height of the mixing chamber were created. Some dynamic mixers used in ÄKTA, have flat surfaces atop the rotating agitator and some have more of a curved ball shape at the top so both geometries where built and compared. While some agitators have more curved blades to allow for smooth rotation closer to the stationary walls, in the simulations, the blades where modelled with sharp corners.

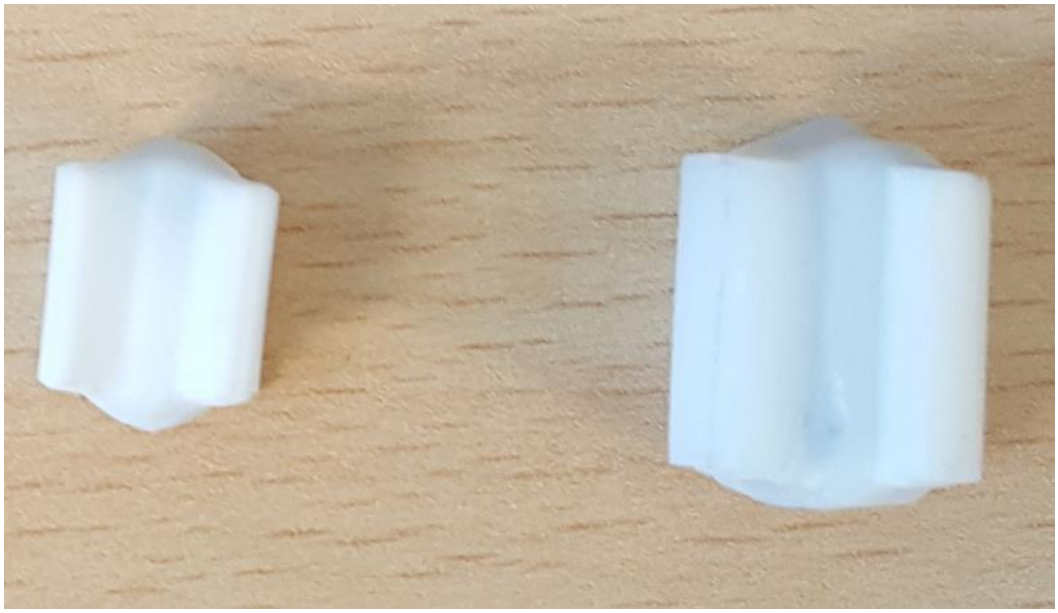

Figure 12: Different sized magnetic agitators used in ÄKTA dynamic mixers.

The characteristic length of the mixer was estimated to 15 mm, based on the diameter of the rotating agitator in the mixer. The Reynolds value was calculated from the following expression where N is the number of revolutions per second and D, is the impeller diameter. (Alveteg, 2015)

$$Re_{impeller} = \frac{ND^2}{v} \tag{25}$$

In both cases, the impeller size was of the same size, the only difference being the height of the cylindrical part of the mixing chamber. The discretization of the rotating domain was created using a moving mesh, which allows the user to have a mesh that changes dynamically around the moving parts of the geometry. There are different methods available in COMSOL MULTIPHYSICS to model moving mesh, but a relatively straight-forward method is available within the physics module *Rotating Machinery-Laminar Flow*. The method was implemented by creating two separate non-overlapping geometries, defining a moving and stationary part. The objects were then assembled to create an identity-pair, allowing the two objects to be treated separately, which coupled with a continuity condition between the stationary and rotating domain, implemented the moving mesh feature, which can be seen in figure 13. Due to the discontinuity in the flow field, very fine mesh structure is needed at the boundary between the stationary and rotating domain. The mesh structure of the dynamic mixers can be seen in figure 14. The full method, creating the geometry and implementing the moving mesh is given in appendix B.

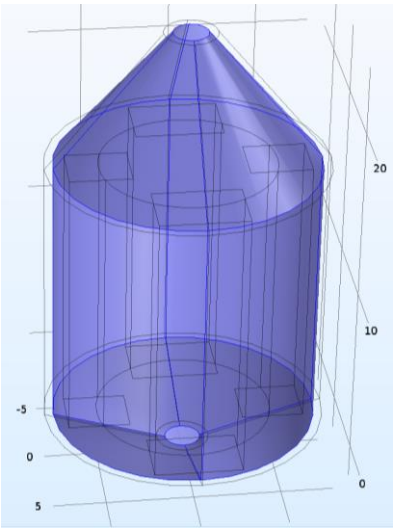

Figure 13: Flow continuity condition between stationary and rotating domain.

The rotating wall boundary condition, describing the continuity condition between the moving mesh and the velocity of the rotating agitator, can be seen in figure 15. The flow in the mixer was in the laminar region, as the number of revolutions per second was set to 10, positive angular velocity, corresponding to Re of approximately 2250, given by eqn. (25).

Figure 14: Meshed 3D model of magnetic stirred mixer side and top view.

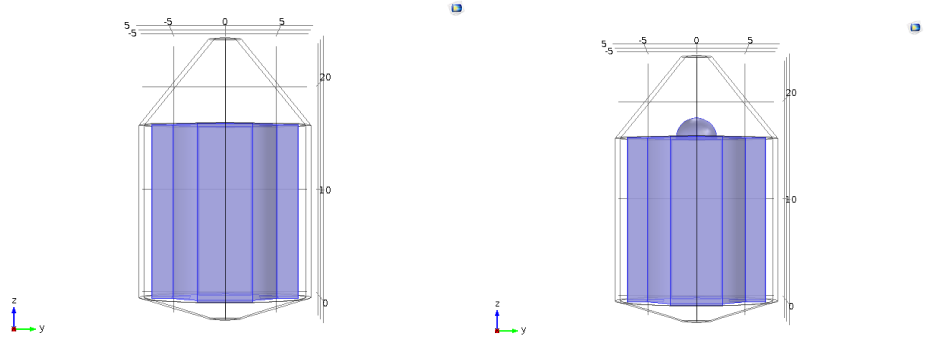

Figure 15: Rotating wall boundary condition with flat surface and ball shape above the rotating agitator.

The initial condition for the transient NS-equations was estimated from solving a quasi-steady state problem using a Frozen Rotor solution. The un-steady NS-equations could then be solved

directly from the Frozen Rotor solution, which is the preferred method when simulating steady state conditions, although the method is more computationally heavy compared with only doing Frozen Rotor simulations. The inlet conditions for the flow was set to an inlet flow-velocity of 0.025 m/s and the pressure was set to zero at the outlet. A no-slip boundary condition was enforced at the stationary walls of the mixer. Due to the close-gap between agitator and stationary wall, it is assumed that a boundary layer with sharp gradients in the velocity field will be seen. The estimation of thickness of the laminar boundary layer between the rotating agitator and the stationary walls was estimated from eqn. (4) by putting L equal to the inner circumference of the mixer, $L = D_{in}\pi,\ D_{in} \approx 15.5\ mm$ and $Re_L = Re_{impeller} = 2250$.

3.2 Experimental based modelling

Coupled with the CFD-analysis of mixing configurations, experiments with T-mixer and active mixers were conducted using the ÄKTA EXPLORER 100-system. The T-mixer used in the experiments was a similar T-mixer, as used in the CFD-analysis. Experiments that were run, were step response experiments using conductivity measurements of NaCl, for different flow rates, tube-lengths and mixing ratios. Experiments showed that reliable experimental data could be collected further away from the mixing point than was possible to model in 3-D, which lead to the usage of a simpler 1-D model when running the experimental study of measuring conductivity. Visual step response experiments using transparent tubes and colours were also used for experiments with ethanol and water. An experimental investigation was also done for the reciprocal-pumps in ÄKTA for different flowrates.

3.3 Experimental Set-Up

The experimental set-up when running the experiments consisted of two parts. The first part, which is the computer part, had all the software needed to send a signal to chromatography system, which is the ÄKTA EXPLORER 100-system, see figure 16.

Figure 16: Experimental Set Up of control system (left) and ÄKTA-system (right).

The system that runs ÄKTA is UNICORN. The system controls all running parameters of ÄKTA, such as flowrates and application of gradients. UNICORN also continuously data logs the experimental runs and stores the data in CSV files that are used for post-processing. The downside of running ÄKTA using UNICORN is that everything must be done manually that can lead to some errors when collecting the data and comparing the data to the model, which is why a script in PYTHON is made and executed through the ORBIT CONTROLLER. ORBIT is a control program written in the scripting language PYTHON, that makes the entire system run automatically, where it does everything step by step according to the time stamps set in the script. The scripts are generated in the PYTHON IDE, SPYDER, and the goal of the script is

to send a rectangular in signal to the system describing the actuation of a system control parameter such as increasing the flow of solute, by an approximately ideal step response. Assuming, that the in-signal to ÄKTA can be considered ideal, the equation describing a quadratic in-signal can be seen below in eqn. (26) and in figure 17 below. The measuring signal was given by the conductive meter as a function of time.

$$u(t) = Mixing\ ratio * (\theta(t-a) - \theta(t-b)) \tag{26}$$

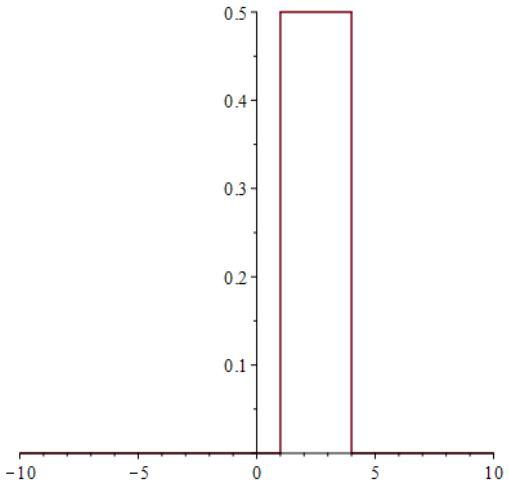

Figure 17: Quadratic in-signal sent to ÄKTA from ORBIT CONTROLLER.

A thing to consider before starting any type of experimentation on the process was to make sure that there was no type of additional delays and lag time between the system and Unicorn. Thus, before all experiments the system was run through a warm-up phase decreasing additional lag-time between the software and ÄKTA. Also, throughout the experiments, there was need to check if the system worked properly, according to the PYTHON-scripts, by checking flowrates and eventual disturbances.

3.3.1 Lag and response time estimation in ORBIT and ÄKTA

To correlate between simulations and experiments, efforts were made to try to establish the exact timeslots between in-signal from ORBIT, to measured signal response by comparing experiments for a known tube length of 0.64 m, with simulations. The tube inner-diameter used in the experiments was 0.75 mm. The total time between in-signal to measuring signal was defined as the sum of the time between in-signal from ORBIT to pump execution in ÄKTA, average residence time in the outlet tube, average residence time in conductivity meter and response time of the software and the conductivity meter.

Lag time from in-signal to execution in ORBIT, β_{pump}, was estimated to approximately 1.08 s, estimated by measuring the time from in-signal from ORBIT, given by the timestamp in the script, to measured pressure response in UNICORN, indicating that the pump started working. The response time of the software in UNICORN was estimated by conducting a series of experiments at flow rates between 10-50 ml/min, thus reducing residence time effects in the conductive meter. The response time between simulation and measurement in UNICORN, β_{lag} was found to be approximately 2.50 s at higher flowrates.

It was seen when conducting experiments that the time difference increased when comparing simulations and experimental values at lower flowrates. The measuring time was found to be inverse proportional to the flowrate and was assumed to be caused by increased residence times in the conductive meter. Rather than conducting a larger series of experiments and fitting a function for measuring time as a function of flowrate, an approximation where the time-lag in the meter, β_{cond}, was estimated as being equivalent to the residence time in ¼ of the total volume, 199 μl, of the conductive meter, was found to have a decent fit between both higher and lower flowrates with a standard error of approximately 2.30 % for one of the data sets. (Healthcare, 2015) More studies regarding measuring technology and a larger amount of experiments needs to be conducted to ensure more exact results over a wider range of flowrates and is beyond the scope of this thesis.

3.3.2 Conductivity Experiments

The experimental set-up for the measurements was carried out by essentially by-passing the whole ÄKTA-system, and coupling the T-mixer directly to the conductivity meter without flow restrictors, thus eliminating all obstacles which could affect the measuring signal other than the dispersion in the tubes. Mixing in the tubing was investigated for different flows, tube lengths and mixing ratios using step response experiments.

The solutions that were used in the experiments were 0.10 M and 1 M NaCl solution and deionised water. Measurements, 200 mm from the mixing point was found to give reliable results, while measuring closer to the mixing point proved difficult to extract useful and reliable data. Several experiments were conducted at mixing ratios of 5, 10, 15, 20, 50 and 100%, for 3 different tube lengths, 642, 400, 200 mm at different flowrates between 1-50 ml/min, and compared with simulations to investigate the homogeneity of the solution at the outlet of the tube.

To compare results between asymmetric and symmetric mixing in the T-mixer, inlets where mixed perpendicular relative to each other, and symmetric flow as used in the CFD simulations, experiments at flowrates of 1, 2, 4 and 10 ml/min at a mixing ratio of 50% was compared with the symmetric configuration.

To compare with numerical simulations, the conductivity was converted to concentration of Total Dissolved Solids(TDS) by an estimated conversion factor and divided by the molar weight of NaCl to convert the conductivity to concentration. Since TDS gives the total amount of dissolved ionic species it was important to prevent CO_2 from dissolving into the water which would have increased the concentration of dissolved ions in the solution. The prepared 1 M NaCl was measured to have pH of 7.5 before each experiment and para-film was put at the top of each bottle to prevent build-up of carbonic acid and hydrogen carbonate in the solution.

Concentration measurements could only be reliably and accurately estimated from conductivity at lower concentrations of NaCl. This was assumed to be caused by the non-linear relation between conductivity and concentration, since at higher concentration, the measured concentration was always lower compared with the simulations. All experimental run times and conductivity data were logged and stored in CSV files and post-processed in MATLAB using **xlsread**.

3.3.3 Mathematical modelling- Step response experiments

For the experimental analysis a macroscopic lumped parameter dispersion model was used for comparison with the step response experiments run in ÄKTA. A time-dependent Dirichlét boundary condition was used to model the inflow of solute to the domain. The problem was

solved analytically, using Laplace transformation and compared with experiments and a discrete model for different tube-lengths, flowrates and mixing ratios. The discrete model was based on a finite volume method (FVM) approximation scheme, using the Method-of-Lines (MOL). The benefit of using analytic computations whenever possible was simplicity over having to rely on discrete models only and an increased control over the numerical simulations when comparing parameter sensitivity for the different models.

3.3.3.1 Analytic model

The analytic model treats the tube as a semi-infinite domain, assuming no boundary effects from the conductive measuring device, only requiring that the solution is bounded for large x.

$$\begin{cases} \partial_t u - {}_{D_{ax}}\partial_x^2 u + \bar{v}\partial_x u = 0\,, x \geq 0 & t > 0 \\ u(0,t) = f(t) & t > 0 \\ u(x,0) = 0 & x \geq 0 \end{cases} \tag{27}$$

$$D_{ax} = \frac{\bar{v} * L_c}{Pe} \tag{28}$$

For a given function $f(t)$ we can show, that any solution u can be written in convolution form, provided that the integral exists.

$$u(x,t) = \int_o^t k(x, t-\tau) f(\tau) d\tau \tag{29}$$

where $k(x,t) = \frac{x}{\sqrt{4D_{ax}t^3\pi}} e^{-\frac{(x-\bar{v}t)^2}{4D_{ax}t}} \theta(t)$, corresponds to the system pulse response.

The normalised pulse response is given by $E(t)_{x=L} = \frac{k(L,t)}{\int_0^\infty k(L,t)dt}$ for a given tube length and we can now calculate the moments of the function $E(t)_{x=L}$ defined by, normalised pulse response, μ_0, mean average residence time, μ_1, variance, μ_2 and variance from mean average residence time, σ^2.

$$\mu_0 = E(t)_{x=L} \tag{30}$$

$$\mu_1 = \bar{t} = \int_0^\infty t E(t)_{x=L} dt = \frac{L}{\bar{v}} \tag{31}$$

$$\mu_2 = \int_0^\infty t^2 E(t)_{x=L} dt \tag{32}$$

$$\sigma^2 = \int_0^\infty (t^2 - \bar{t}^2) E(t)_{x=L} dt = \mu_2 - \bar{t}^2 \tag{33}$$

The integration was done numerically using the trapezoidal rule, **trapz**, in MATLAB with a step length of $10^{-5}\ s$.

Given that the system initially is at rest, we look for causal solution for a given perturbation at the boundary. Assuming homogeneity and neglecting radial transport of solute, diameter of the tube is much smaller compared with the tube length, $D_{tube} \ll L_{tube}$, the mixing of two miscible liquid streams corresponds to a "switch-on" of a continuous source at a given time at the boundary, where the concentration was given by the mixing ratio of the two streams.

The solution for $f(t) = \alpha * \theta(t-\beta)$ can be seen below, where $\theta(t-\beta)$ is the Heaviside step function, α is the mixing ratio between the inlet streams and $erfc$ is the complementary error function. The time of the step response β, is defined as the sum of the times set for the step response in the SPYDER script (β_{step}), the lag time from the computer software and measuring signal (β_{lag}), residence time in conductive meter ($\beta_{cond} = \frac{V_{cond}}{4Q}$) and pump-execution time (β_{pump}), corresponding to the actual step time of $\beta = \beta_{step} + \beta_{lag} + \beta_{pump} + \beta_{cond}$. To calculate the dispersion coefficient, D_{ax} given by eqn. (28), the characteristic velocity was set to the average velocity, $\bar{v} = \frac{Q}{A} = \frac{4Q}{\pi {D_{tube}}^2}$ and $L_c = D_{tube} = 0.75\ mm$.

The solution to an ideal step response of the system is

$$u(x,t) = \begin{cases} 0, t \leq \beta \\ \frac{1}{2}\alpha\left(\left(erfc\left(\frac{x-\bar{v}(t-\beta)}{\sqrt{4D_{ax}(t-\beta)}}\right)\right) + e^{\frac{\bar{v}}{D_{ax}}x}\left(erfc\left(\frac{x+\bar{v}(t-\beta)}{\sqrt{4D_{ax}(t-\beta)}}\right)\right)\right), t > \beta \end{cases} \quad (34)$$

With a small percentage in error from the correct solution, the second term can be neglected. (Warfvinge, 2015) which gives

$$u(x,t) = \begin{cases} 0\ t \leq \beta \\ \frac{1}{2}\alpha\left(erfc\left(\frac{x-\bar{v}(t-\beta)}{\sqrt{4D_{ax}(t-\beta)}}\right)\right) t > \beta \end{cases} \quad (35)$$

The benefit of using this approximation is that we know for $(t-\beta) = \frac{L}{\bar{v}}$, that $u = \frac{1}{2}\alpha$, which suited the experimental analysis when estimating fluid flow segregation. Using the linearity of eqn. (27) and the super-position-principle, the solution was extended to model a "switch-off, of the continuous source and step-down, at time γ, correlated in time in a similar fashion as β, which was more suitable when comparing simulations and experiments, with the following solution.

$$u(x,t) = \begin{cases} 0\ \ t \leq \beta \\ \frac{1}{2}\alpha\left(erfc\left(\frac{x-\bar{v}(t-\beta)}{\sqrt{4D_{ax}(t-\beta)}}\right)\right) \beta < t \leq \gamma \\ \frac{1}{2}\alpha\left(erfc\left(\frac{x-\bar{v}(t-\beta)}{\sqrt{4D_{ax}(t-\beta)}}\right) - erfc\left(\frac{x-\bar{v}(t-\gamma)}{\sqrt{4D_{ax}(t-\gamma)}}\right)\right)\ t > \gamma \end{cases} \quad (36)$$

3.3.3.2 Discrete model

The mathematical model that was used for the discrete model can be seen below.

$$\begin{cases} \partial_t u - {}_{D_{ax}}\partial_x^2 u + \bar{v}\partial_x u = 0 & x \in [0,L], 0\ t > 0 \\ u(0,t) = f(t) & t > 0 \\ \partial_x u(L,t) = 0 & t > 0 \\ u(x,0) = 0 & x \in [0,L] \end{cases} \quad (37)$$

The discrete model was based on a Finite-Volume-Method discretization scheme using the Method-of-Lines (MOL). (Sellberg, 2018) The tube of length L, was discretized using 100 grid

points with a 2 points-backward upwind approximation for the convection term and a 3 points central approximation for the Dispersion term. The boundary conditions for the model was inhomogenous Dirichlét for the inlet and homogenous van Neumann at the outlet of the tube. The discrete model was solved using an implicit ODE solver, *ode15s*, in MATLAB.

3.3.3.3 Statistical analysis of model parameter

A single model parameter, $P = 1$, the dispersion Peclét number, Pe, was calibrated manually, using a parametric sweep and compared with experimental data. The sum of squares error, Q between the normalised model, $y^M = \frac{y_M}{\alpha}$, and experimental data points, $y^D = \frac{y_D}{\alpha}$, for N data points was defined as

$$Q = \sum_{i=1}^{N} \left({y^D}_i - {y^M}_i \right)^2 = \sum_{i=1}^{n} {r_i}^2 = \boldsymbol{R^T R} \tag{38}$$

$$\boldsymbol{R = y^D - y^M} \tag{39}$$

The standard error, ε, for the model parameter p, were then estimated for different Pe given by the parametric sweep.

$$\frac{dQ}{dp} \approx \frac{\Delta Q}{\Delta p} = \frac{Q_1 - Q_2}{p_1 - p_2} = \boldsymbol{J} \tag{40}$$

$$\boldsymbol{X = (J^T J)^{-1}} \tag{41}$$

$$\varepsilon = \sqrt{\boldsymbol{\sigma^2 (J^T J)^{-1}}} \tag{42}$$

where $\sigma^2 = \frac{Q}{N-P}$ was the co-variance value for the model parameter.

3.3.4 Experimental hypothesis Conductivity Measurements

The link between the COMSOL world that was created and the experimental measurements, was the estimation of mixing efficiencies and visual investigation of the streamlines describing the flow configuration, at different flowrates. When conducting the measurements, an experimental hypothesis was developed.

1. The flow regime in the tubes and in the T-mixer, at lower flowrates, is laminar.
2. No mixing occurs, since there is no transversal flow in the tubes.
3. Solute only travels along streamlines. Thus, at stratified flow and differences in ratio between inlet streams, the relative difference in momentum will push the opposing fluid to the outer regions of the outlet tube, which has lower velocity due to the laminarity.
4. The analytic model assumes and expects complete homogeneity, for a given step response. Any deviation from the average residence time given by the analytic model shows that the solute on average spends a longer time in the tube that was expected and thus indicates that the fluid is not mixed at the mixing point.

3.3.5 Pump experiments

The aim of this study was to investigate the cause behind the fluctuation that occurred during the measurement of the concentration/electrical conductivity, also to observe the size of those fluctuations. An important thing to consider is that the pump study was conducted without bypassing the ÄKTA-system, keeping flow-restrictors and switching valves at a default setting,

as explained in the previous section when conducting the conductivity experiments. The only thing by-passed when investigation effects of the pump fluctuations was the column. A sketch design of the mechanism for the reciprocal pump used in the ÄKTA system can be seen in figure 18. (Healthcare, 2005)

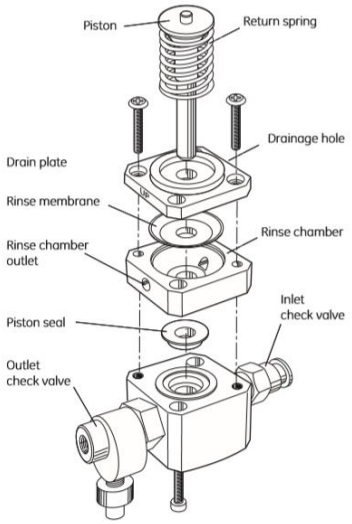

Figure 18: Reciprocal pump

The pumps in the ÄKTA system works the following way. When starting the system, the water pump, pump A, starts alone until the buffer pump starts. The interesting thing here is that when the buffer pump, pump B, is on, the total flow is shared between the water and the buffer flows (depending on the buffer gradient that was sent into the system). To investigate how the fluctuations occurs, a series of runs should be done to test out each pump alone with variety of flow rates that ranges between 1 ml/min to 5 ml/min. After that a series of run of both pumps running together is done with the same flow rates mentioned above.

3.4 Visual experiments - Ethanol and Water

With water and ethanol, the issue of conducting experiments came with the limited possibility to measure the mixing process as done in the conductivity measurements, thus forcing the use of visual experiments. Visual experiments were also conducted for water-NaCl solutions. The aim of the experimental investigation was to gain visual indication of how well mixed the solutions were within the tube. The experiments were conducted by adding two inert indicators, blue dextran and sodium fluorescein, one for each solution. Transparent tubes with 1 mm in diameter were used to see both fluids after the mixing point. The trade-off using the transparent tubes, was the increased mixing length compared with the 0.75 mm tubes usually used when running processes in ÄKTA. The solute, would thus take a longer time to mix in the radial direction, due to the increase in tube diameter, making it difficult to directly apply the experimental results on the 0.75 mm tubes. The color of blue dextran is blue while sodium fluorescein dyes the solution with a yellow color. An indicator of mixing within the tube was if both solution turned green colored in the outlet tube. The outlet was sent directly to waste without passing any flow restrictors or other process equipment.

3.4.1 Preparation of solutions

The solutions used for the visual experiments were prepared by adding blue dextran to a 250-ml deionized water to the point to where the concentration is around 2 to 3 g/l. A less concentrated solution will give false results as in the blue color is very light and faded to be seen. Add

sodium fluorescein to 250 ml of 1 M NaCl solution and 250 ml of 70 % ethanol, the concentration of the indicator in the solution should be around 1 g/l. An important factor to keep in mind when making the solutions is to make sure to mix the solutions very well to get an even distribution of the indicator in the entire solution.

The experimental runs that were made during the investigation for both 1 M NaCl and 70 % ethanol can be seen in the table 1 below.

Table 1: Flowrates and mix ratios used in visual experiments

Flow rate [ml/min]	Mix-ratio [%]
1	10 20 30 50
2	10 20 50
10	10 50

3.4.2 The dynamic mixer experiments

This study utilized a dynamic mixer, which has a magnetic stirrer that mixes the solutions that enters the mixer. The reason behind using this type of mixers is to present an alternate solution so that the fluids used in the system can get mixed without the need of setting very high flow rates that may causes damage to chromatography columns due to the high pressure drop, caused when using high flow rates.

4 Results

The results presented, is divided into two parts. The first part consists of the results from the CFD-analysis. The second part of the results consists of the experimental pump study and flowrate experiments followed by the conductivity experiments and finally the visual experiments, using the T-mixer and the dynamic mixer.

4.1 CFD Analysis

4.1.1 W/E -W/W

When comparing contour plots of the cross-sectional velocity profile at the outlet, the point of v_{max} had been moved from the centre of the mixing channel, which can be seen in figure 19 and 20, due to the viscous boundary layer between the fluids in the W/E-system. For W/E, the higher density of the water stream meant that a larger volume of the mixing channel contained water as the streams flowed through the mixing channel. The flow configuration appeared to be more asymmetric when comparing the streamlines, due to the difference in density between the two inlets, visible in figure 21 for W/W at $Re = 212$ and figure 22 for W/E, $Re = 86$.

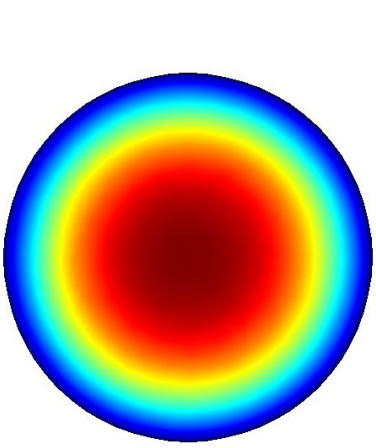

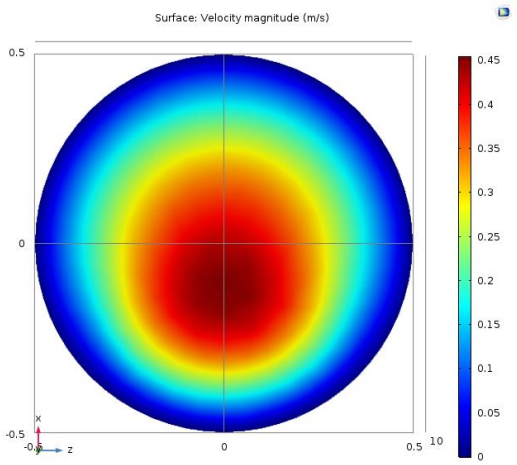

Figure 19: W/W Re 212 Velocity Magnitude *Figure 20: W/E Re 86 Velocity Magnitude*

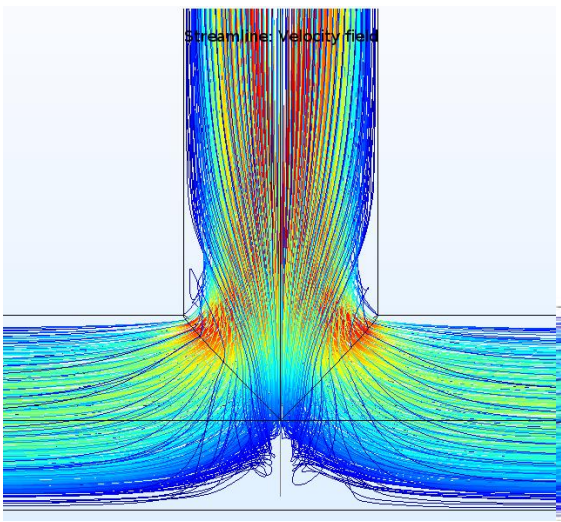

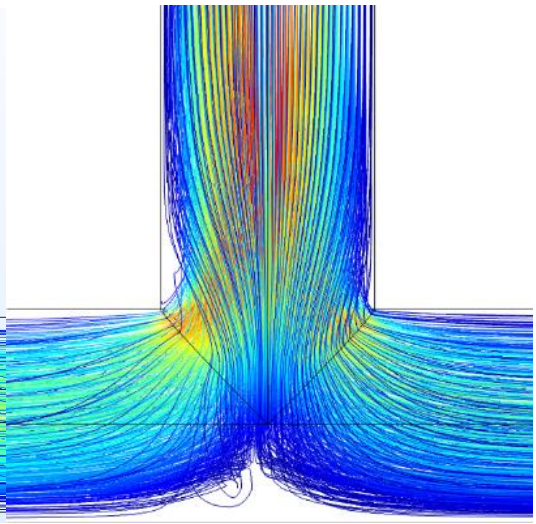

Figure 21: W/W Re 212 *Figure 22: W/E Re 86*

For W/W, a pair of Dean vortices formed at the confluence of the mixing point but the flow was otherwise symmetric with a well-defined symmetry line between the inlets, seen for the streamlines depicted in figure 23 and 24 and for the concentration field in figure 25 and 26 for Re values of 1698 and 1273, respectively. Increasing Re from 40 to 2200 for W/W, showed no significant decrease in mixing efficiency, σ_1, as a function of Re. σ_1 decreased from 37 to 32 % between Re 42 to 1273, which can be seen in table 2, where σ_1 and δ_m are listed for different Re. From Re 1273 to 2200, σ_1 was unchanged. For W/E, both σ_1 and δ_m changed at a similar rate which can be seen in table 2. The slightly lower δ_m for the W/E-system at Re 340 compared with 554 should therefore be compared with the equivalent value for σ_1 which showed no change in mixing. At approximately Re 660, both σ_1 and δ_m showed respectively, a significant decrease and increase, compared with lower Re for the W/E-system. This implies that the flow configuration becomes an asymmetric at a critical Reynolds value of approximately 660, although this was not immediately visible when examining the streamlines comparing Re 660 with Re 554, which can be seen in figure 27 and 28.

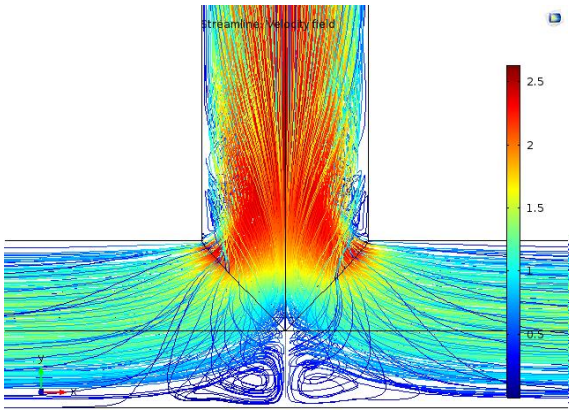

Figure 23: W/W Re 1698

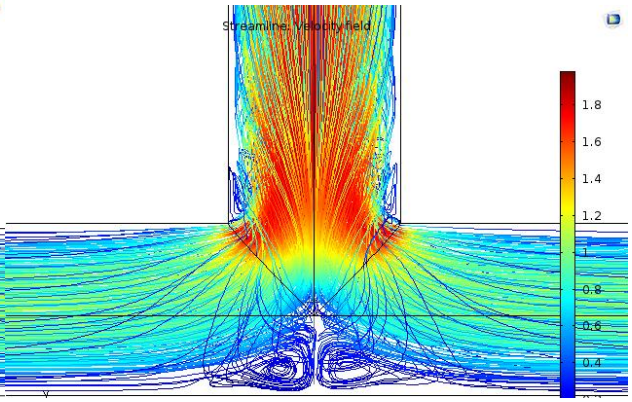

Figure 24: W/W Re 1273

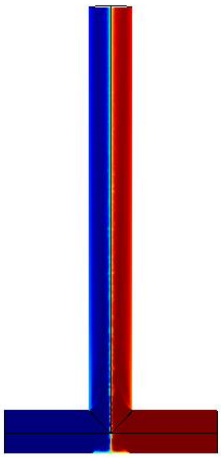

Figure 25: W/W Concentration Re 1698

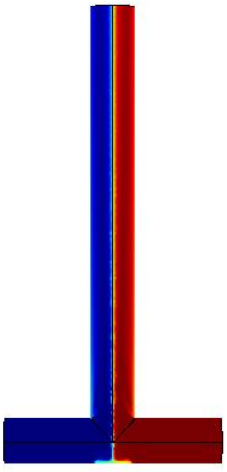

Figure 26: W/W Concentration Re 1273

Table 2:Mix efficiencies for W/E and W/W system showing increased efficiency for W/E system at 661 Re compared with no significant increase for W/W regardless of Re.

Inlet volumetric flowrate[ml/min]	$Re_{mixing\ channel}, W/E$	σ_1[%]	δ_m [%]	$Re_{mixing\ channel}, W/W$	σ_1[%]
1	18	38	28	42	37
5	86	36	30	212	35
10	172	34	34	424	34
20	340	33	34	848	33
30	554	33	32	1273	32
40	661	0	100	1698	32
50	826	0	100	2122	32

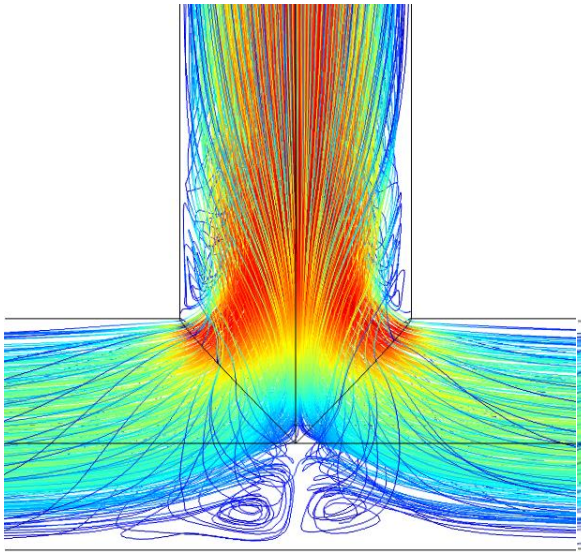

Figure 27: W/E Re 661

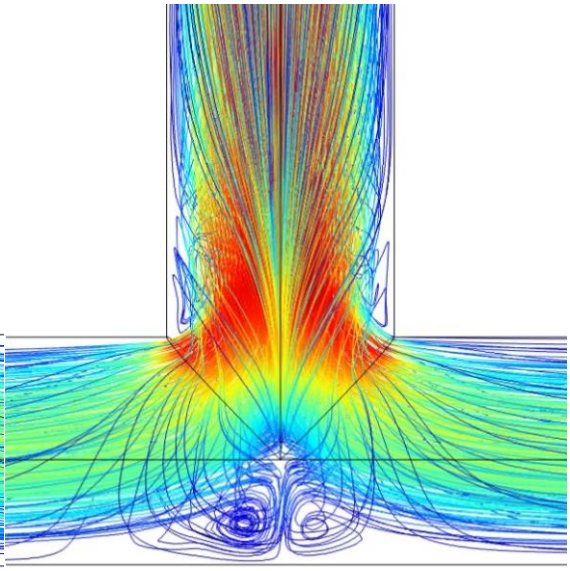

Figure 28: W/E Re 554

When examining the scalar fields for the effective viscosity, effective density and mass fraction of ethanol, it showed a complete break-up of the viscous boundary layer and the well-defined region between the fluids at Re 660, compared with Re 554, which can be seen in figure 29 and 30. It was therefore assumed that the relative difference in density between the inlet streams, were the major factor for increasing the mixing efficiency due to the induced asymmetric flow pattern, at a critical Reynolds value.

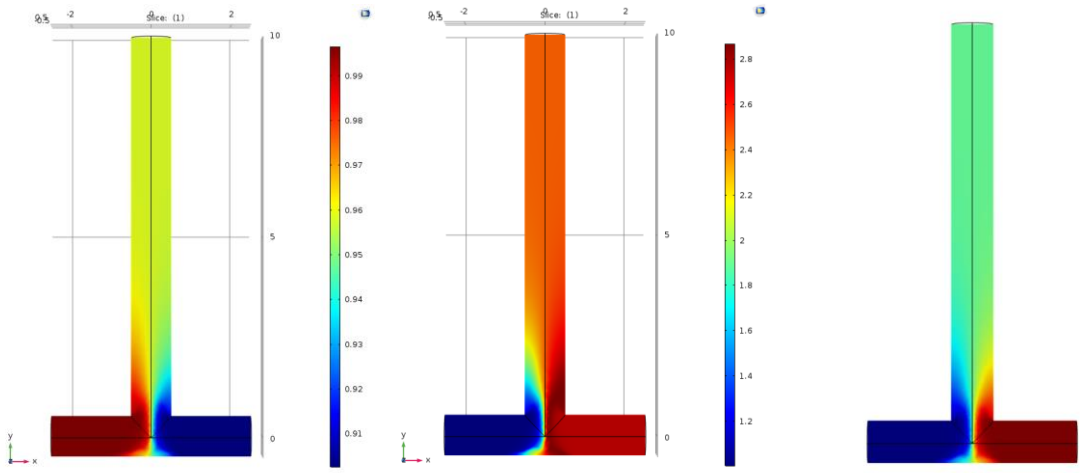

Figure 29: Effective viscosity, Effective viscosity, Mass fraction ethanol, Re 661

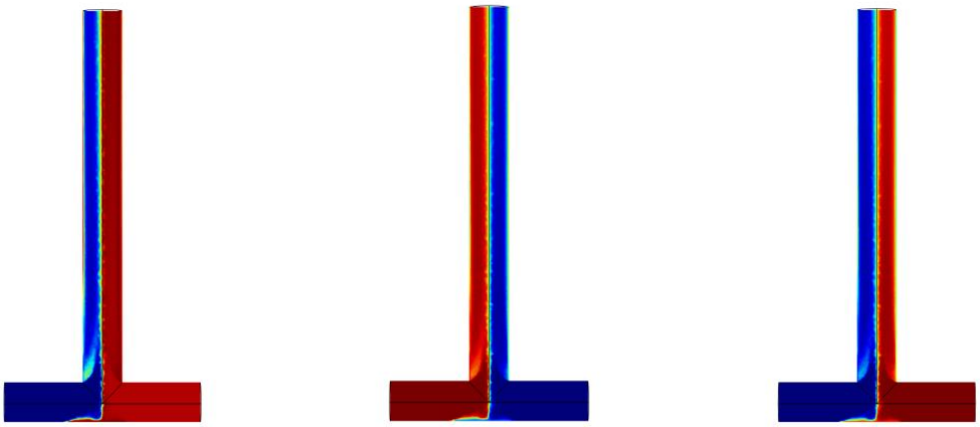

Figure 30: Effective viscosity, Effective density, Mass fraction ethanol, Re 554

When comparing mesh and discretization, it was found that there was no mesh dependence when calculating the mixing efficiency and that the 1st order discretization always gave a lower σ_1 value compared with using a 2nd order element both for W/E- and W/W-system, 11% for 1st and 17% for 2nd at Re 340 for the W/E-system. When comparing the mixing efficiency at high Re for the W/W-system it showed similar level of overestimating the diffusion for lower discretization, but it did not show the sharp shift at a Critical Reynolds value as for the W/E system. The computation time when switching to a coarser mesh was significantly reduced, thus it was found that using higher level discretization and coarser mesh was more accurate and robust for the simulations due to failed simulations at finer mesh for $Re > 660$ for W/E. Increased mesh refinement to further increase the resolution of the viscous boundary layer showed failure of convergence for high Re for W/E, most likely caused by increasing number of singularities around the joint elements of the geometry. At Re below 660 the resolution of the viscous boundary layer and density showed a significant increase in the resolution when comparing coarser and finer mesh. Due to the relatively high Reynolds number investigated, corner refinement and boundary layer meshing was kept as default options to get accurate estimations closer to the walls of the geometry.

As previously mentioned, the asymmetry of the two fluid streams at higher Re seems to be the causing factor for increased mixing, thus there is potential to use the T-mixer as an engulfment mixer, at higher flowrates and when the dilution level needed is asymmetric in comparison to solute stream. However, at perfect symmetry or lower flowrates the flow is completely segregated and the mixing in the cross-section occurs by diffusion only which is assumed to be mainly caused by the geometry of the mixing channel of the T-mixer. Changing the mixing channel diameter could potentially solve these issues and cause engulfment and better mixing at lower Reynolds. The diffusivities in the simulations were of the magnitude 10^{-9} and when discussing diffusive mixing of larger molecules such as proteins, with lower diffusivities, this effectively leads to even lower rates of diffusion when studying the mixing process in the tubes.

The accuracy of the NS flow field simulations needs also to be considered, as no elements better than 1st order element for the velocity field successfully converged. This was mainly assumed to be due to the by default stabilisation methods used for the NS-equations in COMSOL MULTIPHYSICS. Estimation of the size of the Dean vortices forming for different Reynolds could potentially be used as measure for adaptive mesh refinement and higher resolution around the cylindrical walls, but as previously mentioned considering the stability of the advection diffusion equation and increased number of singularities around the joint elements of the geometry, this could prove troublesome. Thus, further investigation of the stabilisation of the 2nd order element in NS needs to be investigated, to potentially get more accurate simulations for the T-mixer.

4.1.2 Static mixer configurations

The calculated mixing efficiencies, σ_1, showed that the stationary mixer with baffles had the highest estimated mixing efficiency of 1.5 % compared with advection model, 5.1% and serpentine model, 10.2 %. The stream line profiles showed that the flow configuration in the stationary mixer with baffles, was more 3-D, due to the cylindrical geometry, compared with the advection model. The streamlines of the different mixing configurations are depicted in figure 31 below.

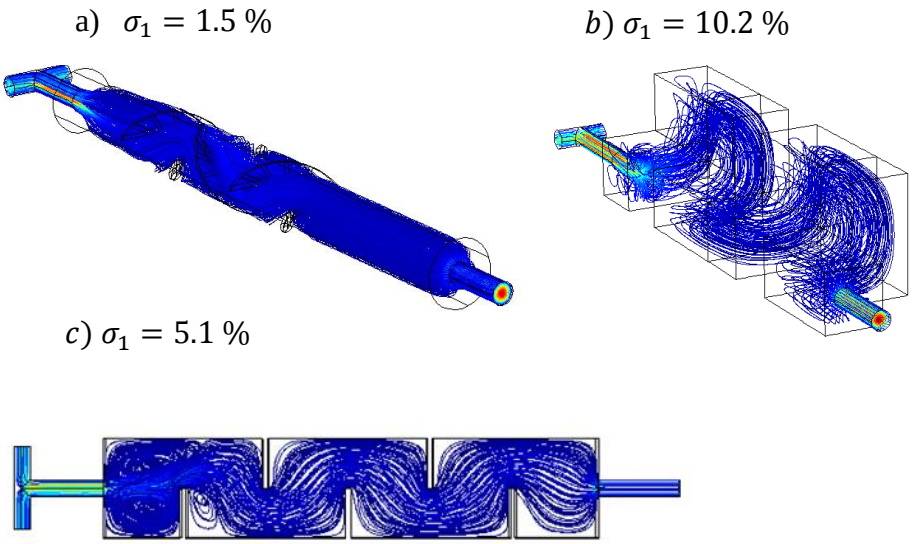

Figure 31: Streamlines and estimated mixing efficiencies, σ_1, for different stationary mixer configurations, a) helical baffle shaped mixer, b) serpentine mixer and c) advection model.

Slice plots of the concentration profile also show the increasing homogeneity in the concentration field for the three models which can be seen in figure 32. The baffle mixer showed a higher degree of continuous break-up of the material structure of the fluid, compared with the advection and serpentine model. The concentration field in the serpentine model exhibited similar rotating distortions as the baffle mixer but the helical shaped baffles seemed to be more effective in creating a high degree of distortion to the diffusive layers in the fluid when comparing the calculated mixing efficiencies.

a) b) c)

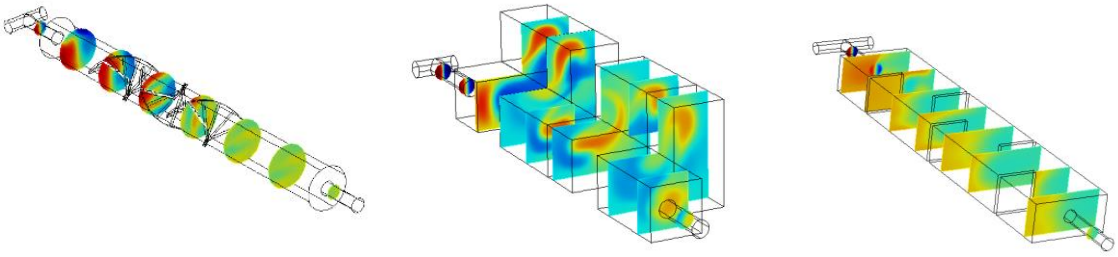

Figure 32: Stationary Concentration between two inlet streams in three different stationary mixer configurations. a) helical baffle shaped mixer, b) serpentine mixer and c) advection model.

When examining slice plots of the concentration profile for the advection model, the concentration field was relatively unchanged after the first section, indicating that the mixer is most efficient in the beginning, assumed to be caused mostly due to the vortex at the inlet of the mixing chamber, indicating a high degree of dispersion as the solute enters the mixer. Adding more sections, would therefore not likely increase the mixing efficiency. In comparison, by increasing the flow rate to the point of vortex formation in each advection cycle, may increase the mixing efficiency substantially, due to the increased folding of fluid elements. Other parameters that potentially could affect the mixing efficiency, is placement of the section walls to further increase the 2D folding effect of the transverse flows in the channel. Due to the high numerical sensitivity of the continuum models, there were convergence issues when increasing the flowrate and coupling it to the advection diffusion equation.

As the flow in the baffle mixer was continuously mapped in the same direction compared with the advection model and the serpentine mixer, it therefore seems that the increased mixing efficiency was created by simultaneously enhancing the diffusive mixing, through increased distortion of the material layers, by advection. While the other models relied only on pure advection to mix the fluid, the baffle mixer works with advection as a way of creating distortion and convolute the concentration field, while the mixing in the end, occurs by diffusion. Optimisation of flowrates, positioning of walls and channel geometry was not done to increase the mixing in the advection and serpentine model and it seems to be more potential in increasing the advective mixing effect from the transverse flows in the mixing channel, than was successfully achieved. For lower flowrates, the combination of advection and diffusion used in the helical baffle mixer seems to be the best option for achieving a high level of controlled mixing without obstructing or affecting the overall running parameters of the process.

When it came to the simulation method, the segregated method of solving NS on a coarse mesh and the stationary transport equation for the solute on a finer mesh, only worked successfully

on the stationary mixer with baffles. While transient simulations of the advection-diffusion equations required very long computation times on fine meshed grids and occasionally exhibited unphysical oscillations on coarser meshes, the segregated method could usually be implemented without any issues regarding convergence. The stationary advection-diffusion equation however, seemed stiffer and more sensitive to the choice of boundary conditions, discretization and choice of mesh size and distribution, compared with the transient simulations and all simulations needed coupled simultaneous solving NS and advection diffusion on the same mesh structure.

The simulations of the helical shaped mixer, were sensitive to the choice of mesh, discretization and diffusivity coefficient, which changed the estimated mixing efficiency from between 1.5-4%. Some simulations also showed oscillations in the concentration field at finer mesh structures, assumed to be caused by over-interpolation, of the concentration gradients around the helical baffles. This needs to be considered when discussing accuracy of the simulations and when comparing the different mixing configurations, based on mixing efficiency.

Below, slice plots of the stationary concentration field for different cross-sections in the static mixer with helical shaped baffles (a-h), advection (i-m) and serpentine model (n-p) can be seen in figure 33. The figures show that the highest degree of distortion was caused by the stationary mixer with helical shaped baffles, although the serpentine model showed similar rotating serpentine like distortion of the concentration field, without having the issues with the dispersion effects from the initial vortex as in the advection model.

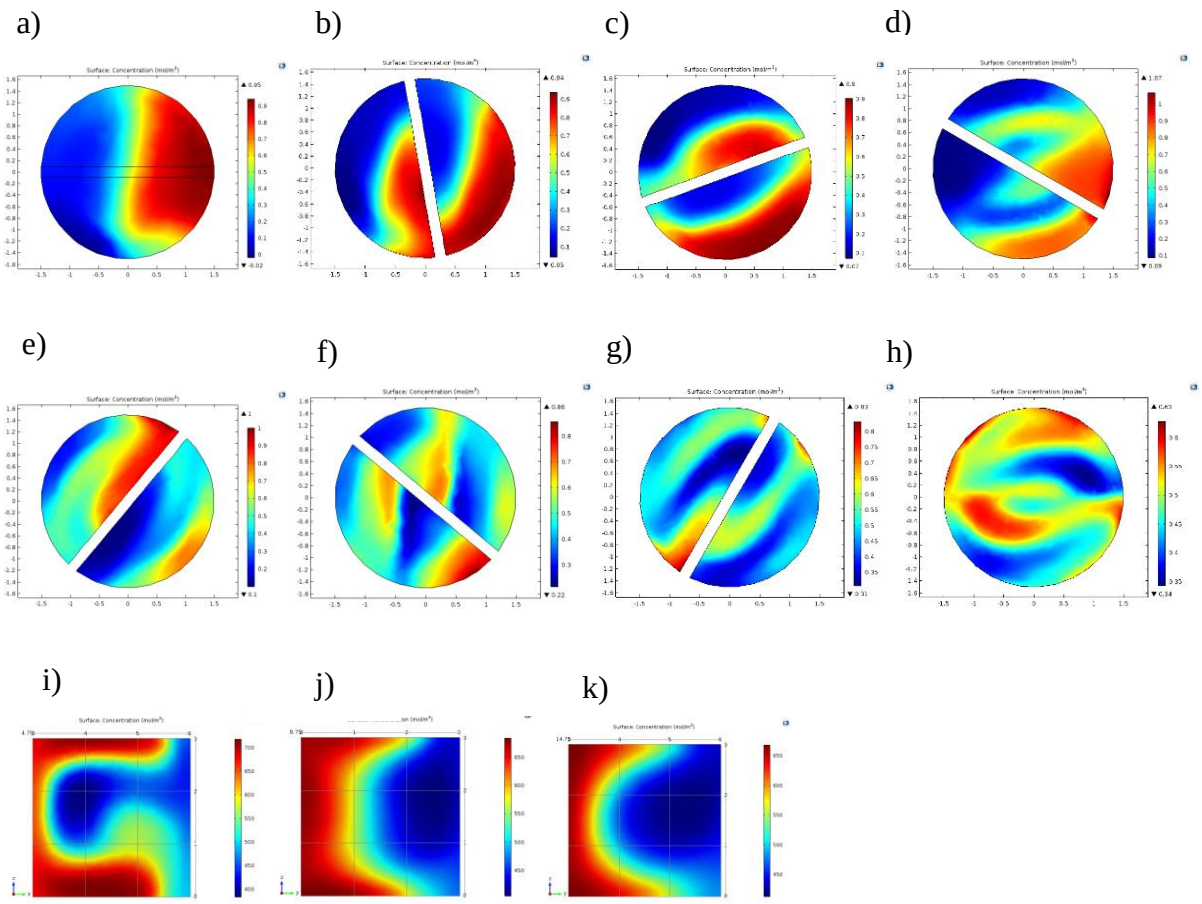

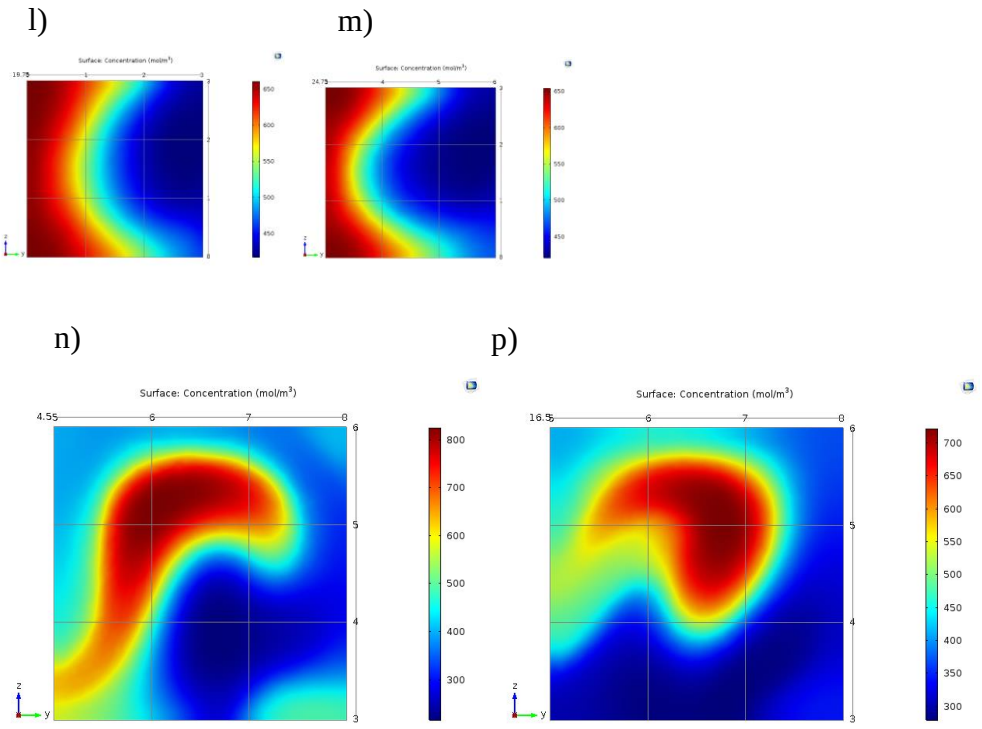

Figure 33: Slice plots of stationary mixer with baffles (a-h), Advection model (i-m) and Serpentine Model(n-p)

4.1.3 Stirred mixer

Attempts with continuum models to model the mass distribution of two mixing streams in the stirred mixer, were prone to numerical instabilities and oscillatory behaviour between positive and negative infinities in time. This was assumed to be due to the sensitivity of the continuity condition between the stationary flow field and the scalar concentration field which introduced the numerical instabilities in the solver sequence. Mesh refinement between the continuous phase between the stationary parts and the rotating domain could potentially increase the resolution and therefore impose the continuity condition on the advection diffusion equation more effectively. This potentially could stabilise the oscillatory behaviour of the concentration field, but as fluid particles in practice, only travels along the streamlines by advection, particle tracing could potentially be a more convenient method to use. When examining the streamlines from the Frozen Rotor solution, both the large and smaller mixer, showed a rotating vortex above the agitator as the fluid entered the mixer which can be seen in figure 34. The velocity then increased closer to the stationary walls, as it comes closer to the rotating agitator, indicating high stretching of the fluid elements before it gets caught in the faster moving outer regions of the geometry. For the larger mixer, it is therefore assumed that a longer retention time of the fluid is spent at the top of the geometry. The 2-D velocity vector field also showed that the angular velocity in the spiralling vortex was close to zero in the middle, which meant that solute caught in the middle of the vortex spends a longer retention time above the rotating agitator. Due to the flat surface, there potentially is a risk of build- up and accumulation of mass atop the surface. When examining the vector velocity field above the rotating agitator, there seemed to be no difference between the flat surface and the ball shaped geometry which can be seen in figure 35. It should be noted that the curved shape of the ÄKTA agitators are more rounded compared to the spherical ball geometry used in the simulations but the simulations showed no apparent

difference of the vortex flow, for the different geometries, so there is likely to be no effect on the flow field from this part of the geometry.

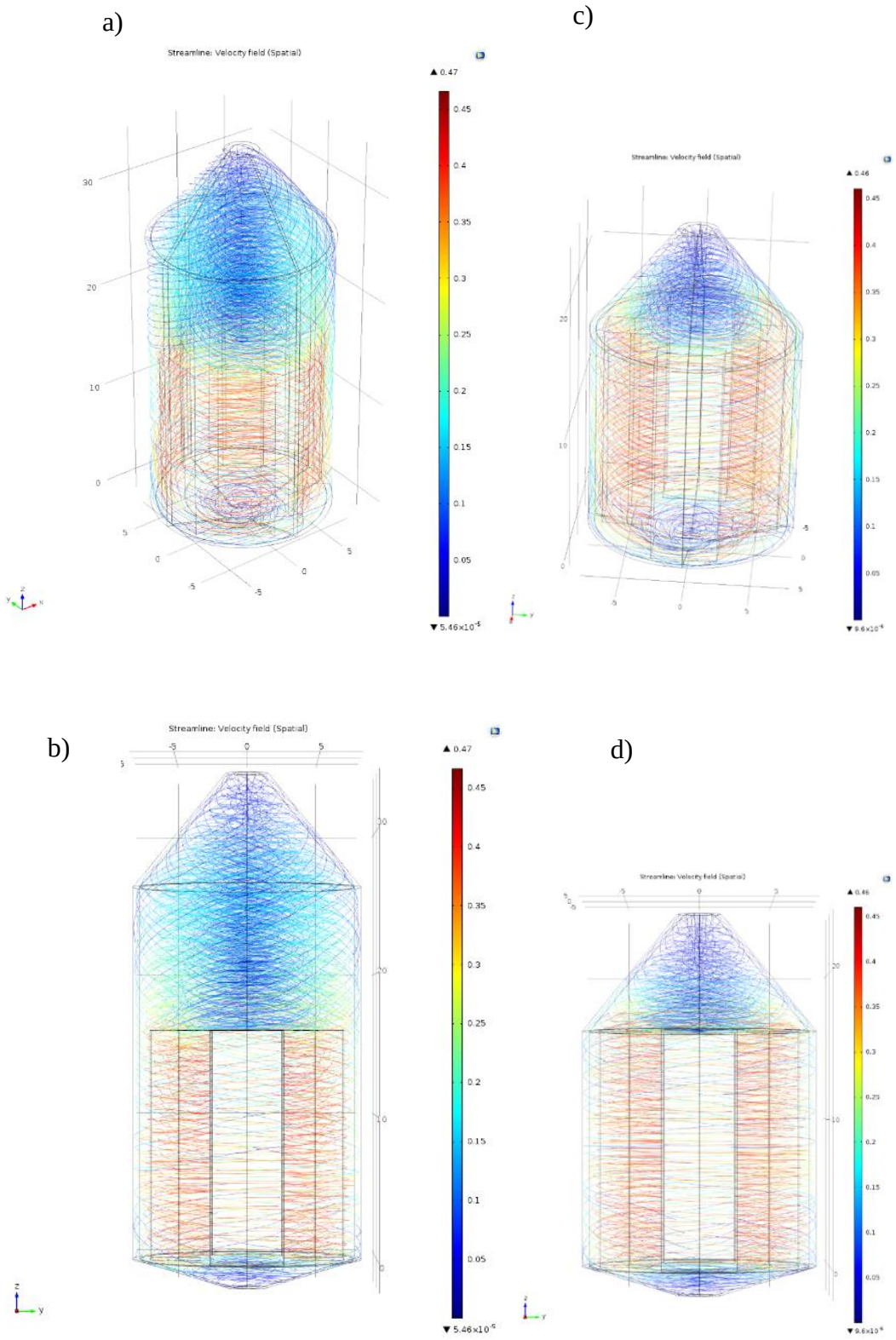

Figure 34: Streamlines from Frozen Rotor Solution in large mixer(a-b) and small mixer(c-d) with flat surface on top of rotating agitator, N=10[1/s].

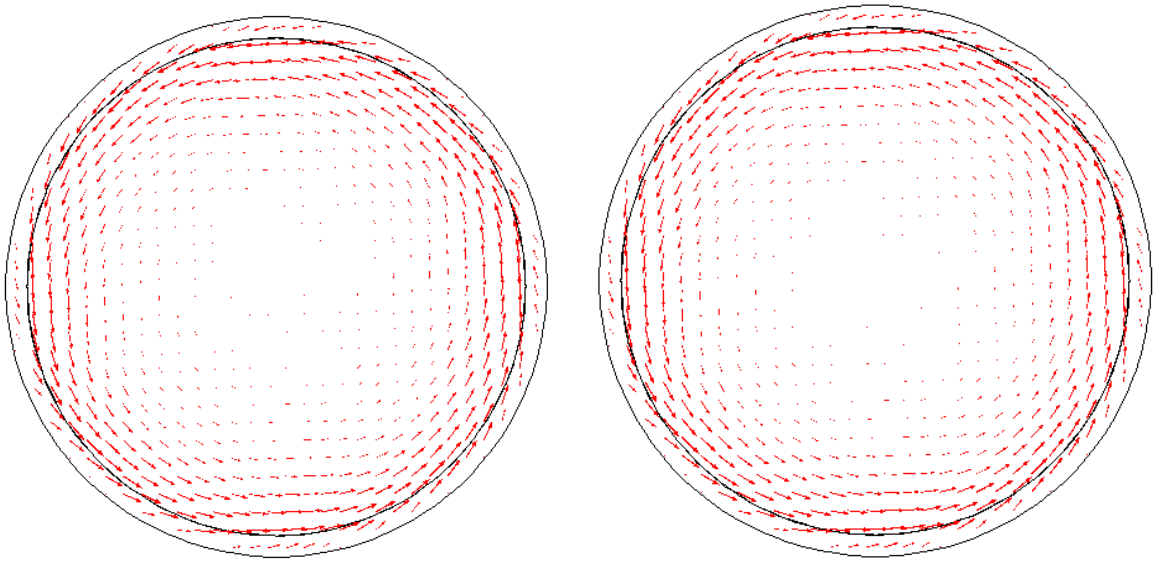

Figure 35: Arrow surface depicting velocity field above flat surface (left) vs ball (right) showing no apparent differences in the velocity field.

Surface plots of the shear-stress rate also showed low resolution of the viscous boundary layer between the rotating agitator and the stationary walls, which further indicated that mesh refinement of the continuous phase between the stationary and rotating parts are needed. This means in practice that the simulations become less accurate, closer to the stationary wall and rotating agitator and at the continuous phase between the stationary and rotating domain, located 7.50 mm from the centre of the mixer. 2-D plots of the shear rate in the fluid, after the agitator have been rotating at top speed for 0.50 seconds in figure 36, show the viscous boundary layer in the middle and at the bottom of the agitator. The Frozen Rotor simulation gave a comparatively lower resolution and an angular distribution of the shear rate in the viscous boundary layer, compared with after the rotor had been rotating for 0.50 seconds. The transient simulations reached a steady state after approximately 0.10 s in the simulations, starting from the Frozen Rotor solution, which could potentially be lowered with shorter output time steps in the transient simulations. Using the Frozen Rotor simulation as initial condition for transient simulations, seems therefore to be more reliable for studying steady state behaviour of the flow field when conducting boundary layer analysis.

Although the resolution in the simulations were low due to the coarse mesh size, the increased shear rate between the agitator and close to the walls indicates sharp gradients in the velocity field, which potentially could damage and harm sensitive molecules in the mixer. Also around the tips of the blades that are close to the wall, the shear rate was higher, compared with the blades further away from the walls. The largest shear rate in the simulations was expected around the bottom of mixer the tip of the blades close-in-contact with the conical walls, $\sim 3000\ s^{-1}$ and around the sharp corners between the cylinder and the connected blades, indicating that the sharpest gradients in the flow field is found around contact areas or where there are very narrow gaps between the rotating and stationary geometry. Potential methods to remedy this could be blade refinement and corner smoothing around the sharp edges and having the blades not rotating to close to the walls to lower the shear stress rate and thus make the mixing process “softer”. The mixers in the ÄKTA system are of plastic and have rounded corners, so that the rotating blades follow the circular geometry smoothly, but the relatively close

proximity of the stationary walls, could potentially induce large gradient in the boundary layer between the rotating agitator and the walls.

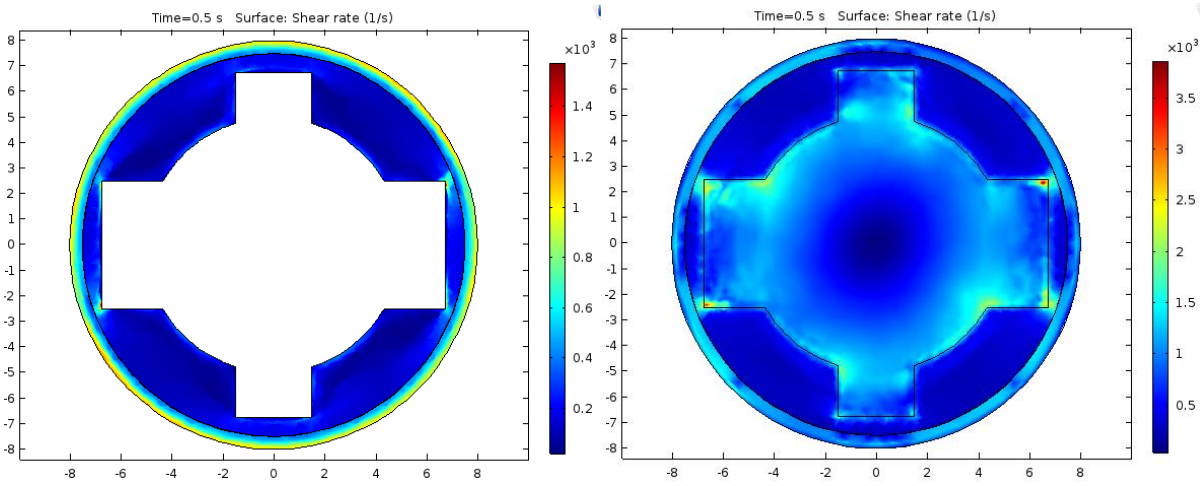

Figure 36: Shear rate viewed from bottom up, in middle of mixer(left) and bottom (right) t=0.50 s between agitator and the stationary wall with no slip boundary condition. Highest degree of shear rate, $\sim 3000\ s^{-1}$, is shown around the sharp edges of the geometries, in contact with the conical lower part of the geometry, depicted in the figure to the right. This effect could potentially be reduced by corner refinement and/or having the agitator spinning further away from the walls.

When discussing accuracy of the simulations, the low resolution of the simulations definitively has an impact on the result and therefore the simulations of the near wall modelling when determining gradients and shear rates should best be thought of as indicators rather than exact measurements and estimations. The low resolution can be seen in figure 37, showing the shear boundary layer in the yz-plane, in the middle of the mixer, between the rotor and stator. A plot of the velocity magnitude, and the shear rate in the radial direction, in figure 38, shows the velocity profile in the viscous boundary layer with an estimated boundary layer thickness of approximately 1.10 mm between the rotating agitator and the stationary wall. This was compared with the theoretically estimated value of approximately 1.03 mm using eqn. (4) based on a Re value of 2250.

A further notice of the laminar boundary layer, is of the nature of how the model was created in COMSOL MULTIPHYSICS. By creating two non-overlapping geometries, the region between the stationary wall with no slip boundary condition and the rotating domain, potentially creates an artificial boundary layer which introduces a jump discontinuity at the continuous boundary located 7.50 mm from the centre of the mixer, see figure 38, where the shear rate cannot be determined, which needs extra consideration when conducting the boundary layer analysis. Given that the shear rate is simply the gradient of the velocity field, approximated in the simulations by linear elements, we expect the shear rate to, approximately, vary linearly in the thin boundary layer between the rotator and the stationary wall. However, as the velocity field in the simulations does not exhibit a smooth parabolic like profile, the resolution is assumed to be the largest contributing factor of the zig zag shear rate profile, coupled with a jump discontinuity at the continuous boundary, which can be seen in figure 38. Possibilities to po-

tentially eliminate the jump discontinuity and smooth out the profile of the shear rate, is assumed to be as previously mentioned, mesh refinement around the boundary between the rotating and stationary domain.

As a final mention, discussing implementation of mixers, the increased shear rate from active mixing methods thus needs extra consideration when choosing appropriate mixing method for the process. If the product is shear sensitive, “softer” passive mixing methods as described in the previous section may be a better option.

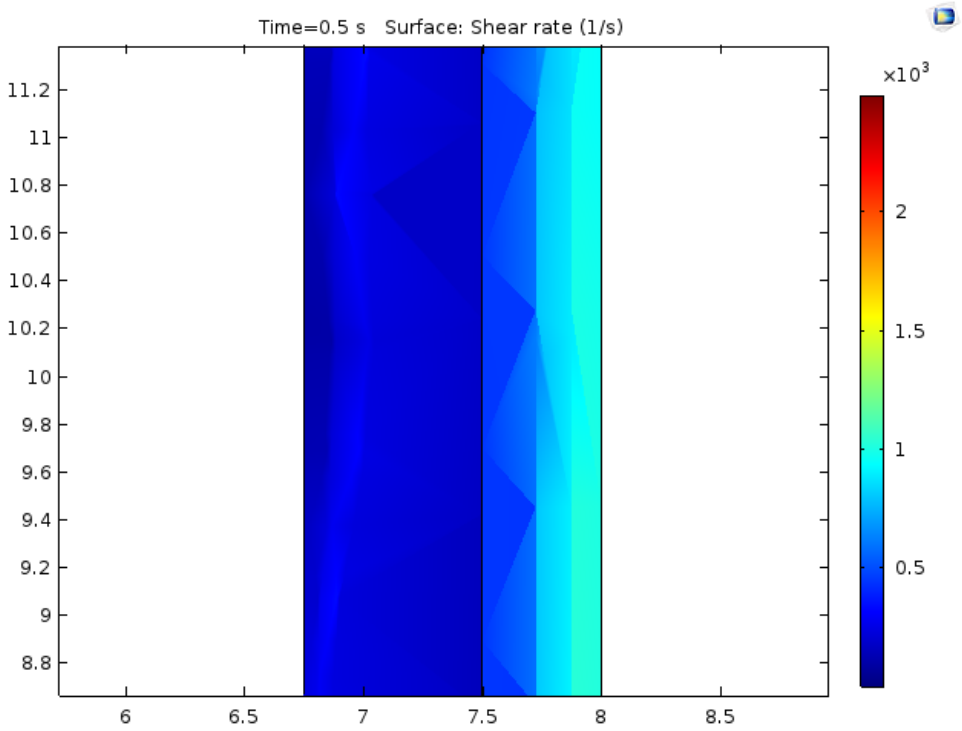

Figure 37: Low resolution of viscous boundary layer between rotating and stationary domain. Boundary between rotating and stationary geometry at 7.50 mm from the centre of the mixer.

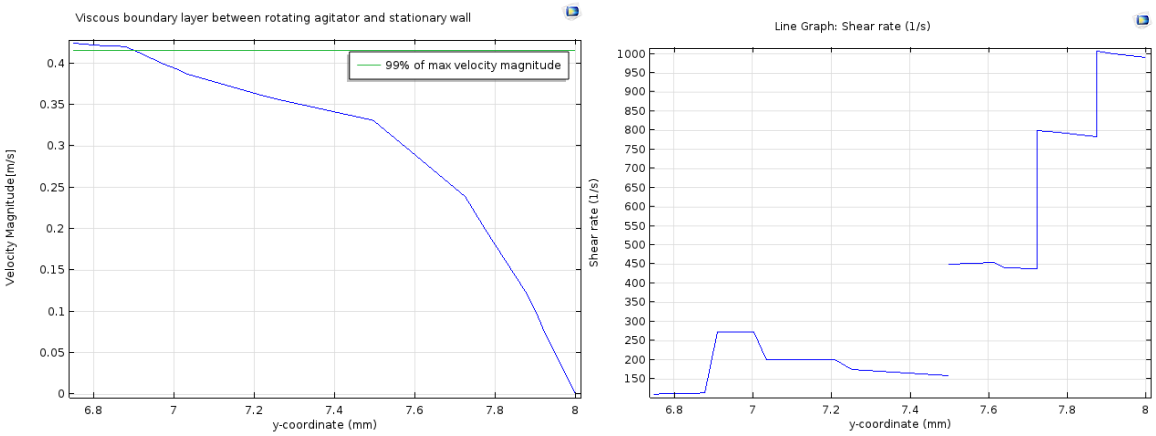

Figure 38: Velocity profile of laminar boundary layer with estimated boundary layer thickness of 1.10 mm, compared with theoretical estimation of 1.03 mm (left) and shear rate profile between agitator and stationary wall (right), with jump discontinuity at the boundary between the stationary and rotating domain located 7.50 mm from the centre of the mixer.

4.1.4 General comments CFD analysis

To sum up the CFD-analysis, three findings are worth mentioning. Continuum models have their difficulties related to them regarding the difficulties of accurate diffusion simulations and numerical instability, so choosing particle tracing as method could potentially be better for modelling the mixing process in hindsight with regards to stability, robustness and accuracy. The relative simplicity of describing distributions using continuous models, however was very useful when comparing different mixing configurations.

The computational load for the simulations was high with the longest simulations for the moving mesh simulations running for one-week, real time on a computer with eight core 2.26 GHz processor. Thus, more powerful computers and/or mesh optimization and optimization of the solver procedure is required to potentially lower the computational load and making the simulations more efficient. The only parameter in the numerical solvers that was tuned to lower the computational load was manually changing the relative tolerance of the solver to 0.01, from the default settings, in the transient simulations of the moving mesh. Otherwise all parameters in the stationary and dynamic solvers were kept at default which could potentially have effect on both the accuracy and computational load.

Choosing an appropriate mixing method for the process seems, to a large extent be based on the overall running parameters of the process. Continuous chromatography, is governed by several running parameters such as the volumetric flow rate during loading, washing and elution, which seems to set a practical limit on the effectiveness of using basic ÄKTA T-mixers as sole mixing method. Active mixing on one hand, intuitively seems being the most effective method when studying the stream lines of the velocity field. The method however, can be potentially be considered "hard" given the higher shear rates, compared with the soft mixing processes based on geometric ingenuity that is used in passive and static mixers. So, choosing the mixing method not only depends on what level of mixing that needs to be achieved, but also what you want to mix together. When mixing buffers, prior to applying a salt gradient in the process, active mixing using the dynamically stirred tanks are ok to use, in correspondence to the guidelines found in the manuals. When conducting inline dilution or virus inactivation, there is possibility that one needs to be more careful and passive mixing methods seems most advisable with a more well-defined dispersion, considering the more controlled mixing process and relatively speaking, more sensitive products involved. It should also be noted that the mixing quality in the configurations was examined purely based on the estimated mixing efficiencies and no investigation of axial dispersion, which needs to be avoided as much as possible to have a controlled mixing sequence, was investigated. The strength of the mix efficiency approach is generality, but more studies is likely needed to exactly investigate the feasibility of implementation, into continuous chromatography processes.

4.2 Experimental studies

4.2.1 Conductivity measurements

The discrete and analytical model both correlated with the experiments, while the analytic model gave a better fit over a wider range of different flowrates, assumed to be caused by differences in sensitivity to the dispersion. For the 64.2 cm tube at $Pe = 0.017$ and a volumetric flowrate of 1ml/min, the simulations (red lines) correlated with the experimental data (blue lines) at mixing ratios above 50% and started to deviate when the mixing ratio was 20 % or lower, indicating fluid segregation. The increase in deviation from average residence time with lower mix ratios, in the 642 mm tube, can be seen in figure 39 on the next page, where the

yellow line depicts the middle of the dispersion front, corresponding to the point of the average residence time, estimated from eqn. (31). The variance from the mean average residence time, $\bar{t} \approx 17\ s$, was estimated to approximately 40 seconds from eqn. (33), corresponding to a standard deviation of approximately $6.30\ s$. The deviation was most pronounced for ratios of 5 and 10 %, which showed increasing deviation from estimated average residence time, indicating that streamlines of the fluid carrying the solute got pushed to the outer regions of the mixing channel, due to the higher momentum of the opposing stream, thus a longer period was spent in the slower moving, outer regions of the tube than the average. This kind of deviation was also seen for the 20 and 40 cm tubes when mixing at lower ratios.

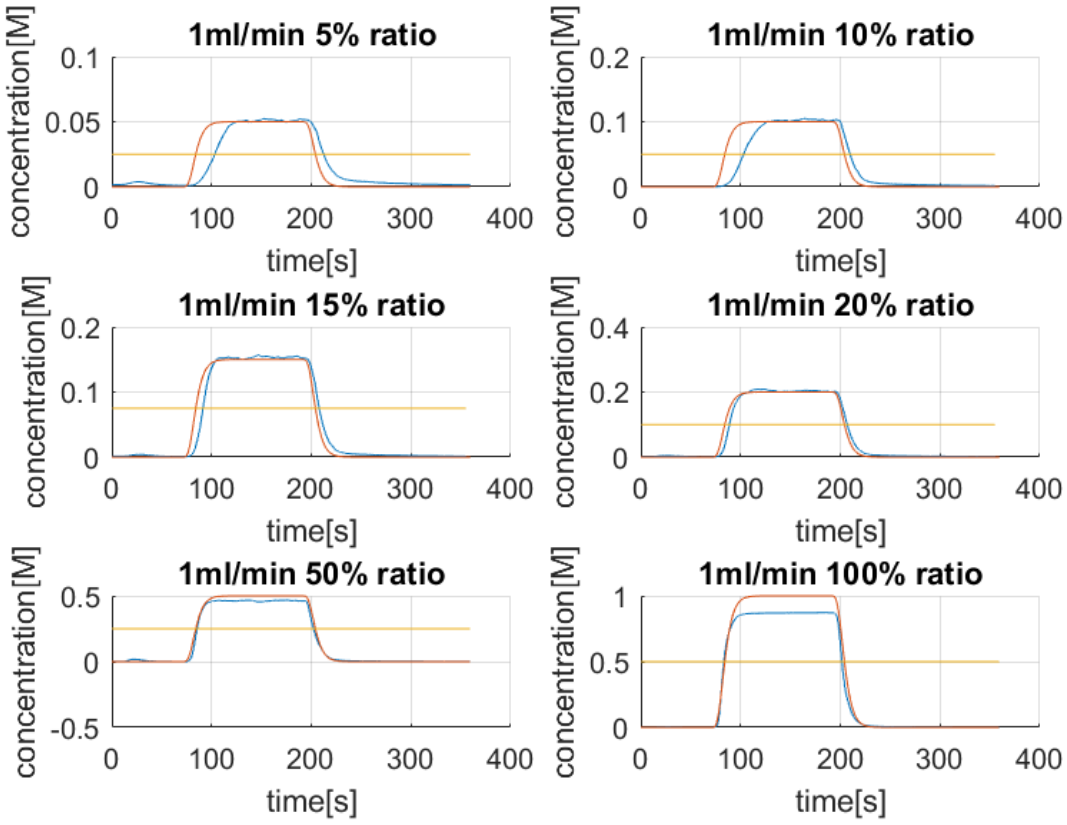

Figure 39: Pe=0.017 Flowrate 1ml/min different ratios ranging from 5 to 100% 1 M Na Cl at mixing point. Measuring-distance from mixing point was 642 mm. Red lines is analytical model, eqn. (40) and blue lines is experimental data. Yellow line depicts average residence time at concentration of $\frac{1}{2}\alpha$.

Experiments with 0.10 M and 1 M Na Cl solution, showed no apparent difference in mixing, seen in figure 40. The difference in measuring signal at steady state for 1 M was assumed to be due to the non-linear relationship between conductivity and concentration at higher concentrations. The TDS-conversion factor used for 0.10 M was 0.58 and 0.65 for 1 M. For the 0.10 M experiments, the configuration was asymmetric, while experiments with 1 M, was run using the symmetric configuration. The experiments were also done for different tube lengths and mixing ratios which need consideration when evaluating the results.

Due to the simplicity, relative low resolution and quality of the conductivity measurements it was difficult to see any difference in deviation from the mathematical models, with only a slightly higher deviation for 2ml/min, when comparing between asymmetric and symmetric configuration of T-mixer for different flowrates, which can be seen in figure 41.

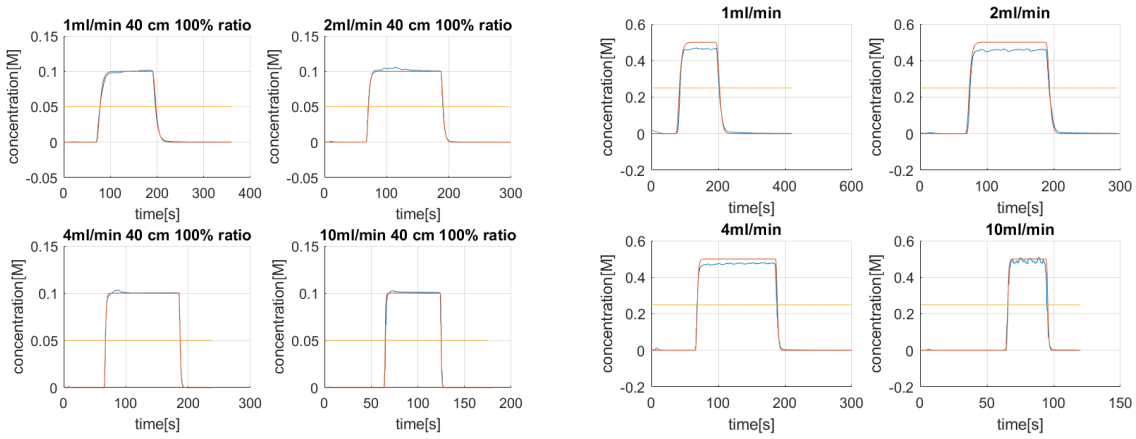

Figure 40: Conductivity measurements for 1 M (right) and 0.10 M Na Cl (left).

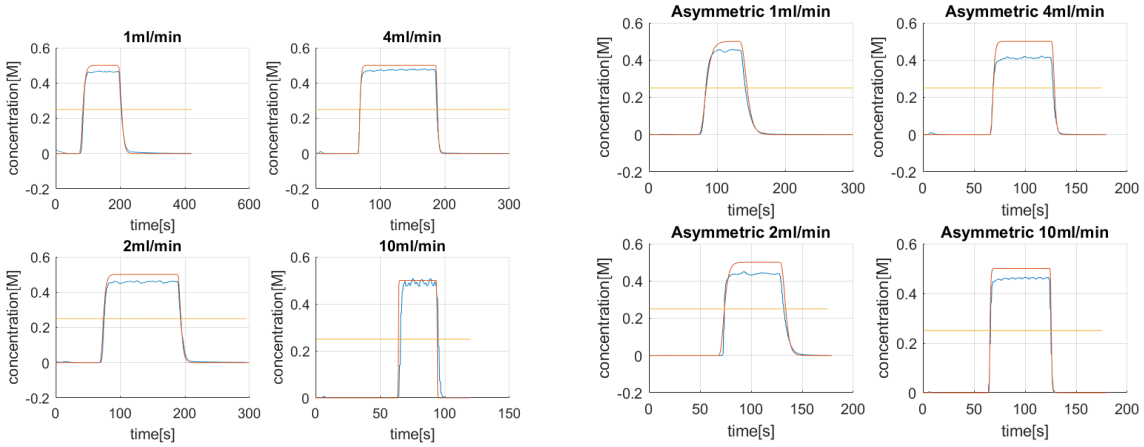

Figure 41: Symmetric configuration (left) and asymmetric configuration (right).

As a concluding remark for the conductivity measurements, were that they provided most information for estimating stratified and segregated flow by examining deviation from average residence time for an approximately ideal step-response at different mixing ratios. The measurements of different mix ratios however, strengthened the notion that in liquid flow, solute carried by the fluid, mainly becomes advected by the flow field and simply seems to travel along the streamlines. Without transversal flows in the mixing channel at higher Reynolds values this leads in practice, to no mixing, thus resulting in complete stratification between the inlet fluids at lower flowrates. In the other experimental cases, the measurements gave less information of the mixing process in the T-mixer.

4.2.2 Ethanol-Water visual experiments

Since the water flow is blue and the ethanol flow is yellow, a good indication of mixing is if the solution becomes green colored in the tube. In addition, a good indication of no mixing is when the separation in color between the fluids is seen.

The results showed that the mix ratio is not a determining factor when it comes to mixing, but the flow rate of the fluids seems to influence the mixing in the T-mixer. The fluid becomes mixed at flowrates above 10 ml/min which can be seen for mix ratios of 10 up to 50%. The results show that there was no mixing for a flow rate lower than 10 ml/min, which can be seen in the diagram in figure 42. It should also be noted when examining the results that the experiments for the higher flowrates approaching 10 ml/min, were primarily used to investigate the cause of the increased mixing occurring at 10 ml/min and therefore not all the different mix ratios were tested at higher flowrates.

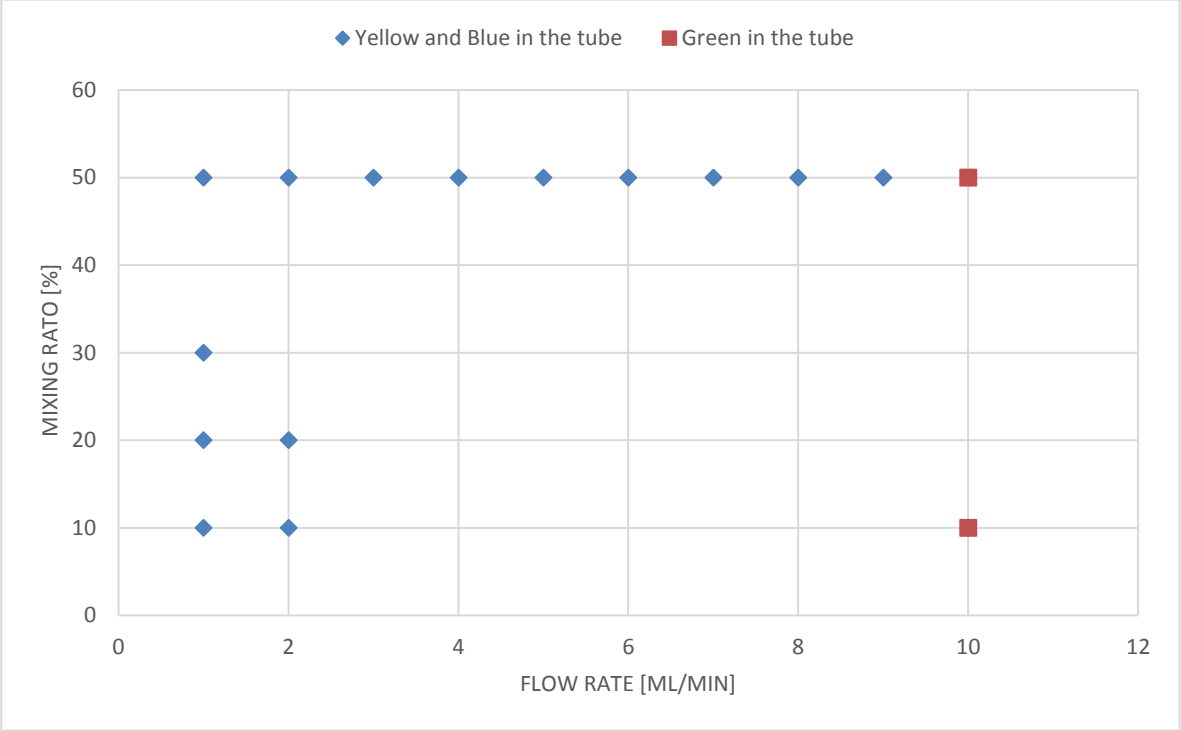

Figure 42: Visual experiments for water-ethanol. Red squares indicate mixing while blue diamonds indicate no mixing and difference in colour in the tube.

A comparison between the colors for two different color experiments, using water and ethanol can be seen in figure 43. The picture to the left side represents 1ml/min and 50 % mix ratio, showing a clear sign of two different colors and the picture to the right represents experiment 10 ml/min and 50% mix ratio showing a green colored fluid in the tubes. These results are identical to the results from the 1 M NaCl solution runs.

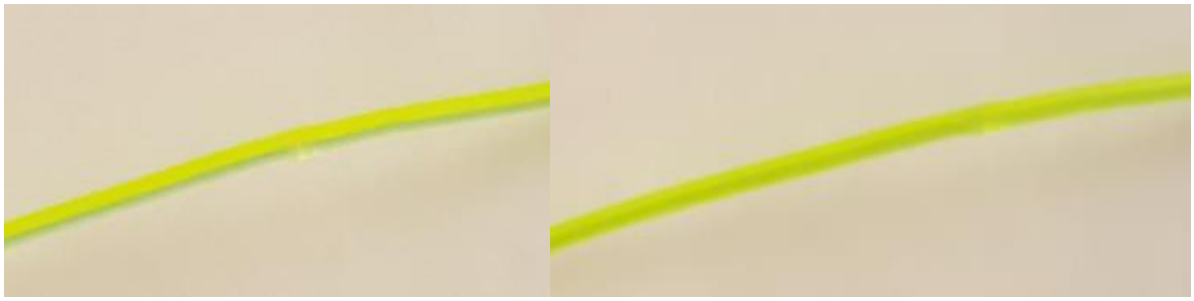

Figure 43: Left figure show fluid segregation at flowrate 1ml/min compared with apparent complete mixing at 10 ml/min for mix ratio of 50%.

These effects occurring at 10 ml/min, were further investigated by making a series of conductivity experiments where a set of low mix ratio experiments was made and compared to the analytical model. The analytical model showed in section 4.2.1, that there was sign of flow segregation when the mix ratio was below 20%. On the other hand, setting a high flow rate seemed to cause the solutions to mix and give the green colour inside the tube.

The parameters set for the two experiments were a flowrate of 10 and 50 ml/min, and a mix ratio of 10%, which showed correlation between the analytical model and the experiments. This further strengthened the notion that something causes an increased mixing at flowrates of 10 ml/min or higher which can be seen in figure 44.

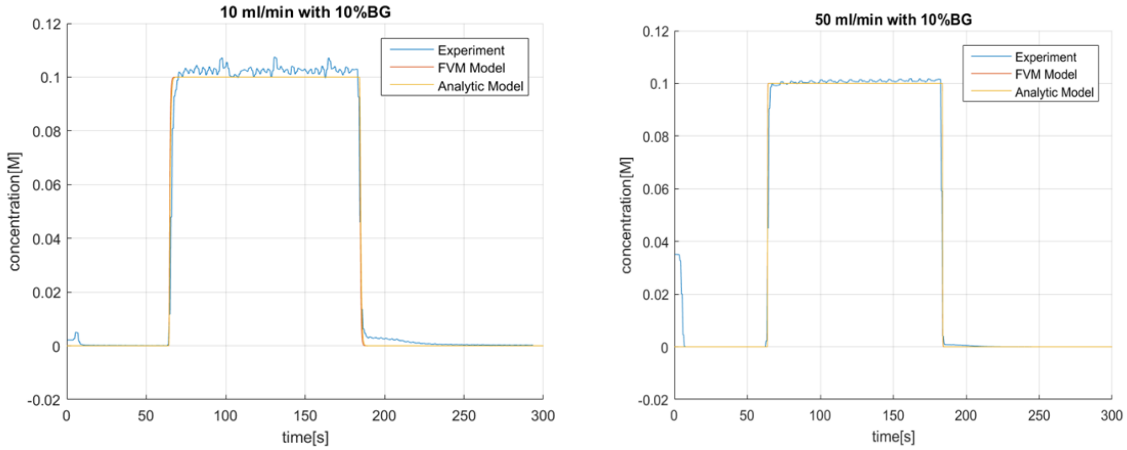

Figure 44: Mixing at 10 and 50 ml/min.

4.2.3 Pump study

By starting each pump alone there were no fluctuation in the conductivity curve. When running both pumps, interesting results occurs that is shown in the figure 45 below.

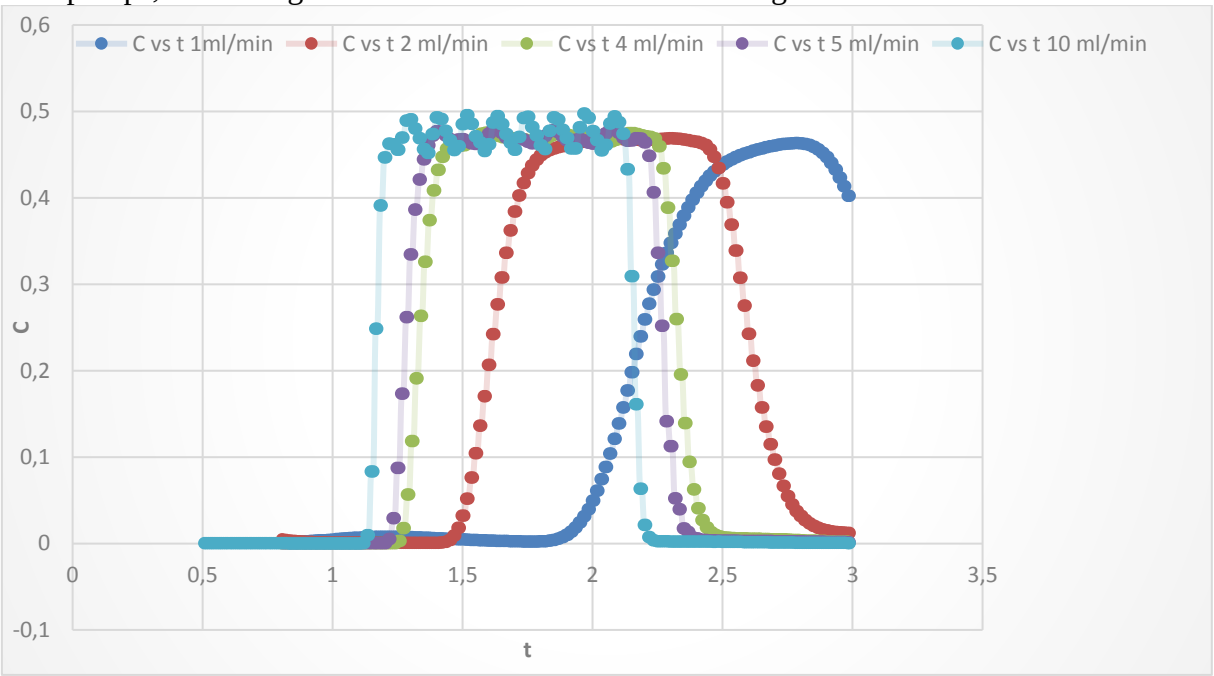

Figure 45: Conductivity curve measured at different flowrates.

This figure shows that the fluctuations occur only when increasing the total flow rate above 2 ml/min and that the frequency of the fluctuations increases when the total flow rate is increased. Another thing to notice is the substantial increase in both the size and the frequency when setting the flow rate to 10 ml/min or above. It seems when setting the flow rate at 10 or higher, the pistons in the pumps seems to be moving a longer distance compared to the lower flow rates. This mechanical movement causes the fluids in the system to mix, which is the reason behind the green coloured fluids in the tubes. (Healthcare, 2005)

Thus, the increased mixing at 10 ml/min is assumed to be attributed to a mechanical factor within the ÄKTA system, which changes a gear of some sort that makes the pumps work stronger at 10 ml/min and not due to engulfment flow, as was investigated in the CFD analysis. Another thing to add is when setting the flow rate above 10 is that the flow in the tube shows a pulsating behavior where both flows sends into the tubes periodically.

4.2.4 Dynamic mixer experiments

The dynamic mixer showed apparently, complete mixing when conducting the visual experiments which was as expected. The upside of using the stirred tank is avoiding the usage of high flow rates, which lowers to probability of damaging the equipment of the ÄKTA system. Table 3 shows the different experimental runs and the results that were made during this study.

Table 3:Visual Experiments using Dynamic Mixer.

# of the experiment	Flow rate ml/min	BG %	Color in the tube
1	1	50	Green
2	1	10	Green
3	2	50	Green
4	2	10	Green

4.2.5 General comments about the experimental part

Understanding the correlation between the model world and the real measurements in the experiments, was one of the biggest challenges with the conductivity measurements. There remains a degree of uncertainty regarding the exact time slots and time correlation between model and the connection between the ÄKTA-UNICORN, measurements and potentially more investigations regarding measuring technology are therefore needed to provide further knowledge. Thus, being able to make visual experiments, proposed a powerful tool for examining the fluid mechanics of the system, even though it was not directly quantified and compared with the CFD simulations. A final mention of the visual experiments, were that though they provided invaluable information, the relatively simple set-up and camera used for the experiments, meant that using a higher resolution camera could potentially give even more exact readings, regarding the degree of fluid segregation in the tubes, for different flowrates and mix ratios.

The way of how the ÄKTA system is used with the chromatography column, the flow rates are going to be very low to avoid damaging the column and other equipment in the ÄKTA system. The trade-off of having a low flow rate is that the mixing in the system seems to be less efficient, which potentially can have other consequences when running the process. But even when increasing the flow rates to 10 ml/min or above, the strain that is put on the system is not sustainable for the pumps life cycle or the process. The pump study indicates that by increasing the flow rate, the pistons starts to move faster until it reaches 10, where it seems that the pumps goes into an extra "gear" which makes the pistons move a longer distance that is long enough to create fluctuations in the solute stream sent into the T-mixer, large enough to cause mixing. An important thing to consider is when investigating the pumps, there were some units such as flow restrictor present that might help in lowering the effect of the pumps. However, when both salt measuring experiments and the visual experiments were made the process was stripped from units that were unnecessary, units such as flow restrictors to remove some time lag from the process and make it easier for the analytical model to compare to the experimental data. If the flow restrictors were present in the experiments it would have lessened the disturbances created by the pumps but that would have also meant that the mixing potentially, would become worse.

5 Conclusion

Simulations of a T-mixer, three different stationary mixer configurations and active mixers with rotating magnetic agitators were simulated in COMSOL MULTIPHYSICS. Experiments were simultaneously conducted in ÄKTA to verify and compare with the simulations.

The overall picture when summarising CFD-analysis and experiments, was that flow in ÄKTA when running continuous chromatography at flowrates <10 ml/min, is most likely in the stratified flow regime, thus setting a practical limit on the effectiveness of the T-mixer, meaning that additional active and/or passive mixers are required to increase mixing to desired levels. By running a variety of conductivity and visual experiments, coupled with the CFD analysis it thus seems that the mixing in the ÄKTA system is mainly diffusion based, especially when using the T-mixer at low flow rates. The factor that seemed to contribute most to increased mixing, was the pumps. When setting the pumps to a flow rates above 10 ml/min, the pistons inside the pumps started to desync which created a disturbance in how the inlets was sent into the mixer. This desync lead to improved mixing which was visible both in the visual- and conductivity experiments. However, the downside when setting the pumps at very high flow rates is shortening of the life cycle of the pumps and potential damage to other process equipment that cannot handle the large pressure drops created by the higher flowrates. An example of such equipment is the chromatography column, which is the most important equipment in the entire process.

Due to the difficulties related to giving accurate answers and estimations regarding diffusive mixing, there remains a degree of uncertainty of the exact quantification of which type of active/passive mixers which is most effective to implement in the process. As seen in the visual experiments, by utilizing the magnetic field provided by the ÄKTA system, the stirred tank can mix the fluids to the point to where the colour inside the tube becomes green, which indicate a degree of homogeneity, but due to the difficulty of simulating the stirred tank with continuum models, the mixing efficiency, remains unknown. While there was no static mixer to experiment on, it is likely the choice of type of mixer to choose for the process. The simulations of the static mixer were very promising, the mixing efficiency is quite high at low flowrates, especially for the static mixer with helical shaped baffles. The upside with the static mixer is that there is no need to extra energy source to power it up, since the mixing is governed to a large extent due to the geometry of the mixer. The relative simplicity of the technology and ease of implementation with potential to develop own passive mixers from scratch are also factors to consider. The governing parameters controlling the mixing process such as flowrate and geometry is potentially also easier to control compared with the stirred tank with the rotating agitator. The smoothness properties of the stationary mixers compared with the active mixer when it comes to shear rates, is also a point to consider, when mixing shear sensitive compounds.

6 Further work

Further work within the subject of CFD, would most likely focus on optimisation of the continuum based models investigated in this thesis and developing advection diffusion models using Lagrangian particle dynamics by simulating advection and diffusion by using the particle tracing module in COMSOL MULTIPHYSICS. Also, analytical computations to exactly establishing the diffusive rate in circular tubes could potentially be used as an additional safety measure to compare with numerical simulations to establish the time it takes to reach homogeneity in the tubes by pure diffusion for different concentrations and diffusivities.

The analytical and discrete model used to simulate the experimental cases for the salt concentration measurements in the ÄKTA system is potentially a powerful analytic tool to estimate dispersion effects on average residence time distributions in the tubing which becomes useful when estimating continuous virus inactivation and stratified flow estimation based on experimental observations, but it is far from a complete model and lacks resolution for describing the exact mixing process.

To quantify the mixing process from the transient pump effects, a list of suggestions can be seen in this section of how to improve the simulation to make it closer to the experimental setup. The first thing to start with is the pumps and their effect on the ÄKTA system. This is one of the most essential things to add to the CFD simulations since the mixing can only occur at 10 ml/min with the help of the desynchronization of the pump. This can be done in two ways; a creation of a pump must be done either in COMSOL or by entering a sinus function that starts once the step response has reached 100% of the signal value to simulate the fluctuations that were present in all the conductivity measurements.

A thing to consider on the experimental side is the passive mixers. In this project, a static mixer was built but unfortunately, air bubbles were obstructing the path of the fluid, which made the mixer less efficient and therefore the experimental static mixer results were not included in this project.

7 References

5.3a, C. M., 2018. *www.comsol.com.* [Online] Available at: https://www.comsol.com/model/download/461711/models.chem.laminar_static_mixer.pdf [Använd 11 May 2018].

Alveteg, M., 2015. *Handbook.* 1 October 2015 red. Lund: Department of Chemical Engineering, Faculty of Engineering, Lund University.

Alveteg, M., 2015. *Introduction to separation processes and transport phenomena.* Lund : Department of Chemical Engineering Lund University.

Analytical, R., 2018. *Conductivity Theory and Practice.* [Online] Available at: http://www.analytical-chemistry.uoc.gr/files/items/6/618/agwgimometria_2.pdf [Använd 11 May 2018].

Andersson, B. o.a., 2012. *Computational Fluid Dynamics for Engineers.* 1 red. United Kingdom: Cambridge University Press.

Andreusssi, T. o.a., 2015. Flow Regimes in T-shaped micromixers. *Computers and Engineering*, 76(1), pp. 150-159.

Aref, H., 2002. Development of Chaotic Advection. *Physics of Fluids,* 14(4).

Aref, H. B. L. P. & Stremler, A. M., 2000. Topological fluid mechanics of stirring. *Physics of fluids,* 403(1), pp. 277-304.

COMSOL, 2012. *COMSOL MULTIHYSICS.* [Online] Available at: http://www.lmn.pub.ro/~daniel/ElectromagneticModelingDoctoral/Books/COMSOL4.3/particle/ParticleTracingModuleUsersGuide.pdf [Använd 14 May 2018].

COMSOL, 2015-2017. *www.comsol.com.* [Online] Available at: https://www.comsol.com/model/download/461711/models.chem.laminar_static_mixer.pdf [Använd 15 May 2018].

Cortes-Quiroz, C., Azarbadegan, A. & Zangeneh, M., 2017. Effect of channel aspect ratio of 3-D T-mixer on flow patterns and convective mixing for a wide range of Reynolds numbers. *Sensors and Actuators,* pp. 1153-1176.

Dizechl, M. & Marshall, E., 1982. Viscosity of some binary and ternary liquid mixtures. *Journal of Chemical Engineering Data,* 27(1), pp. 358-363.

Elman, H. C. & Ramage, A., 2001. A characterisation of oscillations in the discrete two dimensional convection- diffusion equation. *Mathematics of computation,* 72(1), pp. 263-288.

Galetti, C., Roudgar, M., Elisabetta, B. & Mauri, R., 2012. Effect of inlet conditions on the engulfment pattern in a T-shaped micro-mixer. *Chemical Engineering Journal,* 185-185(1), pp. 300-3013.

Hai Lang, Z. & Han, S.-. J., 1996. Viscosity and density of water + Sodium Chloride+ Potassium Chloride Solutions at 298.15 K. *Journal of Chemical Engineering Data,* 41(1), pp. 516-520.

Hardt, S. & Schönfeld, F., 2007. *Microfluidic Technologies for Miniaturized Analysis Systems, eds.* e-ISBN 978-0-387-68424-6 red. New York: Springer Science+Business Media LLC 223 Spring Street .

Hauke, G., 2008. *An introduction to Fluid Mechanics and Transport Phenomena.* 1 red. Spain: Springer Science and Business Media.

Healthcare, G., 2005. *Marshallscientific.com.* [Online] Available at: https://www.marshallscientific.com/v/vspfiles/files/manuals/p900pump.pdf [Använd 16 05 2018].

Healthcare, G., 2015. *issuu.* [Online] Available at: https://issuu.com/marshallscientific/docs/akta_fplc_explorer_100_operator_s_g [Använd 13 June 2018].

Iserles, A., 2009. *A First Course in the Numerical Analysis of Differential Equations.* 2nd red. Cambridge: Cambridge University Express.

Mathew, G., Mezic´, I. & Petzold, L., 2005. A Multiscale Measure for Mixing. *Physica D,* 211(1), pp. 23-46.

MULTIPHYSICS, C., 2013. *www.comsol.com.* [Online] Available at: https://www.comsol.com/blogs/understanding-stabilization-methods/ [Använd 15 May 2018].

Orsi, G. o.a., 2013. Water- ethanol mixing in T-shaped microdevices. *Chemical Engineering Science ,* 95(1), pp. 174-183.

Renardy, M. & Rogers, R., 2004. *An introduction to Partial DIfferential Equations.* 2 red. New York: Springer Verlag.

Schikarski, T., Peukert, W. & Avila, M., 2017. Direct numerical simulation of water-ethanol flows in T-mixer. *Journal of Chemical Engineering ,* 324(1), pp. 168-181.

Sciences, G. H. L., 2012. *https://www.gelifesciences.com/akta.* [Online] Available at: http://cdn.gelifesciences.com/Dmm3BWSV3/assetstream.aspx?assetid=19223&AssetOutputIdent=44&accesskey=dc4ebb6a-d79e-4b48-9068-1e4c88871fdf&download=true [Använd 11 June 2018].

Sellberg, A., 2018. *Open Loop Optimal Control of Chromatographic Separation Processes.* 1 red. Lund: Department of Chemical Engineering .

Spanne, S. & Sparr, A., 1996. *Föreläsningar i Tillämpad matematik, Lineära system.* Lund: KF-Sigma.

Sparr, G. & Sparr, A., 1999/2000. *Kontinuerliga System.* 2:8 red. Lund : Studentlitteratur.

University, C. S., u.d. *www.math.colostate.edu.* [Online] Available at: http://www.math.colostate.edu/~pauld/M545/L%20Transform.pdf [Använd 14 May 2018].

Warfvinge, P., 2015. *Process and Reactor Calculations.* Academic Year 2015/2016 red. Lund: Department of Chemical Engineering .

Vitagliano, V. & Lyons, P., 1995. *Diffusion coefficients for Aqueos Solutions of Sodium Chloride and Barium Chloride ,* u.o.: Department of Chemistry Yale University.

8 Appendix A-Populärvetenskaplig sammanfattning

Vi har alla varit med om det när vi stått och rört runt med skeden i morgonkaffet. De fantastiska, komplexa mönster som uppträder när grädden blandar sig med det mörka kaffet, efterhand som vi rör runt med skeden. Även om du kanske själv aldrig har reflekterat över det så är den här typen av mixning och blandningsförlopp, komplexa fenomen som studerats av och sysselsatt forskare, vetenskapsmän och matematiker under lång tid.

Mixning bygger på en rad komplexa transportfenomen och är till stor del styrt av typen av flöde och hur strömningsförhållandena är. Kaffekopps exemplet är exempelvis ett bra exempel på materialtransport där skeden står för den så kallade advektionen, som står för den storskaliga förflyttningen av partiklar och diffusion, som är exemplet på den spontana, naturliga blandningen man fått om man bara låtit grädden blanda sig i kaffet av sig själv, utan omrörning.

Den största skillnaden mellan små och storskaliga mixningsprocesser är hur dessa två processer samspelar och hur flödesmekaniken beter sig i de olika skalorna. I storskaliga flöden så är kaotisk mixning med hjälp av turbulens det vanligaste sättet som används för att effektivt blanda olika vätskor medan vid mindre skala blir det jämförelsevis, allt svårare att åstadkomma turbulens på grund av de mindre geometriska förhållandena. Flödet karaktäriseras istället av så kallad laminäritet där friktionskrafterna i vätskan åstadkommer ett mycket välordnat flöde jämfört med det kaosartade flödet som uppstår vid turbulens, vilket gör det svårare att bryta upp vätskornas materialstruktur och åstadkomma en bra blandning på liknande vis som när vi rör ner grädde i kaffet eller blandar vår favorit saft. För att mixa olika vätskor innebär detta därför att det krävs någon form av ytterligare hjälp från en teknisk apparat som kallas för mixer.

Mixrar som används i dagens applikationer kan i stort delas in i två kategorier, aktiva mixrar som drivs av en extern kraftkälla och innehåller rörliga delar som rotorblad eller impellrar som fungerar som en form av mekanisk omrörning, tänk hushållsmixern där hemma i köket, medan passiva mixrar utnyttjar istället smart geometrisk design och de fluidmekaniska förhållandena för att förbättra mixningen. Nedan visas en bild av strömningslinjerna i en simulerad dynamisk mixer med en magnetomrörare och en statisk mixer som visar hur mixningen kan förbättras med olika metoder.

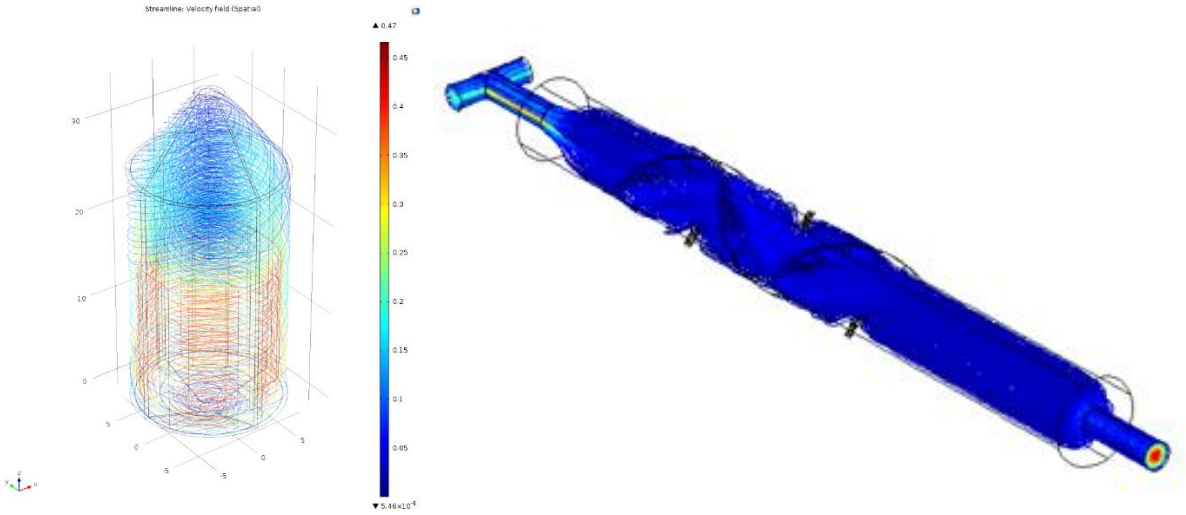

Genom att genomföra kopplade simuleringar och experiment genom att blanda vätskor i ett T-kors och mäta salthalten efter inblandningen, kunde studenter från Lunds Tekniska Högskola fastställa och se hur pass välblandad vätskan var i en små skalig kromatografiprocess. Den samlade bilden av datorsimuleringarna och experiment verkade visa på hur två vätskor som inte utsätts för ytterligare mixning från passiva eller aktiva mixrar, helt enkelt lägger sig jämte varandra och inte blandas på det sätt som man intuitivt kan tänka sig.

I slutändan blir mixern därför en oumbärlig del i en process för att kunna ha en bra och effektiv omblandning, på precis samma vis som vi måste röra runt i kaffet med skeden istället för att vänta och bara låta kaffet och grädden blanda sig spontant på egen hand.

9 Appendix B-Simulation of Dynamic Mixer in COMSOL MULTIPHYSICS

1. Start COMSOL MULTIPHYSICS and select the Physics Module *Rotating Machinery Laminar Flow*. Click add and then done.
   Global Definitions
2. Locate the **Global Definition** section and right click. Choose **Parameters** and type in the parameters given in the figure below.

Settings

Parameters

Parameters

Name	Expression	Value	Description
Din	15 [mm]	0.015 m	Diameter of Rotating Domain
H	16[mm]	0.016 m	Height of mixing chamber
Dstirrer	10[mm]	0.01 m	Diameter of Magnetic agitator Cylindrical Part
Hstirrer	16[mm]	0.016 m	Height of magnetic agitator

   Geometry
3. Locate the Geometry Section and select choose unit. Change from [m] to [mm].
4. *Cyl1*- Locate the geometry section and choose **Cylinder**. In *radius* type **Din/2.** In *height* type **H**.
5. *Cone1*- Right click on geometry and choose **Cone.** In *bottom- radius*, type **Din/2**. In height, type 8. In *specify top size using* choose **Radius** and type **1**. In *position* type **H** in z.
6. *Cone2*- Add another **Cone** and choose *bottom -radius* 1, height 2, *specify top size using* radius, type **Din/2**. In position type **-2** in z.
7. *Uni1* Right click **geometry-Booleans and Partitions** and choose **Union**. Choose, *Cyl1, Cone1, Cone2* as input objects and uncheck, **keep interior boundaries**.
8. *Cyl2*- Locate the geometry section and choose **Cylinder**. In radius type **Din/2+0.5.** In height type **H**.
9. *Cone3*- Right click on geometry and choose **Cone.** In bottom- radius, type **Din/2+0.5**. In height, type 8. In **specify Top size using** choose **Radius** and type **1.5**. In *position* type **H** in z.
10. *Cone4*- Add another **Cone** and choose *bottom -radius* **1.5**, height **2**, specify top size using radius, type **Din/2+0.5**. In position type **-2** in z.
11. *Copy1*-Next follows making an exact copy of *Uni1* by right clicking **Geometry-Transforms-Copy** and choosing *uni1*
12. *Uni2*- take the union between *Cyl2, Cone3* and *Cone4* by similar procedure as *Uni1*
13. *Diff1*-Next we take the difference between *Uni2* and *Copy1* as a foundation for creating the two separate geometries used for defining a rotating and stationary domain. Right click **Geometry-Booleans and Partitions-Difference** and Choose objects to add *Uni2*, objects to subtract, *Copy1*.
14. Click Build- All.
15. Next, we build the geometry for the magnetic agitator.
16. *Cyl3*-In the radius section, type **Dstirrer/2**. In height, type **H**.

17. *Blk1*- In width, type **3.5**, depth, type **5** and height, type **H**. For position choose, **Base** and **5** for x position. For z, type **Hstirrer /2.**
18. *Copy2*- Right click **Geometry-Transforms- Copy** and choose *blk1*
19. *Rot1*- Right click **Geometry-Transforms- Rotate** and choose *copy2.* In rotating angle, type 180.
20. *Blk2*- Build another block and choose width, 3, depth, 3.5 and height, type **Hstirrer**. Choose center as base and type 5 for y position and **Hstirrer/2** for z.
21. *Copy3*- Right click **Geometry-Transforms- Copy** and choose *blk2.*
22. *Rot2*- Right click **Geometry-Transforms-Rotate** and choose *copy3.* In rotation angle, type 180.
23. *Uni3*- Right click **Geometry-Booleans and Partitions-Union** and choose *cyl3, rot1, copy2, rot2, copy3.* Uncheck, keep interior boundaries.
24. *Diff2*- Right click **Geometry-Booleans and Partitions- Copy** and choose objects to add *uni1*, and objects to subtract, *uni3.*
25. *Fin*- Go to **Form Assembly** and choose action, **Form Assembly** and check the box for create pairs, pair type, **Identity Pair**.
26. *Ap1*- Click Build all. An identity pair should have been created in **Component 1-Definitions**

Materials

27. Right click **Materials** and choose Water, liquid.

Physics- Rotating Machinery-Laminar flow

28. *Rotating wall1*- Check that only the boundaries of *Uni3,* is chosen. See figure (16)
29. *Rotating Domain 1*- Right click *Physics- Rotating Machinery-Laminar flow*- **Rotating Domain.** Locate the rotating domain section and select domain 2. In Revolutions per time change to Rotational frequency and set revolutions per time to 10[$\frac{1}{s}$].
30. *Inlet 1*- Choose **Inlet** and choose boundary 57, normal inflow velocity, type 0.025 [$\frac{m}{s}$].
31. *Outlet1* – Choose **Outlet** and pressure constraint, pressure 0, suppress backflow and choose boundary 56.
32. *Flow Continuity1*- Right click *Rotating Machinery-Laminar flow* and choose **Flow Continuity**. Select Identity Pair 1. See figure (14)

Mesh

33. Select Normal and choose Build all. See figure (15)

Study1

34. Choose Frozen Rotor study. Click Compute.

Results1

Streamlines

35. *3D- plot group Velocity(rmspf) Streamlines* Right click and choose add **streamlines**, choose uniform density and type 0.02 for the separating distance. Right click on **streamlines** and Choose add Colour Expression. Click plot all.

Study 2

36. Add another study and choose Time Dependent. Go into **Values of Dependent Variables** and expand the section **Initial values of Variables solved for** and go to **Settings,** change to user defined and choose **Method-Solution, Study 1-Frozen Rotor, Automatic** to start the transient simulation from the Frozen Rotor Solution. In **Times,** type

range (0,0.1, 0.5) and then click compute. The result will show that steady state is reached after approximately 0.1 seconds, starting from the Frozen Rotor Solution. This is usually the best way of getting accurate steady state simulations compared with only computing the Frozen Rotor Solution.

Results2
Streamlines

37. *3D plot group Velocity field(rmspf) (1) Streamlines*- Same procedure as for the Frozen Rotor Solution. In selecting data set, change to study 2 and choose time 0.5 s. Click plot all

Data Sets

38. *CutPlane1* In Results go to Data sets and Right Click. Choose **Cut Plane** and choose xy planes. In choosing data set choose Study 2. Type 10 in the z position to plot the xy-plane in the middle of the geometry. This data set is used to plot the velocity field in the plane above the rotating agitator.
39. *Cutplane2* In Results go to Data sets and Right Click. Choose **Cut Plane** and choose yz planes. In choosing data set choose Study 2. This data set is used to plot the shear profile in between the rotating agitator and the stationary walls.
40. *Cutline1* In Results go to Data sets and Right Click. Choose **Cut Line 3D 1** and choose two points as line entry method. Type (x,y,z)=(0,6.75,10) for entry point one and (x,y,z)=(0,8,10) for entry point 2. Choose data set, Study 2.

Arrowsurface

41. Left click Results and choose **2D** plot group. Choose data set *Cutplane1*. Left Click **2D**-plot group and choose arrow surface. Click Plot

2D plot group Shear Rate profile-Cutplane1

42. Left click Results and choose **2D** plot group. Choose data set *Cutplane1*. In expression change to *rmspf1.sr*. Click Plot

2D plot group Shear Rate profile-Cutplane2

43. Left click Results and choose **2D** plot group. Choose data set *Cutplane2*. In expression change to *rmspf1.sr*. Click Plot

Velocity profile between rotating agitator and stationary wall
2D Shear Rate profile-Cutline 3D 1

44. Left click Results and choose **1D** plot group. Choose data set *Cutplane1*. Left click **1 D** plot group and choose **Line Graph**. In expression change to *rmspf1.U*. On axis, replace expression by typing **y**. Click Plot

Shear rate profile between rotating agitator and stationary wall
2D Shear Rate profile-Cutline 3D 1

45. Left click Results and choose **1D** plot group. Choose data set *Cutplane1*. Left click **1 D** plot group and choose **Line Graph**. In expression change to *rmspf1.sr*. On axis, replace expression by typing **y**. Click Plot

10 Appendix C-Analytical model

The boundary value problem with solution given by (10), for a chemical species under a Parabolic evolution law was studied when comparing mixing experiments and macroscopic mathematical modelling of mixing. Here follows the complete description of the mathematical model and the step by step method of finding a solution to the problem. The problem statement differs from the ordinary formulation of initial value problems since we are assuming that we have equations that describes the system for all t, but the system is initially at rest prior to perturbation. That means that we are looking for causal solutions (9). We study the following problem.

$$\begin{cases} \partial_t u - D_{ax}\partial_x^2 u + \bar{v}\partial_x u = 0 \; x > 0, , t \in \mathbb{R} \\ u(0,t) = \alpha\left(\left(\Theta(t-\beta) - \Theta(t-\gamma)\right), t \in \mathbb{R}\right. \end{cases} \tag{C.10.1}$$

We use linearity of the equation and the super- positioning principle to write $u = u_1 + u_2$. We then get the following two problems which we solve independently.

$$\begin{cases} \partial_t u_1 - D_{ax}\partial_x^2 u_1 + \bar{v}\partial_x u_1 = 0 \; x > 0, t \in \mathbb{R} \\ u_1(0,t) = \alpha\Theta(t-\beta), t \in \mathbb{R} \end{cases} \tag{C.10.2}$$

$$\begin{cases} \partial_t u_2 - D_{ax}\partial_x^2 u_2 + \bar{v}\partial_x u_2 = 0 \; x > 0, t \in \mathbb{R} \\ u_1(0,t) = -\alpha\Theta(t-\gamma), t \in \mathbb{R} \end{cases} \tag{C.10.3}$$

Since $f(t) = \Theta(t-\beta)$ is causal, i.e system at rest $t < \beta$ we take the partial Laplace transformation of (1) with respect to t. Note that since we have a causal problem we do not take the one- sided Laplace transformation with regards to t, thus ignoring the initial value condition. We thus define

$$U(x,s) := \mathcal{L}_t u(x,s) = \int_{-\infty}^{\infty} e^{-st} u(x,t)dt \tag{C.10.4}$$

$$F(s) := \mathcal{L}_t f(s) = \int_{-\infty}^{\infty} e^{-st} f(t)dt \tag{C.10.5}$$

We will also need some transformation rules and the following transformation pair to solve the problem where $*$ denotes the convolution between two functions. (University, u.d.)

$$\mathcal{L}_t{}^{-1}\left(e^{-\sqrt{s}a}\right) = \frac{x}{\sqrt{4t^3\pi}} e^{-\frac{x^2}{4t}}\theta(t), x > 0 \tag{C.10.6}$$

$$\mathcal{L}_t{}^{-1}\left(F(s)G(s)\right) = f(t) * g(t) \tag{C.10.7}$$

$$\mathcal{L}_t f(at) = \frac{1}{a}F(\frac{s}{a}) \tag{C.10.8}$$

$$\mathcal{L}_t(f(t)e^{bt}) = F(s-b) \tag{C.10.9}$$

$$\mathcal{L}_t(\partial_t u)(x,s) = sU(x,s) \tag{C.10.10}$$

$$\mathcal{L}_t(\partial_x^2 u)(x,s) = \partial_x^2 U(x,s) \tag{C.10.11}$$

$$\mathcal{L}_t \partial_x u(x,s) = \partial_x U(x,s) \tag{C.10.12}$$

The PDE becomes transformed to the following homogenous, second- order ODE which is solved using the characteristic polynomial of the equation.

$$sU(x,s) - D_{ax}\partial_x^2 U(x,s) + \bar{v}\partial_x U(x,s) = 0 \tag{C.10.13}$$

$$\Rightarrow r^2 - r\frac{\bar{v}}{D_{ax}} - \frac{s}{D_{ax}} = 0 \tag{C.10.14}$$

$$r = \frac{\bar{v}}{2D_{ax}} \pm \sqrt{(\frac{\bar{v}}{2D_{ax}})^2 + \frac{s}{D_{ax}}} \tag{C.10.15}$$

$$\Rightarrow U(x,s) = e^{\frac{\bar{v}}{2D_{ax}}x} * \left(A(s)e^{\sqrt{(\frac{\bar{v}}{2D_{ax}})^2 + \frac{s}{D_{ax}}}x} + B(s)e^{-\sqrt{(\frac{\bar{v}}{2D_{ax}})^2 + \frac{s}{D_{ax}}}x} \right) \tag{C.10.15}$$

We are only interested in bounded solutions for $x > 0$. For $Re\ s > 0$, we require that $A(s) = 0$. Applying the boundary condition, we get that $U(0,s) = F(s) = B(s)$ which gives

$$U(x,s) = e^{\frac{\bar{v}}{2D_{ax}}x}F(s)e^{-\sqrt{(\frac{\bar{v}}{2D_{ax}})^2 + \frac{s}{D_{ax}}}x} = F(s)e^{\frac{\bar{v}}{2D_{ax}}x} * e^{-\sqrt{\frac{\frac{\bar{v}^2}{4D_{ax}}+s}{D_{ax}}}x} \tag{C.10.16}$$

The solution to the initial problem follows by taking the inverse Laplace transform of $U(x,s)$ which by (7) gives the solution

$$u(x,t) = \mathcal{L}_t^{-1}(U(x,s)) = \mathcal{L}_t^{-1}\left(F(s)e^{\frac{\bar{v}}{2D_{ax}}x}e^{-\sqrt{\frac{\frac{\bar{v}^2}{4D_{ax}}+s}{D_{ax}}}x} \right) =$$

$$e^{\frac{\bar{v}}{2D_{ax}}x}\mathcal{L}_t^{-1}\left(F(s)e^{-\sqrt{\frac{\frac{\bar{v}^2}{4D_{ax}}+s}{D_{ax}}}x} \right) = f(t) * \mathcal{L}_t^{-1}\left(e^{-\sqrt{\frac{\frac{\bar{v}^2}{4D_{ax}}+s}{D_{ax}}}x} \right) \tag{C.10.17}$$

Applying transformation pair (6) together with transformation rules (8) and (9) gives

$$\mathcal{L}_t^{-1}\left(e^{-\sqrt{\frac{\frac{\bar{v}^2}{4D_{ax}}+s}{D_{ax}}}x} \right) = e^{-\frac{\bar{v}^2}{4D_{ax}}t}\frac{x}{\sqrt{4D_{ax}t^3\pi}}e^{-\frac{x^2}{4D_{ax}t}}\theta(t) \tag{C.10.18}$$

We now acquire the solution by computing the convolution given by

$$u(x,t) = e^{\frac{\bar{v}}{2D_{ax}}x}\left(f(t) * e^{-\frac{\bar{v}^2}{4D_{ax}}t}\frac{x}{\sqrt{4D_{ax}t^3\pi}}e^{-\frac{x^2}{4D_{ax}t}}\theta(t) \right)$$

$$= e^{\frac{\bar{v}}{2D_{ax}}x}\int_{-\infty}^{t} f(\tau)e^{-\frac{\bar{v}^2}{4D_{ax}}(t-\tau)}\frac{x}{\sqrt{4D_{ax}(t-\tau)^3\pi}}e^{-\frac{x^2}{4D_{ax}(t-\tau)}}\,d\tau$$

Inserting $f(t) = \theta(t-\beta)$ we get after some rearranging and using the quadration rule

$$u(x,t) = e^{\frac{\bar{v}}{2D_{ax}}x} \int_{\beta}^{t} \frac{x}{\sqrt{4D_{ax}(t-\tau)^3\pi}} e^{-\frac{\bar{v}^2}{4D_{ax}}(t-\tau)} e^{-\frac{x^2}{4D_{ax}(t-\tau)}} d\tau =$$

$$\int_{\beta}^{t} \frac{x}{\sqrt{4D_{ax}(t-\tau)^3\pi}} e^{\frac{\bar{v}}{2D_{ax}}x} e^{-\frac{\bar{v}^2}{4D_{ax}}(t-\tau)} e^{-\frac{x^2}{4D_{ax}(t-\tau)}} d\tau = \int_{\beta}^{t} \frac{x}{\sqrt{4D_{ax}(t-\tau)^3\pi}} e^{\frac{-x^2+2\bar{v}(t-\tau)-\bar{v}^2(t-\tau)^2}{4D_{ax}(t-\tau)}} d\tau =$$

$$\int_{\beta}^{t} \frac{x}{\sqrt{4D_{ax}(t-\tau)^3\pi}} e^{-\frac{(x-\bar{v}(t-\tau))^2}{4D_{ax}(t-\tau)}} d\tau \qquad \text{(C.10.19)}$$

We now use a trick and write

$$u(x,t) = \int_{\beta}^{t} \frac{x}{\sqrt{4D_{ax}(t-\tau)^3\pi}} e^{-\frac{(x-\bar{v}(t-\tau))^2}{4D_{ax}(t-\tau)}} d\tau = \int_{\beta}^{t} \frac{1}{2} \frac{x+\bar{v}(t-\tau)}{\sqrt{4D_{ax}(t-\tau)^3\pi}} e^{-\frac{(x-\bar{v}(t-\tau))^2}{4D_{ax}(t-\tau)}} +$$

$$\frac{1}{2} \frac{x-\bar{v}(t-\tau)}{\sqrt{4D_{ax}(t-\tau)^3\pi}} e^{-\frac{(x-\bar{v}(t-\tau))^2}{4D_{ax}(t-\tau)}} d\tau = \int_{\beta}^{t} \frac{1}{2} \frac{x+\bar{v}(t-\tau)}{\sqrt{4D_{ax}(t-\tau)^3\pi}} e^{-\frac{(x-\bar{v}(t-\tau))^2}{4D_{ax}(t-\tau)}} d\tau +$$

$$\int_{\beta}^{t} \frac{1}{2} \frac{x-\bar{v}(t-\tau)}{\sqrt{4D_{ax}(t-\tau)^3\pi}} e^{-\frac{(x-\bar{v}(t-\tau))^2}{4D_{ax}(t-\tau)}} d\tau = \int_{\beta}^{t} \frac{1}{2} \frac{x+\bar{v}(t-\tau)}{\sqrt{4D_{ax}(t-\tau)^3\pi}} e^{-\frac{(x-\bar{v}(t-\tau))^2}{4D_{ax}(t-\tau)}} d\tau +$$

$$\int_{\beta}^{t} \frac{1}{2} \frac{x-\bar{v}(t-\tau)}{\sqrt{4D_{ax}(t-\tau)^3\pi}} e^{\frac{\bar{v}}{D_{ax}}x} e^{-\frac{(x+\bar{v}(t-\tau))^2}{4D_{ax}(t-\tau)}} d\tau$$

Now putting $\eta_1 = \frac{x-\bar{v}(t-\tau)}{\sqrt{4D_{ax}(t-\tau)}}$ and $\eta_2 = \frac{x+\bar{v}(t-\tau)}{\sqrt{4D_{ax}(t-\tau)}}$

Gives $\frac{d\eta_1}{d\tau} = \frac{1}{2} \frac{x+\bar{v}(t-\tau)}{\sqrt{4D_{ax}(t-\tau)^3}}$ and $\frac{d\eta_2}{d\tau} = \frac{1}{2} \frac{x-\bar{v}(t-\tau)}{\sqrt{*D_{ax}(t-\tau)^3}}$ and we now get

$u(x,t) = \frac{1}{\sqrt{\pi}} \int_{\frac{x-\bar{v}(t-\beta)}{\sqrt{4D_{ax}(t-\beta)}}}^{\infty} e^{-{\eta_1}^2} d\eta_1 + \frac{1}{\sqrt{\pi}} e^{\frac{\bar{v}}{D_{ax}}x} \int_{\frac{x+\bar{v}(t-\beta)}{\sqrt{4D_{ax}(t-\beta)}}}^{\infty} e^{-{\eta_2}^2} d\eta_2$ which we identify as the complementary error function. This gives the final solution.

$$u(x,t) = \begin{cases} 0, t < \beta \\ \frac{1}{2}\alpha\left(\left(erfc\left(\frac{x-\bar{v}(t-\beta)}{\sqrt{4D_{ax}(t-\beta)}}\right)\right) + e^{\frac{\bar{v}}{D_{ax}}x}\left(erfc\left(\frac{x+\bar{v}(t-\beta)}{\sqrt{4D_{ax}(t-\beta)}}\right)\right)\right), t > \beta \end{cases} \qquad \text{(C.10.20)}$$

We should check with boundary conditions and initial value conditions that the solution is correct. It is directly apparent that the solution satisfies $u(x,0) = 0$. It also becomes apparent when taking limits that $u(0,t) \to \theta(t-\beta)$ when $t \longrightarrow \beta$.

The full solution to the original problem follows by solving A.8.3 by a similar procedure and adding the two solutions together. This concludes the proof of solving problem A.8.1.

11 Appendix D-Experiments-ÄKTA Explorer 100 system

11.1 Conductivity experiments

In the following section a compilation of the conductivity experiments run and the parameter estimation using ÄKTA Explorer 100 is summarized.

11.1.1 Parameter estimation

The discrete and analytic model (eqn. (27)) showed similar results when compared with experiments, seen in figure (40) below, with a slight increase in deviation at lower flowrates. This was assumed to be due to differences in sensitivity of the dispersion Pe- parameter. The analytic model appeared more dispersion sensitive and more accurate compared with experimental data over a wider range of different flowrates, affecting the dispersion coefficient, $D_{Ax} = f(\bar{v})$, which can be seen in figure 1 below.

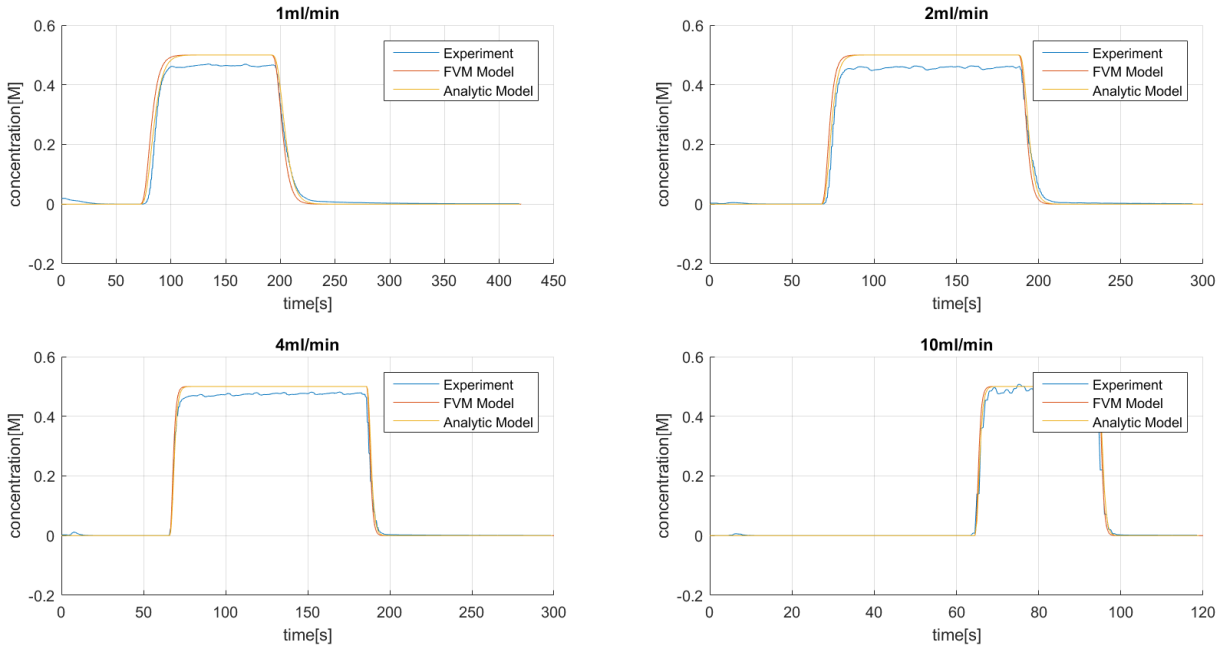

Figure 1: Comparison between analytic model, discrete model(FVM) and experiment. Pe= 0.017.

The simulations in the experimental study were conducted with a dispersion Peclét value of 0.017, calibrated by a parametric sweep for eqn. (27) for a volumetric flow rate of 2 ml/min, which can be seen in figure 2. The standard error for the estimated parameter was estimated to approximately 2.43%, based on a co-variance value of $3.79 * 10^{-4}$. All the data that were sampled were time dependent, where every data point is dependent of the data point before it. This makes statistical analysis less reliable for this type of experiments. For the validation procedure, it was most interesting to capture the transient mixing of the two inlet streams in the conductivity curve and deviation from mean average residence time, when running the experiments and thus no weighting factor or attempt to adjust measured data by erasing outliers were made, to decrease the standard error and ensure a better fit for the mathematical model.

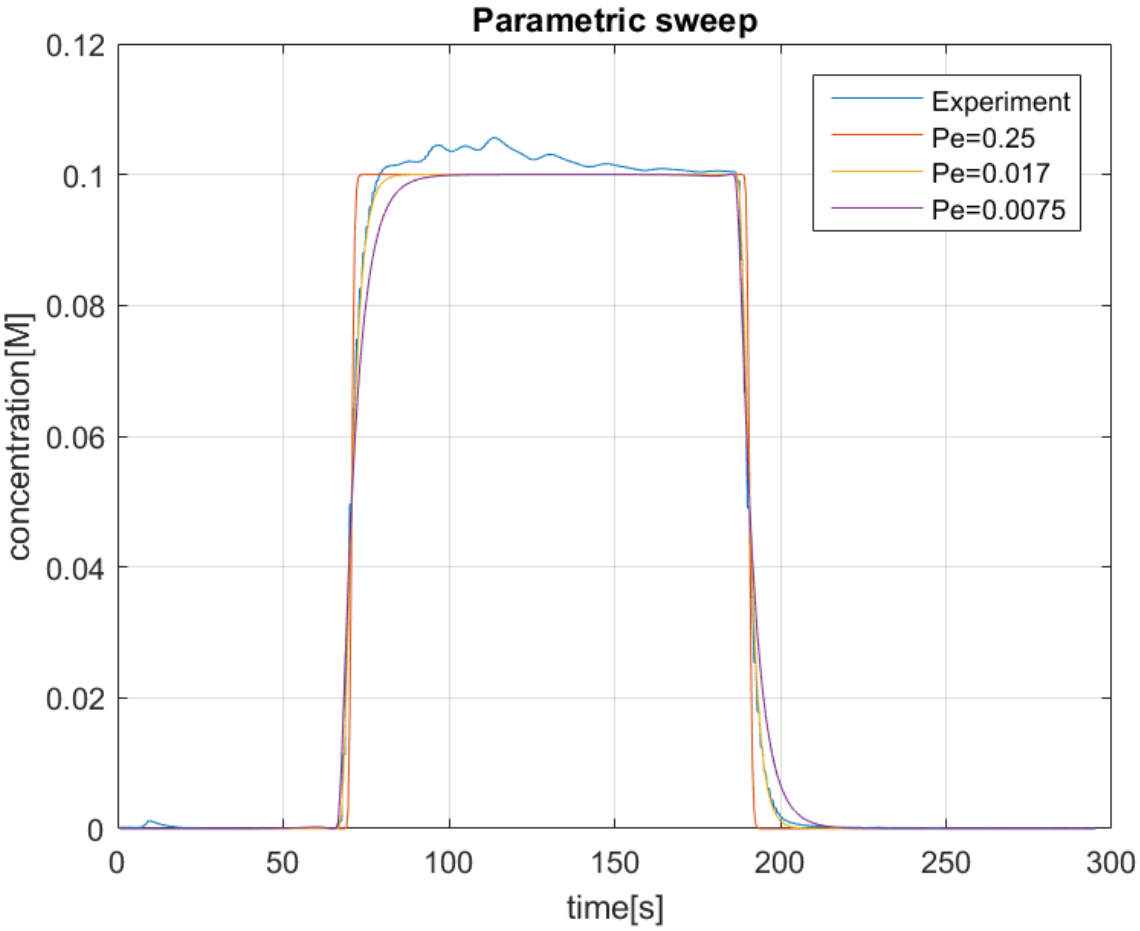

Figure 2: Parametric sweep for Pe =0.25; 0,017; 0.0075

11.1.2 Estimation of time lag

Measurements for estimation of time-lag between signal execution by Orbit to measured response signal in Unicorn.

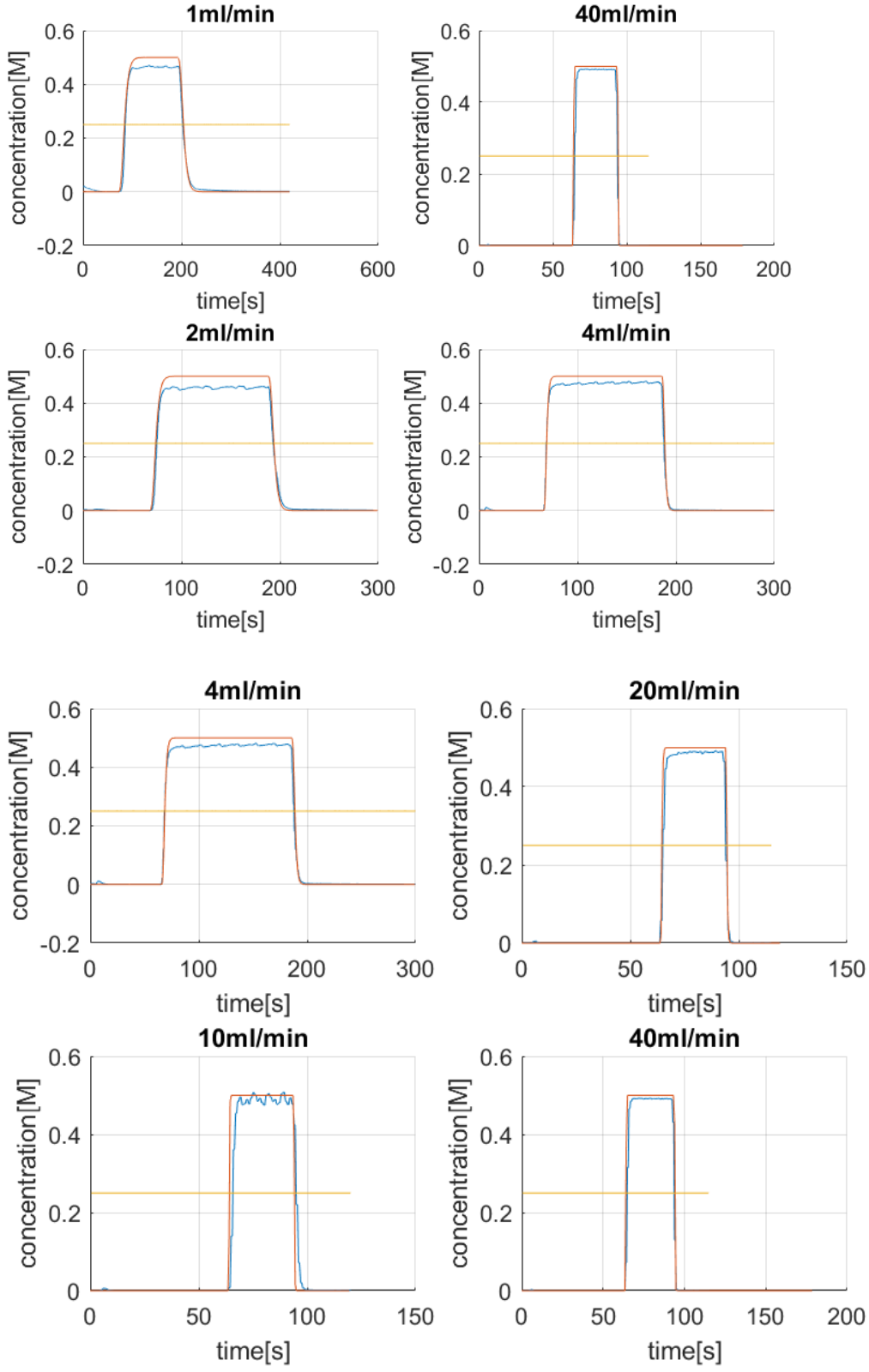

11.1.3 Ratio experiments

Experiments for different ratios 20,40 and 64.2 cm conducted for ratios 100,50,20 and 10% for 1M Na Cl at a flowrate of 1ml/min. TDS factor was 0.65.

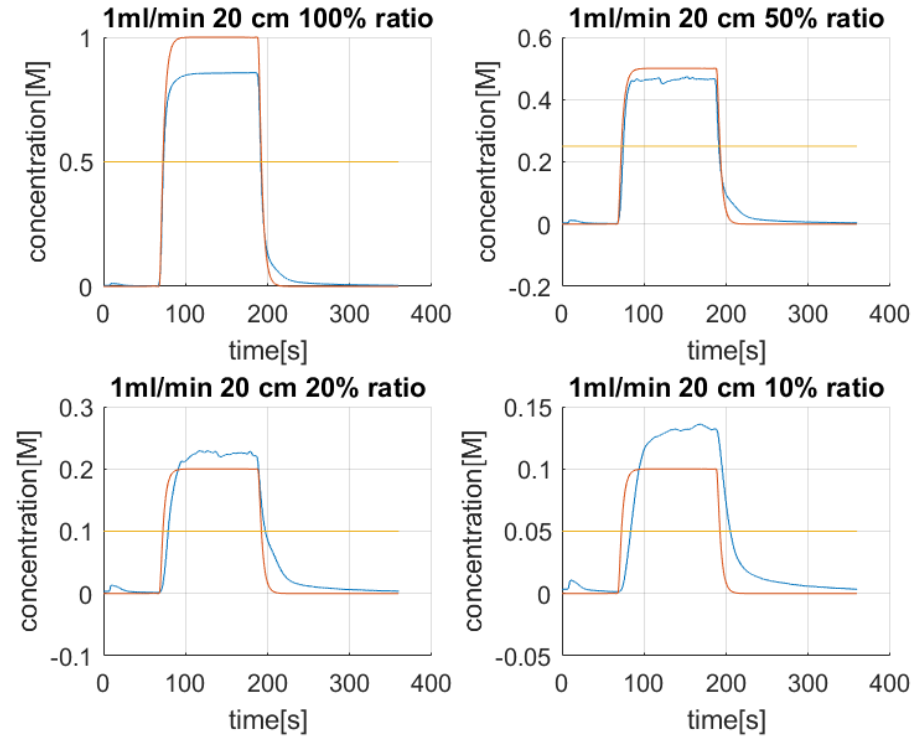

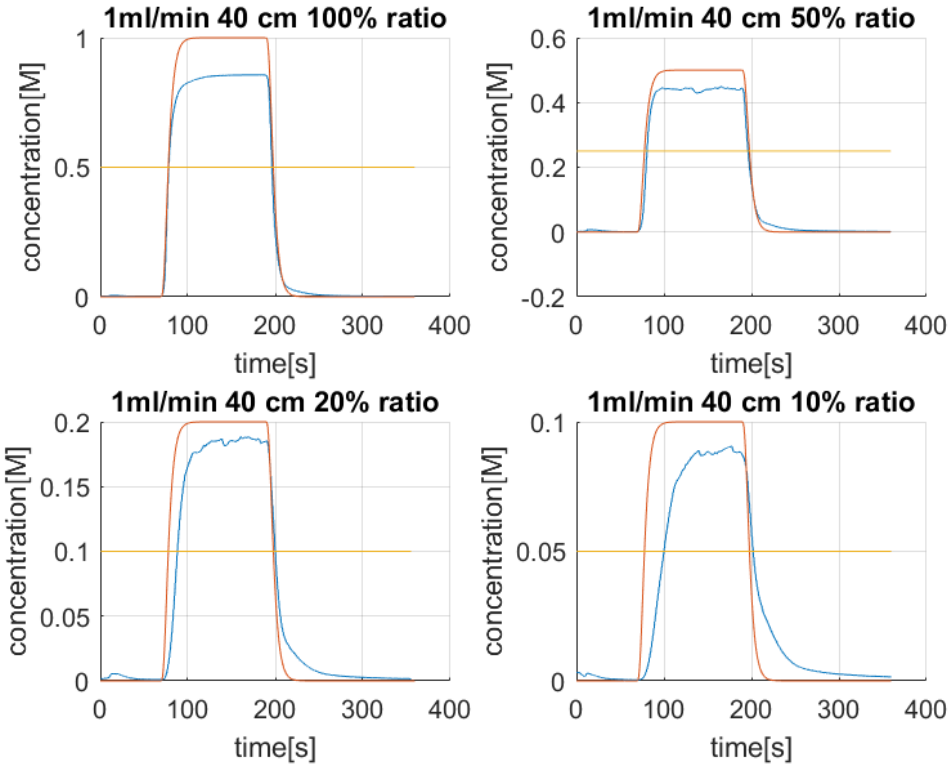

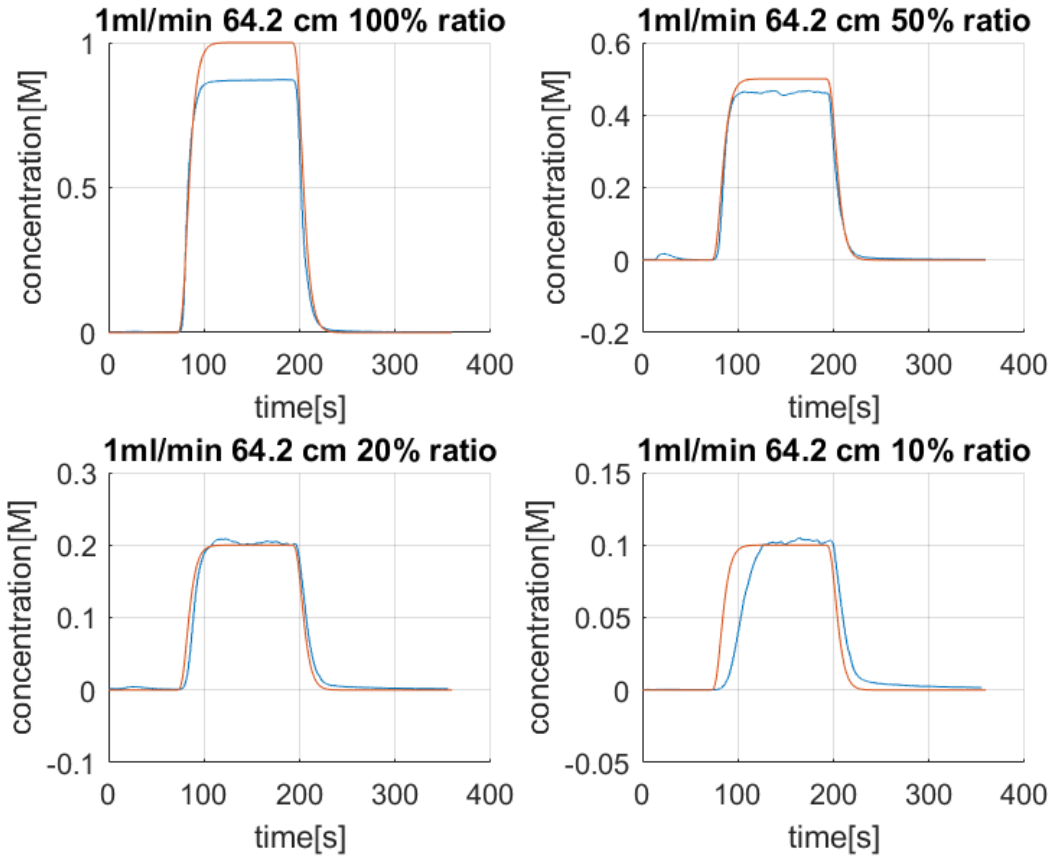

11.1.4 Asymmetric and Symmetric configuration

Comparison between asymmetric and symmetric flow configuration for T-mixer.